UNIVERSITÀ DEGLI STUDI DI CATANIA

DIPARTIMENTO DI FISICA E ASTRONOMIA
DOTTORATO DI RICERCA IN FISICA
XXX CICLO

ALESSIO COMPAGNINO

PROPERTIES AND CORRELATION OF FLARES AND CORONAL MASS EJECTIONS AND THEIR POSSIBLE RELEVANCE ON THE SOUTHERN NIGHT SKY BACKGROUND : A STATISTICAL STUDY

—-
TESI DI DOTTORATO
—-

Coordinator: Prof. V. Bellini
Tutor: Chiar.ma Prof.ssa F. Zuccarello
Cotutors: Dott. P. Romano
Prof.ssa R. Caruso

ANNO ACCADEMICO 2016-2017

Contents

1 Introduction **1**

1.1 Eruptive phenomena on the Sun 1

1.2 Effects of solar phenomena on the Earth environment 6

2 Solar flares: observational characteristics and standard model **13**

2.1 Flare emission, morphology, physical parameters 13

2.2 Flare classifications 15

2.3 Standard model 16

3 Flare occurrence in Active Longitudes **20**

3.1 Data sample 21

3.2 Flare Distribution Over the Solar Cycles 21

3.3 Results of the analysis on flare occurrence in Active Longitudes 21

3.4 Summary 29

4 Coronal Mass Ejection: observations and models **30**

4.1 CME morphology and physical parameters 30

4.2 Models for CMEs initiation 31

4.3 The state-of-the-art on statistical studies of CMEs parameters 35

5 Statistical analysis on selected CME's parameters **37**

5.1 LASCO and CACTus datasets 37

5.2 CME Parameters Over the Solar Cycles 23 and 24 37

6 Correlation between flares and CMEs: a statistical approach **45**

6.1 Previous results reported in literature 45

6.2 GOES dataset 46

6.3 Correlation between flares and CMEs 47

6.4 CME Parameters and Flare Energy 53

7 **Possible correlation between CME occurrence and variations of the night-sky brightness** **57**

7.1 The Fluorescence Detector 58

7.2 The Night Sky Brightness 60

7.2.1 Dependence of NSB on the solar cycle 61

7.2.2 The results of ground-based NSB measurements 63

7.3 The measurement of the night sky background in the Pierre Auger Observatory 63

7.3.1 Result on the night sky photon flux from the Pierre Auger Observatory 64

7.4 Most recent results on the Night Sky Background 66

7.4.1 Results 68

7.5 Correlation between CMEs and Night Sky Background 71

8 **Discussion and Conclusions** **77**

Acknowledgements **84**

Bibliography **84**

Abstract

This Thesis is devoted to a statistical study of solar phenomena (flares and coronal mass ejections) and their possible effects on the Earth.

The Sun, our star, can be considered a huge laboratory where we can study the interaction of a ionized gas with magnetic fields. In particular, the solar atmosphere (the outer layers of the Sun, those which are accessible to observations) is characterized by phenomena that due their existence to localized magnetic fields: sunspots, faculae, filaments, active regions, bright points, coronal holes, etc. The occurrence of these phenomena is variable, depending on the so-called activity cycle, characterized by a period of 11 years.

Moreover, in some situations, the magnetic field that permeates the active regions, from an initial potential field configuration (characterized by the minimum energy content), can slowly store energy, changing its configuration to more complex and more energetic ones. When the magnetic field configuration is not able to maintain its equilibrium, the stored magnetic energy is abruptly released, giving rise to phenomena that are generally termed as solar eruptions but that, depending on their characteristics, are distinguished between flares, filament eruptions and coronal mass ejections.

In the last decades, the possibilities offered by new computer capabilities, new instruments and by satellite observations, have allowed us to understand many of the characteristics of these eruptions, as well as their effects on the Earth magnetosphere and ionosphere.

However, despite the progress in our comprehension of these phenomena, there are still many aspects that need to be clarified: how and where is the energy stored, what causes the trigger of the eruption, how the different phenomena are related to each other and how they can affect our environment, to cite only a few.

In this scenario, the work carried out in this Thesis has been motivated by three main questions:

- Are there preferential locations on the Sun where the magnetic field is prone to produce eruptive events ?
- What kind of correlation exists between flares (mainly confined to the solar atmosphere) and coronal mass ejections that, by definition, expel magnetized clouds into the interplanetary space ?
- Can the charged particles emitted during these events and arriving to the Earth ionosphere have a role in the observed variations of the night-sky background ?

The attempt to provide answers to the previous questions has been faced in this Thesis from an observational / statistical point of view.

More precisely, the dataset that have been used in order to answer the first two questions have been retrieved from public archives of flares and coronal mass ejections relevant to the last two solar cycles (23 and 24), while in order to provide an answer to the third question, also data acquired by the Pierre Auger Observatory have been used.

The main results obtained in this Thesis can be summarized as follows:

- The spatial and temporal distribution of the flares analyzed show persistent domains of occurrence within well defined belts of longitude, with a behavior similar to the one observed for other activity phenomena, like the sunspots.
- There is a temporal correlation between flares and CMEs for the 60 % of the events analyzed; the time interval (between 10-130 minutes) however depends on the dataset used. Moreover, the majority of CMEs with highest velocities show a clear temporal correlation with flares.
- The variations in the night-sky background analyzed for the nights when a major impact of charged particles associated to CMEs was expected, could not be clearly correlated to these events.

The Thesis is organized as follows: in Chapter 1 we provide a brief introduction on the characteristics of the solar atmosphere and on the main eruptive phenomena occurring in the Sun. Chapters 2 reports the main observational characteristics of flares and a description of the flare standard model, while Chapter 3 describes the work carried out in order to study the occurrence of flares in preferential regions called Active Longitudes. The main observational characteristics of CMEs are reported in Chapter 4. Chapters 5 and 6 report respectively on the statistical study of CMEs, on properties and correlation with flares. The study carried out using the data provided by the Pierre Auger Observatory in order to investigate the possible correlation between flares, coronal mass ejections and the variations in the night-sky background is reported in Chapter 7. The discussion of the results obtained in this Thesis and the conclusions are reported in Chapter 8.

A mamma e papà

Chapter 1

Introduction

1.1 Eruptive phenomena on the Sun

This chapter introduces the main characteristics of solar eruptive phenomena occurring in the solar atmosphere: filament eruptions, flares and coronal mass ejections (CMEs). These phenomena involve the interaction between localized magnetic fields and the hot ionized gas of the solar atmosphere (known as *plasma* i.e., a fluid that can be locally charged but globally electrically neutral, formed by both neutral and charged particles, such as electrons, protons and ions).

The Sun's atmosphere is composed by three main regions which present different temperature and density distributions (Figure 1.1). The innermost layer, the *photosphere*, extends for about 500 km and is characterized by a temperature ranging between 5780 and 4300 K and a density of 2×10^{-4} kg m^{-3}. Most of the sunlight we observe is emitted from this layer. Above the photosphere there is the *chromosphere*, extending for $\sim$ 2500 km, with a temperature ranging from 4300 to $\sim$ 25000 K. A thin layer, called *transition region*, is located above the chromosphere: here the temperature suddenly increases from 10^4 to 10^5K. The outermost and hottest layer of the Sun is the *corona*, characterized by a temperature of about $2{\times}10^6$ K, and a density of $\sim 10^{-12} - 10^{-14}$ kg m^{-3}. A flow of plasma, such as electrons, ions, and α particles, extending from the corona and propagating toward the interplanetary medium, is known as *solar wind* (Golub *et al.*, 2009). Depending on the velocity, density and source of origin of the solar wind, we can distinguish between two different regimes: the fast solar wind, with velocities of $\sim$ 500 - 800 km s^{-1} at 1 AU and originating mainly in the polar regions (where dark features, with low emission in the Extreme Ultra Violet (EUV) and X-ray range, known as *coronal holes*, are located), and the slow solar wind, characterized by velocities of $\sim$ 300 - 400 km s^{-1} at 1 AU, originating mainly from equatorial regions.

In the solar atmosphere several features can be observed: sunspots, faculae, filaments, bright points, coronal loops, active regions. Their appearance and evolution is related to localized magnetic fields that emerge from the subphotospheric layers and later diffuse in the solar atmosphere. The number of sunspots present on the solar disc is quantified through the *Wolf Number* W = k(f+10g), where k is a parameter that depends on the observational conditions (i.e., site, telescope, observer), while f and g indicate the total number of sunspots and sunspot groups, respectively, present on a certain day on the solar disk. The Wolf Number is not constant in time, but follows a well defined periodicity (11-year), such that phases of maximum activity are followed by phases of low activity. Each 11-year period is called *solar cycle*.

At the beginning of each solar cycle the sunspots appear at latitudes of $\sim$ 40 degrees, while in the following years the latitudes of appearance of sunspots slowly decrease and at the end of the cycle these features are observed close to the solar equator, following a pattern that is generally recognized by means of the Butterfly diagram. Moreover, within each solar cycle, the polarity of the sunspots is governed by the Hale's Law, according to which in each solar hemisphere the preceding (i.e., the western) sunspot in each group has always the same polarity and in the other hemisphere the preceding sunspot has the opposite polarity. In the following cycle the situation is reversed (Zirin, 1988).

Another characteristic of the solar magnetic activity is related to the presence of the so-called *active longitudes*, that are belts of longitude of about 15 degrees, characterized by the continuous emergence of magnetic flux and that therefore show a higher level of activity than the surrounding longitudes.

As we are mainly interested in solar phenomena that can give rise to eruptive events, we will describe in the following the main characteristic of these features / events, while we defer the reader to Zirin (1988) for a complete description of other solar activity phenomena.

In the chromosphere and corona, in the $H\alpha$ (6563 Å) and $He\ II$ (304Å) lines respectively, we often observe dark elongated features, called *filaments*, which are characterized by a main axis, called *spine* (Figure 1.2), that presents features protruding laterally named *barbs* (indicated by white arrows in Figure 1.2). Solar filaments appear dark due to the absorption that causes a lower emission with respect to the background atmosphere. When they are located on the solar limb, they appear bright and are referred to as *prominences*.

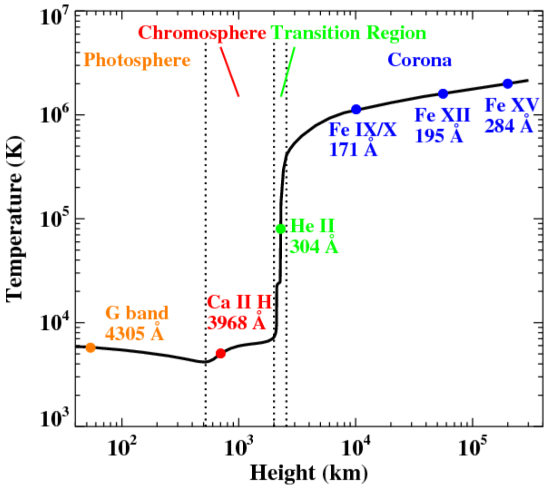

FIGURE 1.1: Temperature distribution vs height in the solar atmosphere (Yang *et al.*, 2009).

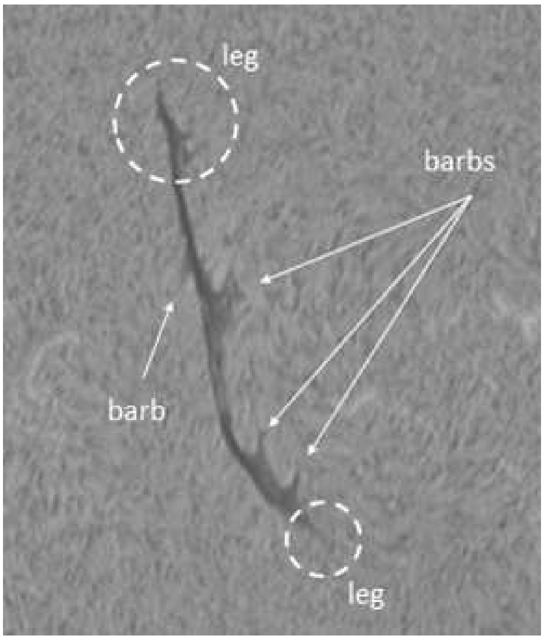

FIGURE 1.2: High resolution image of a filament observed in $H\alpha$ (6563 Å). The barbs are the dark structures, indicated by arrows and departing from the axis of the filament (the spine). White circles indicate the legs or outer ends of the filament.

Filaments are located on the polarity inversion line (PIL), i.e., the line separating the two opposite magnetic field polarities (Martin, 1998) and usually the two outer ends are anchored in one or more regions of opposite magnetic polarity. They form when localized magnetic fields rise from the subphotospheric layers to the solar atmosphere, assuming a configuration which is the result of a competition between two main forces, (magnetic tension and magnetic pressure), that cause the suspension of cold and dense material at heights of about 10 Mm, sometimes for several solar rotations. When the filament dynamical equilibrium is perturbed, the instability can cause the eruption of the plasma in a phenomenon known as *filament eruption*. For a summary of current observations, theories and models of filaments see Labrosse *et al.* (2010), Mackay *et al.* (2010), Parenti (2014).

Solar flares are transient phenomena that cause a violent and sudden release of energy, of about $10^{28} - 10^{32}$ erg, that can last for some tens of minutes or hours and can involve emission in the whole electromagnetic spectrum (Emslie *et al.*, 2012). The emitted radiation can cover in fact many wavelengths, ranging from radio waves (10^{6} cm) to gamma ray (10^{-11} cm). A solar flare was observed for the first time by Carrington (1859) and since then these phenomena have been extensively studied. Figure 1.3 shows a flare observed by the Transition Region and Coronal Explorer (TRACE) in the EUV range. The largest and most energetic events, called *two ribbon flares*, are characterized in chromospheric and UV lines by two narrow and long bright regions located on both sides of the PIL (Figure 1.4). These flares are usually associated with CMEs, that are the most massive and energetic solar eruption of plasma and magnetic field, originating from the solar corona and propagating into interplanetary space (Gopaswamy, 2008).

One aspect concerning the flare occurrence that needs to be further investigated

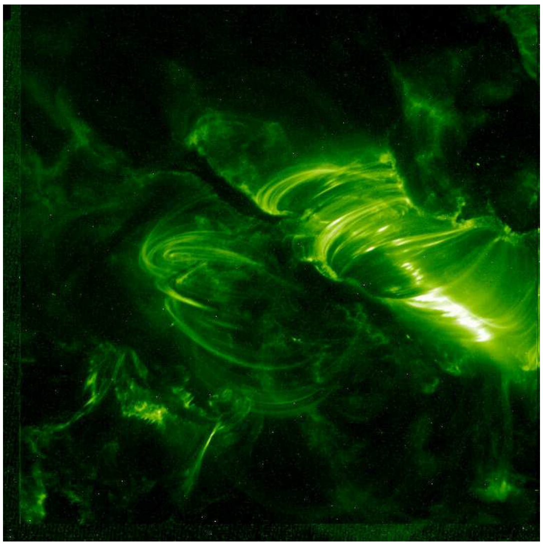

FIGURE 1.3: A two ribbon flare observed by TRACE in the EUV range on 2nd April, 2001 in active region NOAA 9393.

is related to the location of appearance of the active regions hosting the flares: it seems in fact that there are some preferential longitude strips the so-called *active longitudes* (ALs) where these phenomena take place with the highest probability. To this aim, part of this thesis (Sect. 3) is devoted to a statistical analysis on the occurrence of flares in the ALs during the solar activity cycles 23 and 24.

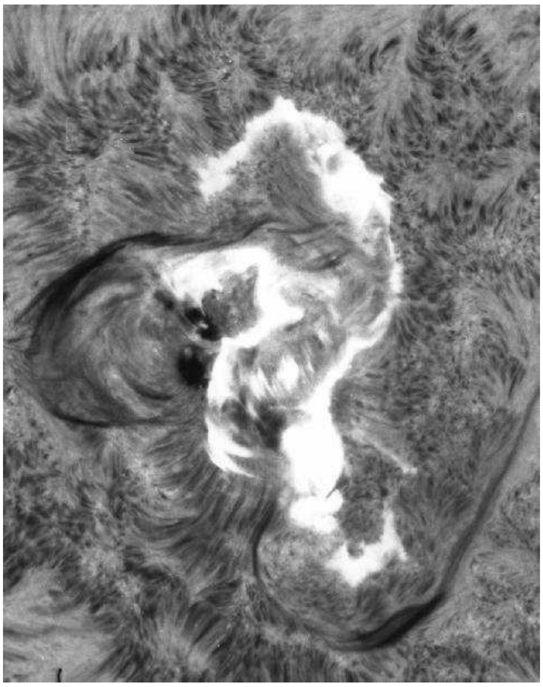

FIGURE 1.4: A two ribbon flare occurred on 7th August 1972, observed by the Big Bear Solar observatory in the Hα line.

CMEs occur with a frequency of few events per day during the solar maximum. They have a speed of about $100 - 1000$ km s^{-1}, sometimes reaching up to 3500 km

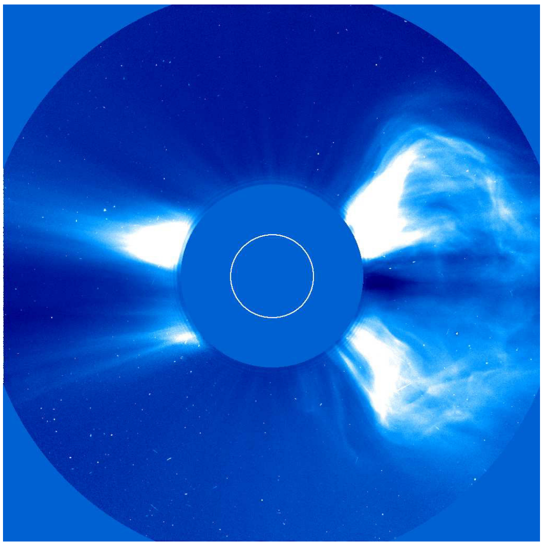

FIGURE 1.5: CME observed by SOHO/LASCO on 7th April 1997.

s^{-1} (Yashiro *et al.*, 2004, Zhao and Dryer, 2014) and kinetic energy up to 10^{32} erg (Compagnino *et al.*, 2017). The mass involved in these phenomena ranges between $10^{14} - 10^{16}$ g. The mass lost by the Sun each year due to the CMEs occurrence depends on both the mass involved in a single event and the number of events occurring during the different phases of the solar activity cycle. An example of a CME observed on 7th April 1997 by the Large Angle Spectrometer Coronagraph (LASCO) onboard of the Solar and Heliospheric Observatory (SOHO) satellite is shown in Figure. 1.5.

As already stated, CMEs are usually associated with other eruptive phenomena on the Sun, like flares and eruptive prominences (Forbes, 2000; Low, 2001). The CMEs properties and a statistical study of the CMEs parameter will be discussed in Sect. 4 of this thesis, while the correlation between flares and CME occurrence will be described in Sect. 5.

1.2 Effects of solar phenomena on the Earth environment

Solar phenomena like the solar wind and the CMEs, during their propagation into the interplanetary space, can cause variations in the heliosphere and in the magnetospheres of planets. In 1930 Sidney Chapman and Vincent Ferraro speculated the existence of energetic particles emitted from the Sun that could produce *geomagnetic storms* when they impacted on the Earth magnetosphere. Since then, many studies have been carried out in order to discover the origin of these phenomena.

A geomagnetic storm is characterized by a brief period (one or few hours) of deep depression in the *horizontal component* of Earth magnetic field at low latitudes (due to the dipolar configuration of the Earth magnetic field, close to the equator the field lines are parallel to Earth's surface, or *horizontal*) and a recovery phase which lasts several days (Rostoker, 1996 ; Lakhina *et al.*, 2005).

In this respect, we recall that the magnetic field anchored to the Sun at one footpoint and distributed in the interplanetary space, is called Interplanetary Magnetic Field (IMF). The IMF has two components (B_x, B_y) parallel to the ecliptic, while the B_z component is perpendicular to the plane of the ecliptic. From the orientation of this magnetic field component it is possible to infer the solar wind or CMEs geoeffectiviness and when interplanetary shocks produced by fast CMEs propagating in the solar wind can generate solar energetic particles (SEP) (Gopalswamy *et al.*, 2003; Cliver and Ling, 2009).

Breaking and merging or reconnection of the CMEs and Earth magnetic field, occurring when they are oriented opposite or antiparallel to each other, produce transfer of energy and mass to the magnetosphere, with dramatic effects observed in the Earth magnetosphere (Figure.1.6).

Another important phenomenon that may be related to and, sometimes, confused with the effects of CMEs is the formation of compression regions behind the slow solar wind. More precisely, when fast solar-wind streams, emanating from coronal holes, interact with slow streams emanating from equatorial regions, they can produce Co-rotating Interaction Regions (CIRs) in the interplanetary space (Figure 1.7). The magnetic field lines of the slow solar wind streams are more curved due to the lower speeds, while the field lines associated with the fast streams are more radial because of their higher speeds (Hundhausen, 1972; Acuña *et al.*, 1995). Intense magnetic fields can be produced at the interface (IF) between the fast and slow streams in the solar wind and the combination of the Earth and solar wind magnetic field conditions can produce strong geomagnetic storms during the minimum of solar activity.

CMEs and CIRs are therefore the two large-scale interplanetary structures that can cause geomagnetic storms under certain conditions: a high plasma speed and a more southward direction of their associated magnetic field, which is opposite to the direction of the Earth magnetic field. These conditions must be maintained for a long period to allow an efficient exchange of energy (Srivastava and Venkatkrishnan, 2004; Naitamor, 2005; Zhukov, 2005 and references therein; Zhang *et al.*, 2007).

When CMEs are ejected from the Sun, they describe a long path in the interplanetary space and reach the Earth in 1 – 4 days, depending on their speed. CMEs that in coronagraphic images are characterized by a projected angular width of 360 degrees are called *halo* CMEs (Howard *et al.*, 1982). Wang *et al.* (2002) found that 81 % of

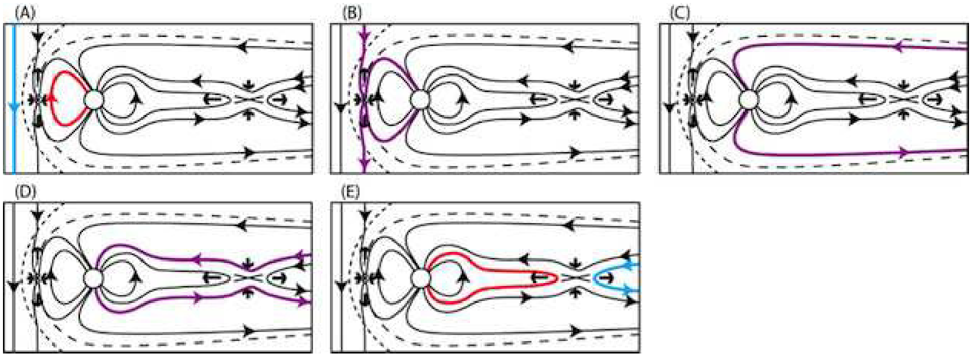

FIGURE 1.6: Schematic drawings of the sequence of phenomena occurring in the Interplanetary Magnetic Field and the Earth's magnetosphere when a geomagnetic storm takes place. Magnetic field reconnection (indicated by arrows) occurs under southward IMF (light blue line in A), adding open flux (purple lines in B) that is convected to the magnetotail (C). Energy is stored in the tail until it is explosively released (D) as the newly closed flux is returned to the dayside (red line in E), giving rise to auroral displays (Eastwood *et al.*, 2012)

.

halo CMEs occur in proximity of the central meridian with a latitude of $(\pm 10 - 30^{\circ})$. Halo CMEs are directed towards the Earth and for this reason are usually source of geomagnetic storms.

Moreover, the Earth-directed CMEs which initiate from the visible solar disk, called *frontside halo*, and the CMEs characterized by a projected angular width greater than 120°, called *partial halo*, can also be geoeffective (Webb, 2002; Gopalswamy Yashiro and Akiyama, 2007). In addition, the frontside halo CMEs that originate on the west side of the Sun show a higher probability to cause geomagnetic storms (Michalek *et al.*, 2006).

Two parameters are important to measure geomagnetic storm intensity and the disturbances that storms cause on the interplanetary environment and on Earth. They are the Planetary-K index (K_p) and the Disturbance Storm Time (DST).

K_p quantifies the variations of the horizontal component of the Earth magnetic field, by a number ranging from 0 to 9, where a value less than or equal to 4 indicates normal condition of the Earth magnetic field and absence of a geomagnetic storm, while those greater than or equal to 5 indicate the presence of a geomagnetic storm and an intense magnetic field activity. This index is computed from the maximum fluctuations of the Earth magnetic field with a 3 hours time cadence. More specifically, the K_p index is the sum between the maximum and minimum absolute value (nT) of the horizontal component of the Earth magnetic field and is computed as the mean weight of the index measured from 13 observatories around the world.

The DST index is a measure of the variation of the horizontal component of the Earth's magnetic field related to the equatorial ring current. This index, calculated on a hourly basis, is determined by using data acquired by four geomagnetic observatories. Although the DST index is considered an indicator of the ring current, there are other currents, such as the current of the magnetopause, the partial ring current etc, that can contribute to determine its value. Due to this reason, currently, the DST index is considered as a measure of the effects produced by indiscriminate over-current systems which flow along the equatorial plane.

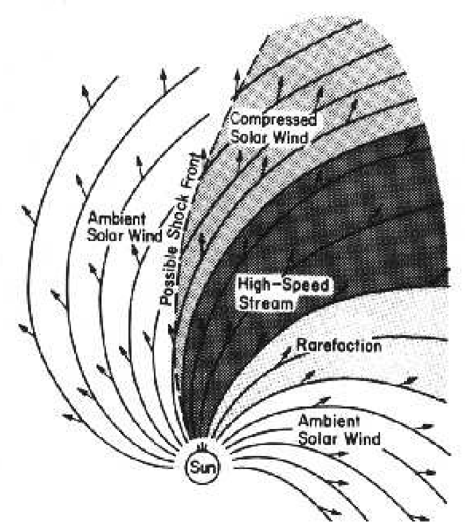

FIGURE 1.7: CIR formation

.

The geomagnetic storm classification based on the DST index is reported in Table 1.1 and the maps of the observatories that measure the k_p and DST indexes are shown in Figures 1.8 and 1.9.

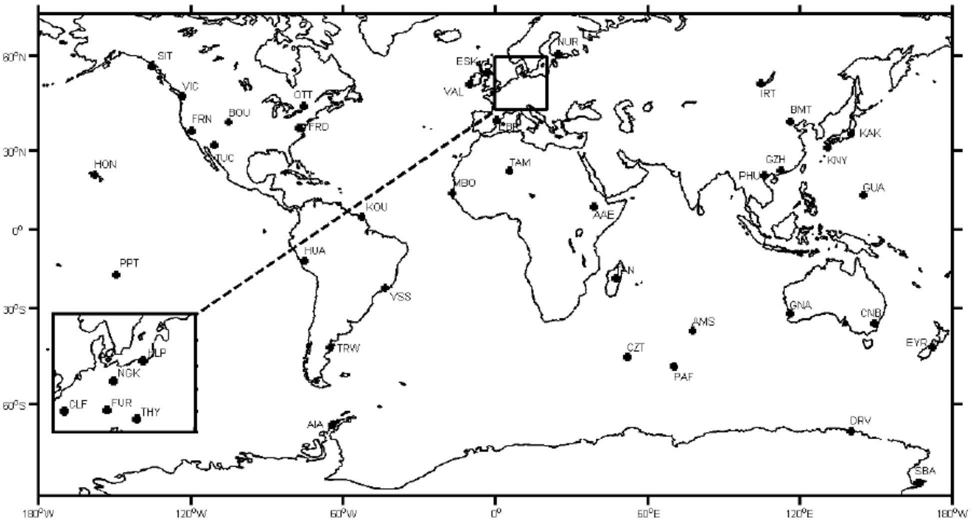

FIGURE 1.8: Global Map of magnetic observatories around the world that measure the k_p index (Segarra and Curto, 2015).

The variation of four parameters mentioned above (k_p, DST, IMF, and B_z) during a geomagnetic storm are shown in Figure 1.10. In this figure the horizontal component of the Earth magnetic field is measured in the Geocentric solar magnetospheric (GSM) system, i.e. the X axis is directed towards the Sun and the Z axis is the projection of the Earth's magnetic dipole axis (positive North) on the plane perpendicular to the X axis.

When charged particles enter the Earth magnetosphere, many disruptive effects can occur because of the enhanced ionospheric current system that can produce induced currents in the power grids and black-out in telecommunication. Orbiting satellites, spacecraft surfaces sensors, solar panels and humans in space can also be damaged by these particles. Moreover, radio and X-ray burst produced by flares can

FIGURE 1.9: Global Map of magnetic observatories around the world that measure the DST index

.

TABLE 1.1: Geomagnetic storm classification (Loewe and Prölss, 1997)

Type	
Weak	-50 < Dst < -30 nT
Moderate	-100 < Dst < -50 nT
Intense	-200 < Dst < -100 nT
Super	Dst < -200 nT

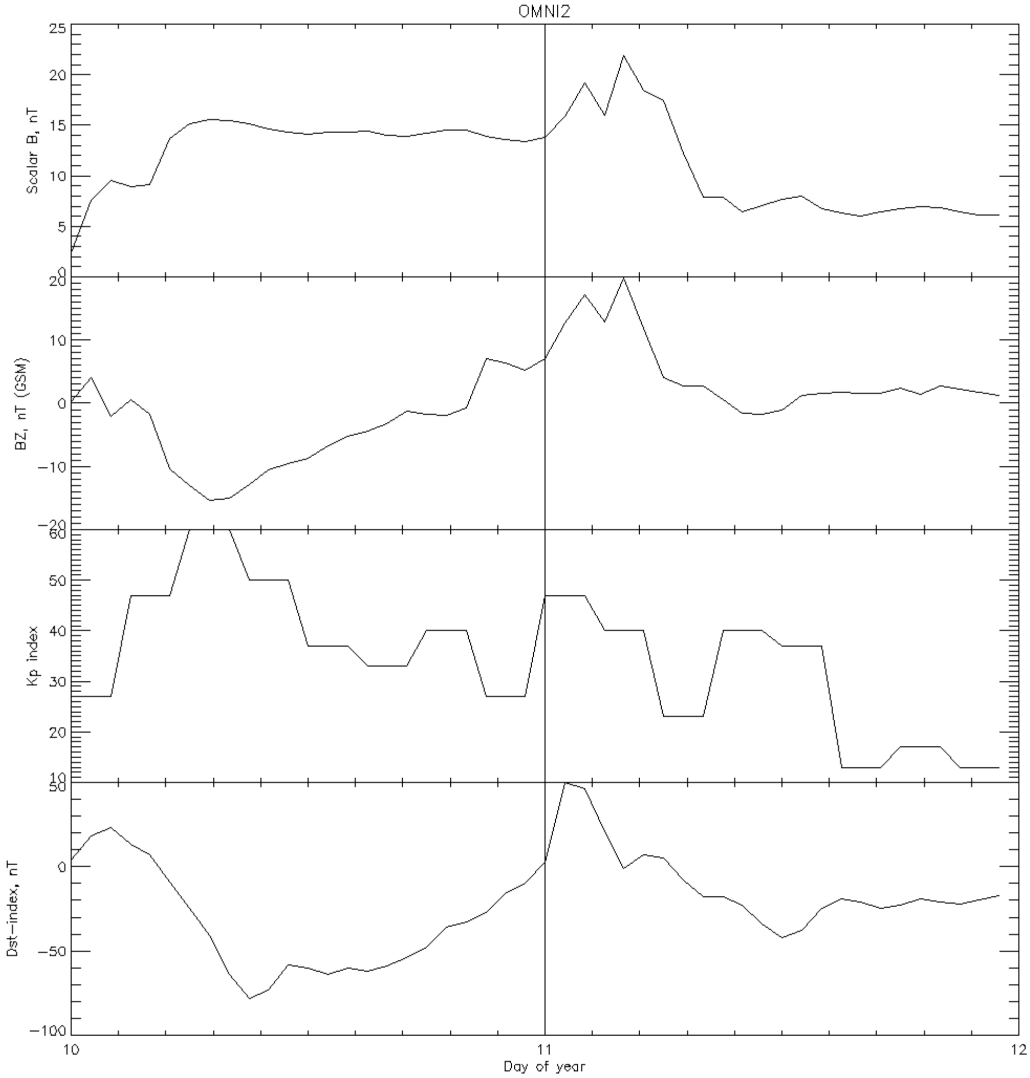

FIGURE 1.10: Effect on the horizontal component of Earth's magnetic field of a geomagnetic storm occurred on 14th July 2000 due to a previous CME observed by LASCO on 11th July 2000. From top to bottom we report the mean value of the scalar IMF (nT), the horizontal component of the Earth magnetic field in the Geocentric solar magnetospheric (GSM) system, the k_p (multiplied by a factor 10) and the DST index. This figure was obtained using the data provided by the NASA OMNIWeb Goddard Space Flight Center Space Physics Data Facility, at the following link : https://omniweb.gsfc.nasa.gov/form/dx1.html

.

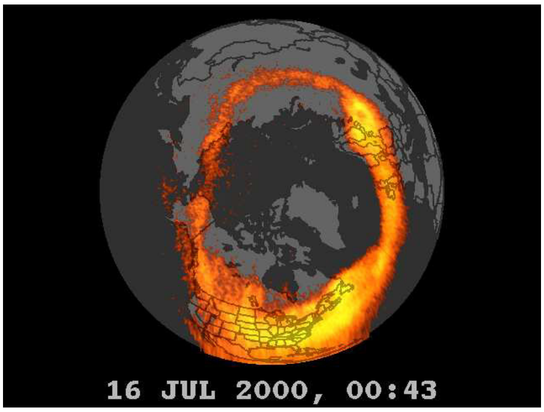

FIGURE 1.11: Auroral oval observed by the NASA Polar Satellite on 16th July 2000

.

cause radio frequency interferences and degradation of high frequencies transmissions at high latitude, together with sudden ionospheric disturbances (SID).

In this context, the term *Space Weather* refers to physical processes that produce changes in the Earth magnetosphere and in the space environment near Earth when any disturbance in the heliospheric plasma impacts on Earth magnetosphere under certain conditions of IMF and terrestrial magnetic field. These changes can affect the space and ground technological systems performance and reliability, as well as the health of humans in space.

Therefore it is important to fully understand and eventually to forecast the occurrence of flares and CMEs in order to avoid or mitigate effects related to the following issues: a) radiation and charging that can cause damage or anomalies to spacecraft; b) damages to humans in space subject to radiation and energetic particles; c) geomagnetic field perturbations; d) disruption of the communication and navigation systems; e) blackout of power grids.

Another effect related to the geoeffectiviness of solar phenomena is the beautiful phenomenon named *aurora*. Particles associated with CMEs or with the solar wind that enter the magnetosphere may be trapped in the magnetic field of the Earth, but some of them may escape penetrating into the Earth's ionosphere, generally close to the terrestrial geomagnetic poles, where they interact with and excite the molecules of the Earth atmosphere. When these molecules decay to a lower state, they emit radiation and cause the auroras. The aurora colors depend on the energy owned by the particles that excite the oxygen and nitrogen molecules present in the atmosphere. The aurora phenomenon on average extends from 100 to 250 km in height and has a typical pattern called auroral oval (see Figure. 1.11). Generally the most spectacular effects are observed at visible wavelengths, but the collision between the molecules of the Earth atmosphere and the charged particles can also cause emission of radiation at other wavelengths, such as in the UV and X-ray ranges.

The image in Figure. 1.12 shows an aurora, occurred on 16th July 2000, caused by a geo-effective CME occurred on 14 July 2000 (for this reason called the Bastille Day event) observed by LASCO at 10:54:07 UT and associated with a flare of class X5.7. This event caused a geomagnetic storm that occurred on 15th July 2000 at 14:37 UT.

FIGURE 1.12: Aurora observed on the 16th July 2000

.

The brief description provided above about the aurora phenomenon underneaths the possibility that in those locations of the Earth where the aurora occurs there is a variation of the night-sky brightness and in order to investigate such effects in the southern hemisphere, we report in Sect. 7 a preliminary study on the possible correlation between CMEs occurrence and changes in the night-sky background using the data provided by the Pierre Auger Observatory.

Chapter 2

Solar flares: observational characteristics and standard model

2.1 Flare emission, morphology, physical parameters

Solar flares are sudden, impulsive and localized ($\sim 10^3 - 10^5$ km) releases of energy occurring in the solar atmosphere. The emission of a flare can be observed across the entire electromagnetic spectrum and may be associated with the ejection of high energy particles and blobs of plasma from the solar atmosphere into the interplanetary space. The kind of emission depends on the energy storage process involved in the flare.

Usually flares are characterized by three phases: the pre-flare, the flash and the main phase (Figure 2.1). During the pre-flare phase we can observe the appearance of Hα blue-shifted events. Soft X Ray (SXR) emission (< 10 keV) that gradually increases because of an enhanced thermal emission from the coronal plasma, as well as emission of hard X Ray (HXR) and gamma rays can also be detected. Moreover, before the HXR emission, an increase of the UV intensity and spectral lines broadening in SXR is also observed.

In the second phase, the flash phase, that lasts typically few minutes, the intensity of the HXR and gamma ray emission increases almost impulsively. In this phase we observe microwave and radio burst (100 to 3000 MHz), as well as HXR burst (> 30 keV) emitted by electrons at high energies. These electrons travel down along the two legs of coronal loops into the low corona and chromosphere, where they heat the plasma very rapidly and may give rise to chromospheric evaporation (see below). Moreover, the HXR component is often characterized by many short but intense and complex spikes of emission at smallest time scales, each lasting two seconds for moderate events and until about tens of seconds for the large ones. After the spiky emission, we observe EUV and UV emission, that appears to be highly correlated in time with the SXR emission. After the flash phase some of the largest flares show a distinct second HXR component due to a second phase of particle acceleration (Priest, 1981).

In the latter phase, called main (or gradual) phase, the hard X-ray and gamma-ray fluxes decline more or less exponentially with a time constant ranging from some minutes to a hour and occasionally one day in the largest two ribbon flares (Priest, 1981). The soft X-ray flux continues to rise and then it falls exponentially, sometimes on time scales of several hours. The soft X-rays are due to thermal radiation, or bremsstrahlung, of a gas heated to temperatures of tens of millions of degrees (Janvier *et al.*, 2015). In this phase, we observe the so called *post-flare loops*, that are very hot (T = 10 MK) and are seen to expand above the flaring region. These loops appear first in hot filters and progressively are observed in colder filters (Forbes, and Acton, 1996). Moreover, newly formed loops appear above already existing loops (e.g. Raftery *et al.*, 2009; sun *et al.*, 2013), filled with evaporated dense plasma, through a process called *chromospheric evaporation*.

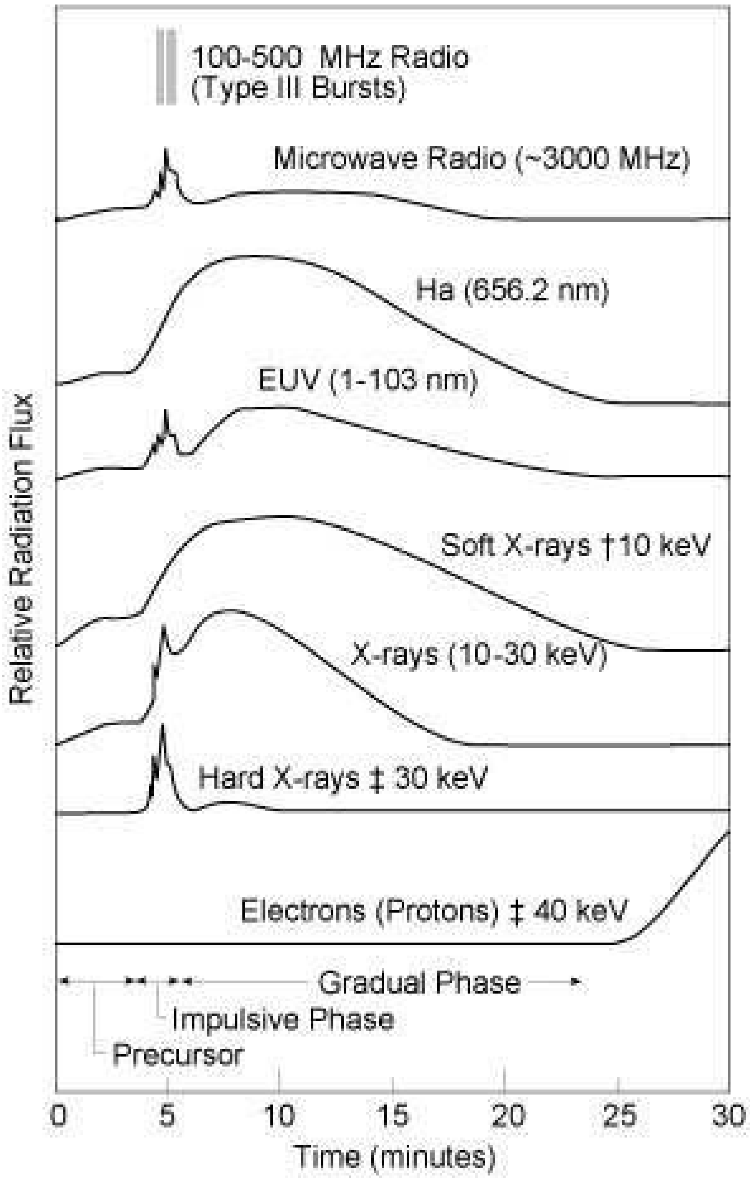

FIGURE 2.1: Time profile of solar flares in different spectral ranges.

The different flare phases described above can be recognized in Figure 2.2, relevant to an event observed on 6th March, 1989. We can see that the preflare phase lasts from about 13:50 to 13:56 UT. This is followed by the flash phase, that ends at about 14:06 UT, when the main phase begins. Note that the soft X-ray flux continues to fall smoothly.

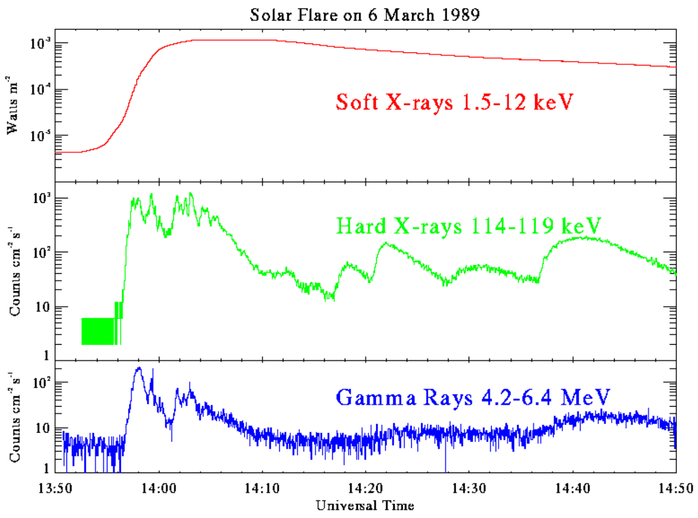

FIGURE 2.2: Different phases of the flare observed on 6 March, 1989

.

2.2 Flare classifications

There are many classifications of flares, but we focus our attention on the most frequently used. A qualitative classification is based on the flare intensity in the Hα line, in which we distinguish the flares as Faint, Normal or Brilliant, indicated with the letter f, n, and b respectively. In this classification a flare is also distinguished by a number representing its dimension in squared degrees (Tandberg-Hassen and Gordon, 1988) (see Table 2.1).
Another important classification of flares considers the peak flux of SXR emission within 1–8 Å measured by the Geostationary Satellite (GOES), in Wm^{-2}. In this classification a flare is identified by a letter giving the intensity at the peak flux, as reported in Table 2.2, and a number representing the intensity scaling factor (e.g C7.4 means 7.4×10^{-6} Wm^{-2}).

TABLE 2.1: Hα Flare classification.

Hα classification	
Class	Area (Sq. Deg.)
S	<2.0
1	2.0–5.1
2	5.2–12.4
3	12.5–24.7
4	> 24.7

TABLE 2.2: GOES Flare classification .

Soft X-ray classification	
Class	Peak flux in 1–8 Å (W/m^2)
A	$10^{-8} - 10^{-7}$
B	$10^{-7} - 10^{-6}$
C	$10^{-6} - 10^{-5}$
M	$10^{-5} - 10^{-4}$
X	$> 10^{-4}$

Based on their morphology, we can divide flares into two groups, which appear to require quite different physical mechanisms in their formation and evolution process:

- "Simple-loop" or "compact" flare: a single loop enhances its emission in soft X rays and maintains apparently the same shape and location for the whole event, not showing any particle emission (Priest, 1981).
  The simple-loop flares can occur within a large-scale unipolar region or near a sunspot with simple magnetic field configuration, where little excess of magnetic energy is stored.
- "Two ribbon flares": these are much larger and energetic than compact flares and take place near a solar filament located on the PIL in sheared loops. When the filament is located in the quiet Sun, such as a remnant active region, the flare tends to be slow, long-lived and not very energetic, presumably because the magnetic field is relatively weak near such a filament. Active regions with complex magnetic field topology are the place where more energetic flares occur. During the flash phase of a two-ribbon flare, two ribbons of Hα emission form, one on each side of the PIL and during the main phase these ribbons move apart with a velocity of 5 – 20 km s^{-1}. Frequently, they are seen to be connected by an arcade of post-flare loops. Occasionally, the solar filament initially located on the PIL remains intact, but usually it rises and disappears completely. Such a filament eruption begins slowly during the pre-flare phase, and continues in the following phases with a much more rapid acceleration (Priest, 1981).

In Figure 2.3 the evolution of a two ribbon flare in chromosphere in the Hα line (left) and in the corona at 171 Å (right) is reported.

2.3 Standard model

Several observations have provided indications that magnetic reconnection is responsible for the occurrence of flares. Magnetic reconnection is a process where neighbouring magnetic field lines rapidly reorganise themselves into a lower energy configuration (Forbes, 2000). Many observed flares are frequently discussed in the framework of the standard 2D flare model, called the CSHKP model after the names of Carmichael (1964), Sturrock (1966), Hirayama (1974), Kopp, and Pneuman (1976), (Figure 2.4).

The CSHKP model assumes that when a filament rises towards higher layers of the solar atmosphere, the expansion above the filament stretches the magnetic field lines surrounding the flux rope and a current sheet is formed in the coronal layer below the filament. In this current sheet the magnetic field is anti-parallel and reconnects, giving origin to the major dissipation of magnetic energy that heats and accelerates charged particles. These charged particles precipitate towards lower atmospheric layers, where they heat the plasma and cause the ribbons in chromosphere. The newly reconnected field lines have their footpoints at increasing distances with respect to those that have reconnected earlier. Therefore, the separation of the flare ribbons is not a real motion of the plasma, but an apparent shift of the heated footpoints. Moreover, the charged particles heat impulsively the plasma in

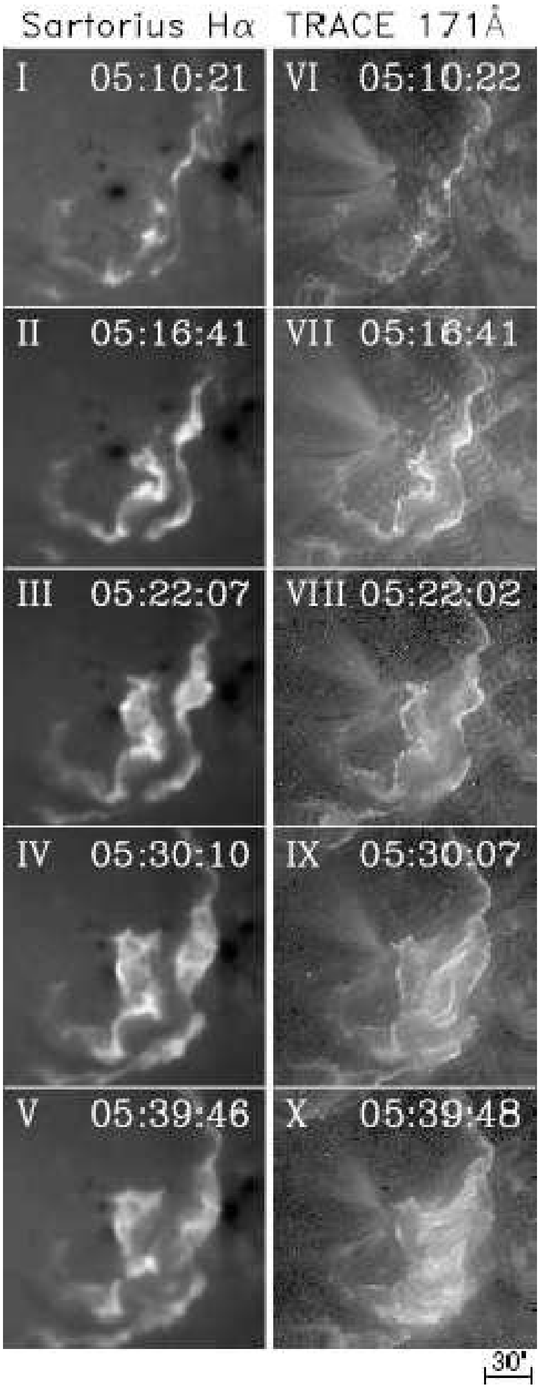

FIGURE 2.3: In chromosphere (left) we note the brightness increase of the two ribbons and their distance that increases with time. Coronal images (right) show two ribbons that matches with the one observed in chromosphere and in the last images the post-flare loops.

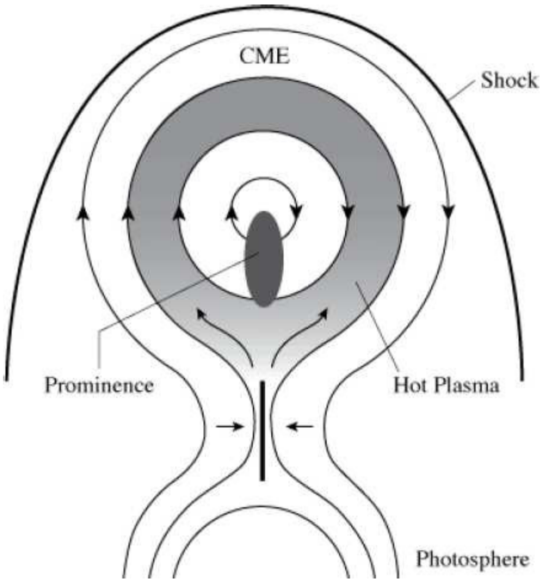

FIGURE 2.4: Schematic representation of the standard flare model, showing the locations of the rising filament /prominence and of the current sheet.

chromosphere that ablates and fill the just reconnected magnetic field lines, giving origin to the observed SXR post-flare loops.

These post-flare loops emit radiation, so they cool down until they show an emission in the EUV range with a temperature ranging from 1 to 2 million of Kelvin. The outer loops are seen in SXR while the inner loops are seen in EUV and later in Hα (see Figure 2.5).

During the last decades many characteristics of this model have been widely confirmed thanks to observations carried out by satellites (SOHO, TRACE, RHESSI, SDO, Hinode). However, there are still many open issues that concern our full understanding of flares. Among these, we can cite the following :

- how the energy, previously stored in a stressed magnetic field configuration, is released on time scale of tens of minutes or hours;
- what is the trigger mechanism that causes the sudden lost of equilibrium;
- how is the energy transported through the solar atmosphere;
- how is the magnetic energy converted into the kinetic energy of the non-thermal particles and into the flare's radiation output;
- why only some flares are spatially and timely correlated with coronal mass ejections;
- how can we forecast the occurrence of these events.

This Thesis is aimed at giving a contribution to provide an answer to the last two items listed above.

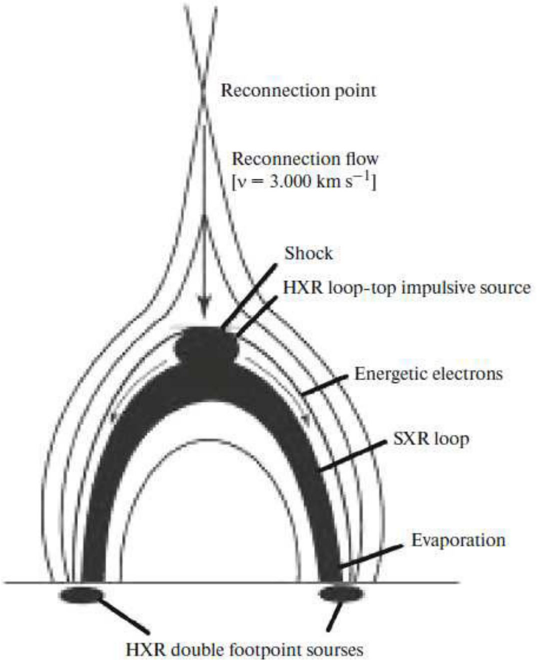

FIGURE 2.5: Schematic view of the 'standard flare' model. Impact of energetic particles provokes evaporation of chromospheric plasma and emission of the post-flare loops in different wavelength ranges.

Chapter 3

Flare occurrence in Active Longitudes

In this chapter we describe our study on the occurrence of C-, M- and X-class flares with known location on the solar disk to search a possible trend of the flares productivity in the active longitudes (ALs), i.e the longitudes that maintain an intense magnetic activity for a long period (Brandenburg and Subramanian, 2005 Ivanov, 2007). We used a dataset provided by GOES covering the cycles 23 and 24 of the Sun.

ALs are regions with high magnetic field concentration that form in well determined longitudes of the Sun (Kitchatinov and Olemskoi, 2005). For instance, sunspots seem to prefer some longitudinal domains when they emerge from the subphotospheric layers (Carrington, 1863). However, the ALs reflect very well not only the sunspot activity, but also the flares occurrence location and the distribution of cap-like structures that usually overlie sunspots, called coronal streamers (Li, 2011 and references therein).

During the solar maximum of cycles 23 and 24, the Sun seemed to show two AL belts separated by 180 degrees, while no AL was clearly detected during the solar minima (de Toma *et al.*, 2000), (Usoskin *et al.*, 2005; Zhang *et al.*, 2011). On the other hand, Gyenge *et al.* (2014) found that the width of belts is 20-30 degrees, and that they are more extended around a maximum and narrower at the minimum.

The simulations of Weber *et al.* (2013) showed that the distribution of the large-scale emerging magnetic field is non-uniform in longitude and exhibits preferred longitudinal belts at low latitudes (between ± 15 degrees), in agreement with the observed behaviour of the ALs.

The period of persistence of the ALs on average ranges from 5-6 months for the AL of short duration, to 1.5-2 years for the AL of long duration (Ivanov, 2003).

Gyenge *et al.* (2016) studied the occurrence of solar flares in ALs and they found that the probability of flare occurrence depends on the separation in longitude between the ALs. Using the data acquired by the Reuven Ramaty High Energy Solar Spectroscopic Imager (RHESSI) and GOES satellites they showed that the majority of flares (about 60%) is located within ± 36 degrees from the ALs. Previously, Zhang *et al.* (2008) discovered that 80% of C-flares at the solar minimum occurs in ALs with half widths of 20-30 degrees.

During the solar maxima, 80% of X GOES class flare occur in ALs (Huang *et al.*, 2013).

However, further studies on flare activity in ALs need to be carried out in order to improve our understanding of this phenomenon. In this scenario, we analyzed the flares registered by GOES during the last two solar cycles in order to search a possible trend of the energy released by flares in ALs.

3.1 Data sample

Using the observations of GOES we collected 21152 C, M, and X-class flares in a time window extending from July 31, 1996, to December 31, 2014, i.e., during the solar cycles 23 and 24. Among these events, we selected 18979 C class flares (89.73%), 2005 M class flares (9.48%), and 168 X class flares (0.79%). We used the archive available at the following link: (ftp://ftp.ngdc.noaa.gov/) in the National Geophysical Data Center (NGDC) in order to acquire some information on these events, such as the initial, peak, and final time of the flares, the class in the X-ray range reported by GOES, the integrated flux that considers the time window between the start and end time of the flares and the occurrence location of the flares on the solar disc. We obtained such information for about 50% (10879 flares) of the initial dataset. More precisely, we know both time and location of 9326 (85.73 %) C-class-flares, 1418 (13.03 %) M-class flares, and 134 (1.23 %) X-class flares.

3.2 Flare Distribution Over the Solar Cycles

Using the dataset relevant to flares of C-, M-, and X-class observed by GOES during the period 1996 – 2014, we determined the total number of flares per year. The result is shown in Figure 3.1 (black line), where we can see two peaks approximately corresponding to the maxima of the solar activity cycles. The maximum of Solar Cycle 23 is quite long: in 2000, 2001, and 2003 we observed about 2500 flares per year. In 2008 we observed only 11 flares: 10 of C class, and 1 of M class.

When we distinguish among the C-, M-, and X-class flares (Figure 3.2) we see that the maxima of the M-class flares occurred in 2002 and in 2014 and that both the C- and the M-class flare distribution have a higher maximum during Cycle 23 than during Cycle 24.

3.3 Results of the analysis on flare occurrence in Active Longitudes

Taking into account the heliographic longitude where each flare occurred and the corresponding peak time, we computed for all (10879) selected flares the Carrington longitude, defined as the angular distance between the observed phenomenon and a reference meridian called Carrington meridian, that rotates at an average velocity of 13.2 degrees. In Figures 3.3 and 3.4 we plot the Carrington longitude of the flares as a function of their peak time for the North and South hemisphere of the Sun, respectively.

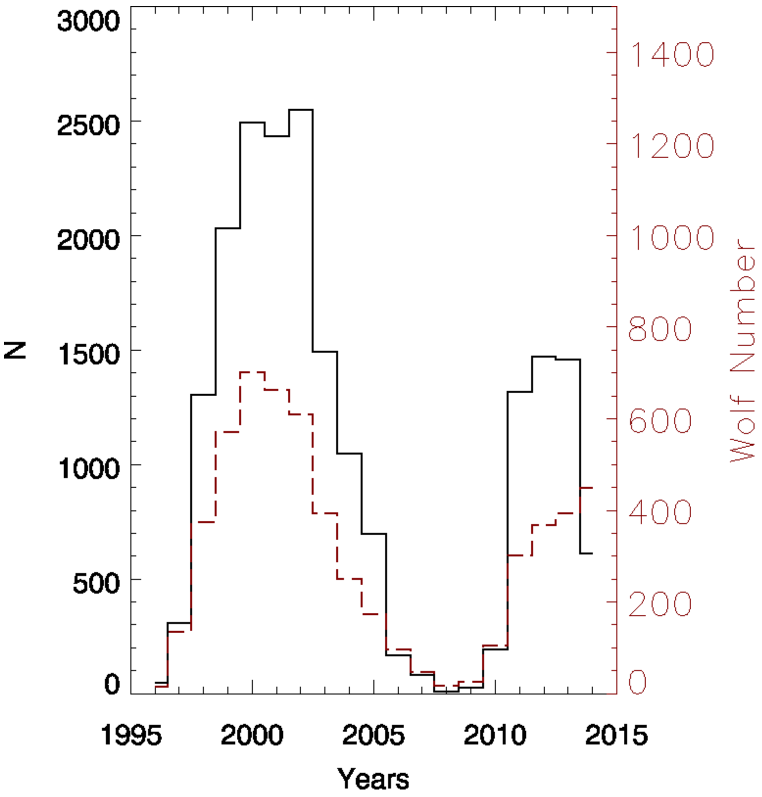

FIGURE 3.1: The black and long-dashed-red line indicate the total flares distribution and the Wolf number in the considered time window, respectively.

We note in all ALs and for both hemispheres two main phases of activity that correspond to the solar maxima of the Cycle 23 and 24, well separated by a period characterized by few flares and low activity, representing the period of minima between the two solar cycles. We also recognize the inhomogeneity of the flare distribution, distinguishing several locations of enhanced activity. However, due to the differences in time scales between the solar cycle and the period of persistence of ALs, from these plots it is not really possible to disentagle any particular trend of flare occurrence in each AL. For the sake of completeness, we mention that some authors also considered the ALs migration with respect to the Carrington reference frame (see Berdyugina, Moss, and Usoskin (2006); Usoskin *et al.* (2005)) and that Zhukov (2012), applying both the methods based on the Carrington longitude and the one based on differential rotation, found that there was not important differences between the two approaches.

Therefore we are confident that our results are not affected by the reference to the Carrington longitude and we can conclude that the spatio-temporal distribution of flares shows several persistent domains of activity, similar to the distribution of the ALs.

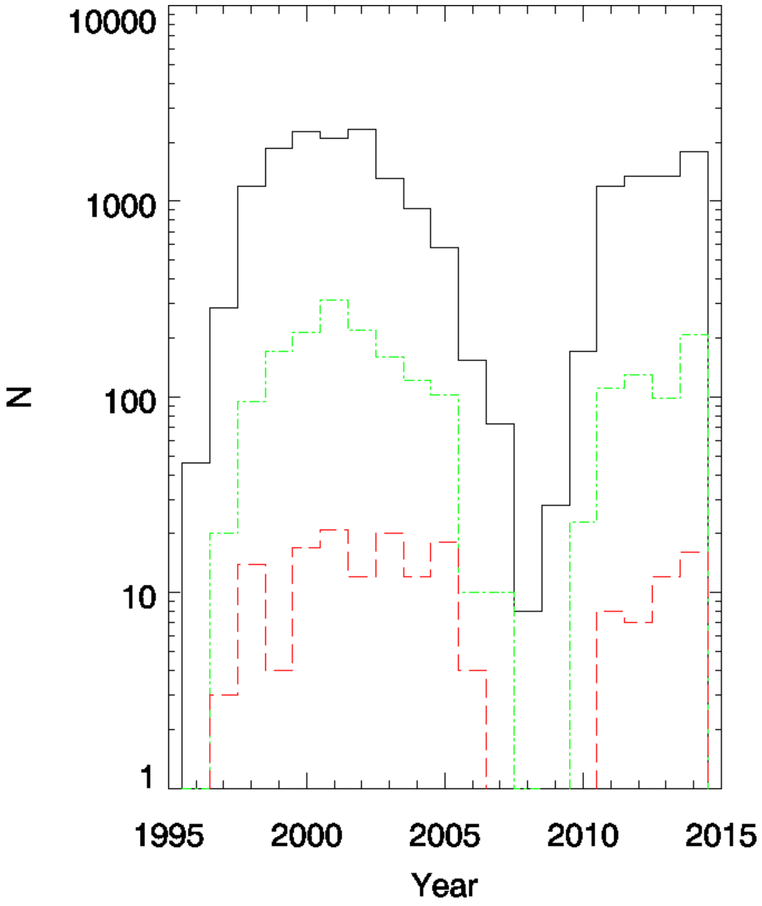

FIGURE 3.2: The black, dot–dashed green, and long-dashed red lines represent the C, M, and X-class flares in the considered time window respectively.

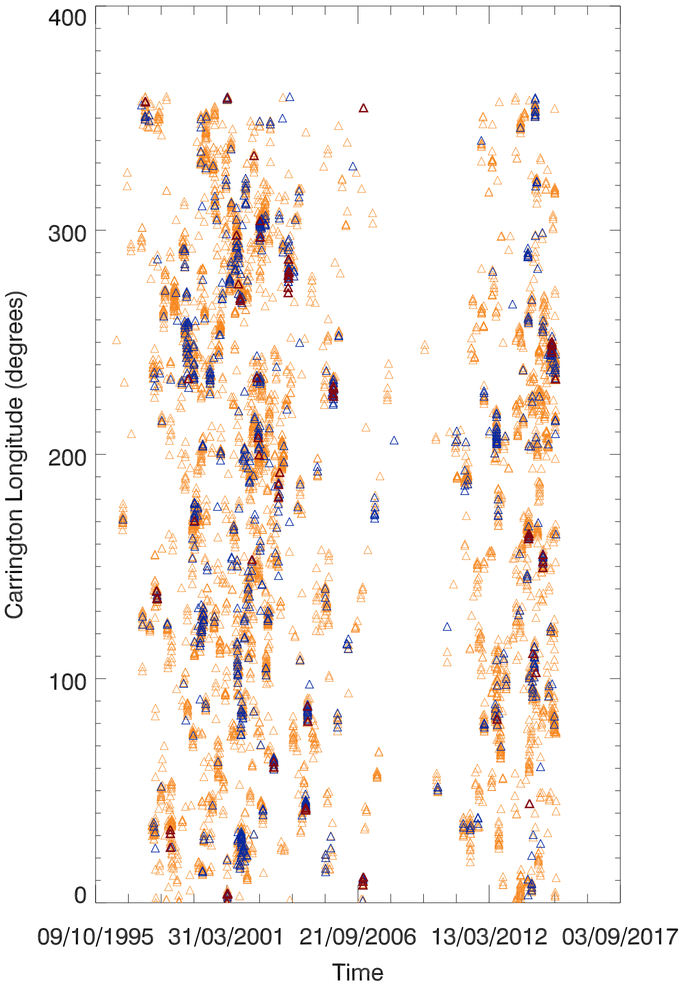

FIGURE 3.3: Carrington longitudes vs time for flares of C (orange), M (blue), and X (red) class for the southern hemisphere.

.

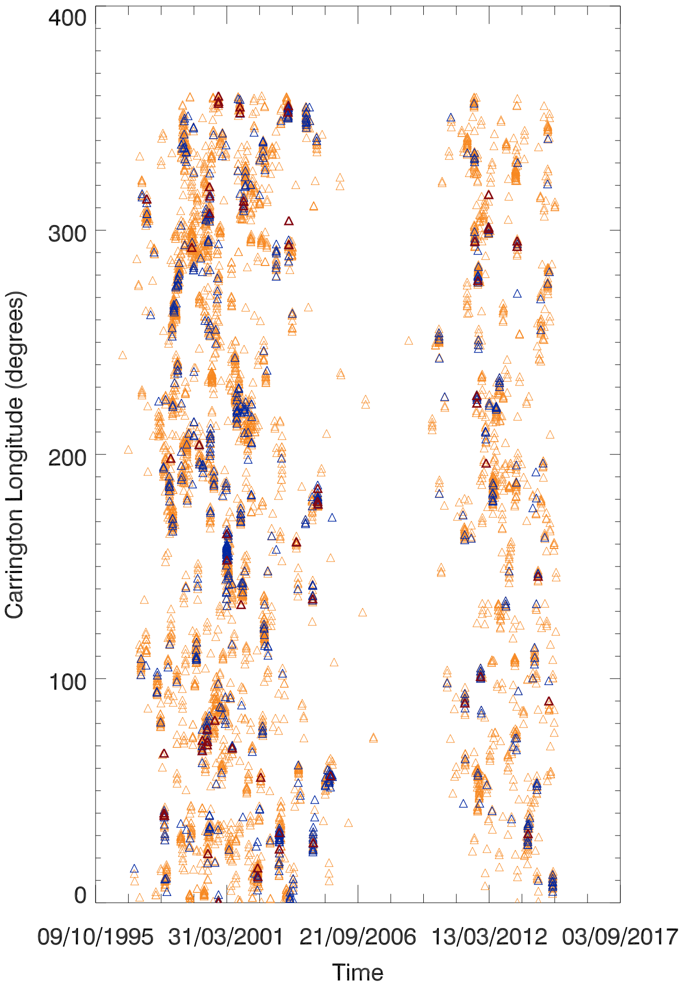

FIGURE 3.4: Same as in Figure 3.3 in the Northern hemisphere of the Sun.

.

We then focused our attention on the energy released by flares in ALs, considering the activity before and after each X-class flare and the AL where it occurred. We considered the peak time of each X-class flare as a reference time (t=0) and we considered the other flares of C-, M-, and X- class that occurred in a time window of 1.3 years (i.e., the average period of persistence of an AL) with respect to t=0. We considered only flares occurred around the Carrington longitude of each X-class flare, i.e.,within ± 18 degrees (see Gyenge *et al.*, 2016). For each day before and after t=0, we computed the mean of the flux peaks of the flares occurred in the AL where the X-class flare was located. The results are reported in Figure 3.5.

The main result is that the most energetic events coincide with the peak of the energy released in the AL within a time interval of about 9 Carrington rotations.

We note a periodicity of about 28 days in the flare activity. We presume that this periodicity may be ascribed to the fact that we observe only the solar disk toward the Earth and that we can investigate the AL activity for about 14 days, i.e., during the AL passage on the solar hemisphere towards the Earth. Therefore, when an X-class flare occurs at the East limb, we are able to analyze only the AL activity during the following 14 days, but it is impossible to obtain information concerning the previous days. Similarly, when an X-class flare occurs at the West limb, we are

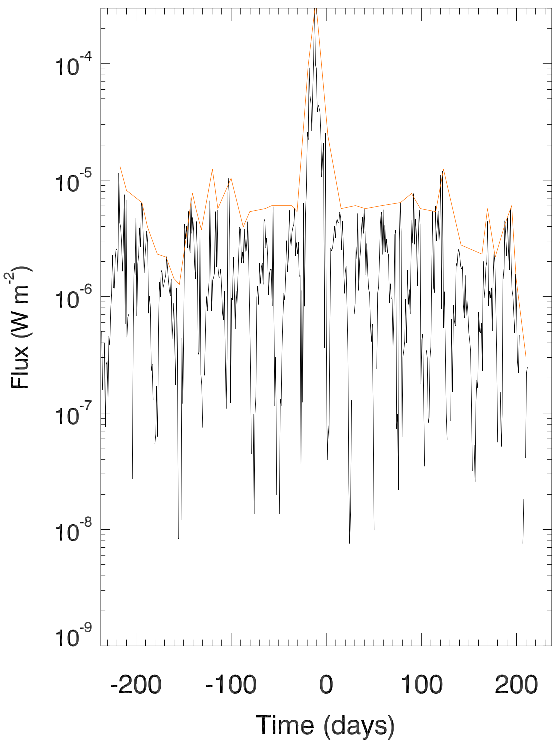

FIGURE 3.5: Mean energy flux released in all ALs where an X-class flare occurred and computed taking into account all C-, M-, and X-class flares. t=0 corresponds to the peak time of X-class flares.

.

able to analyze only the AL activity during the preceding 14 days, but we do not have any information about the following days. In this way we underestimate the AL activity at the edges of the period of 28 days, corresponding to a Carrington solar rotation. Moreover, we note that there are also days with no flare observation (these days correspond to the discontinuities in the plot line of Figure 3.5).

Considering the maxima of energy flux for each Carrington rotation (see the red line in Figure 3.5), we clearly see that the energy released during the solar rotation when the X-flare occurs is one order of magnitude greater than the previous and the following rotations.

If we analyse the flare activity in the ALs reducing the region of interest not only in longitude but also in latitude, i.e., considering only the flares occurred within a heliographic latitude of ± 10 degrees from the X-flare, we obtain the plot shown in Figure 3.6. In this case we see that the ALs where the X-class flare occurs are characterized on average by a phase of increase and a phase of decrease of the energy delivered by the other events before and after the stronger events respectively, i.e. during the Carrington rotations which precede and follow the rotation at t=0, respectively (see the red line in Figure 3.6). These phases of increase and decrease of the released energy in the AL last about 4-5 Carrington rotations.

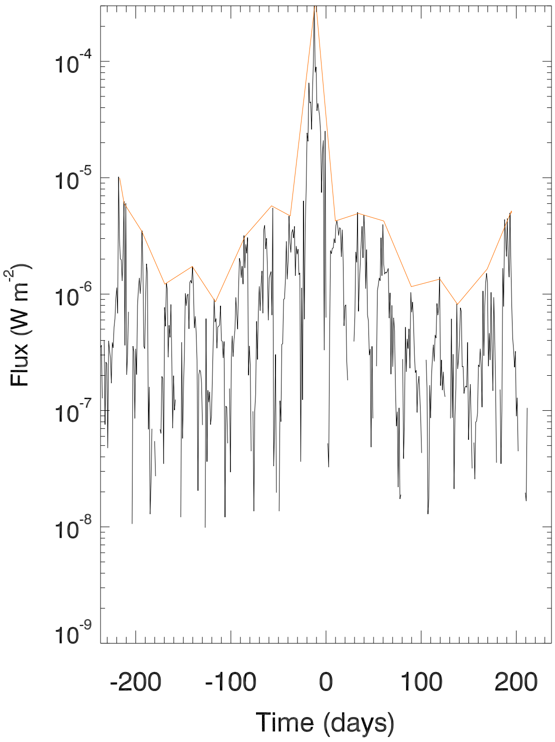

FIGURE 3.6: Mean energy flux released in all regions (± 18 degrees in longitude and of ± 10 degrees in latitude) where an X-class flare occurred and computed taking into account all C-, M-, and X-class flares. t=0 corresponds to the peak time of X-class flares.

.

We also computed the flux emitted in 0.1 − 0.8 nm range, from the beginning to the end of each flare. Taking into account this quantity we obtained the plot of Figure 3.7. In this case we still see the phase of increase of the energy released in the ALs during the 4 Carrington rotations which precede the X-class flares, and comparing the peaks of Figures 3.5 and 3.6 to the ones of Figure 3.7, we see an increase in the energy released by the flares of about a factor 5.

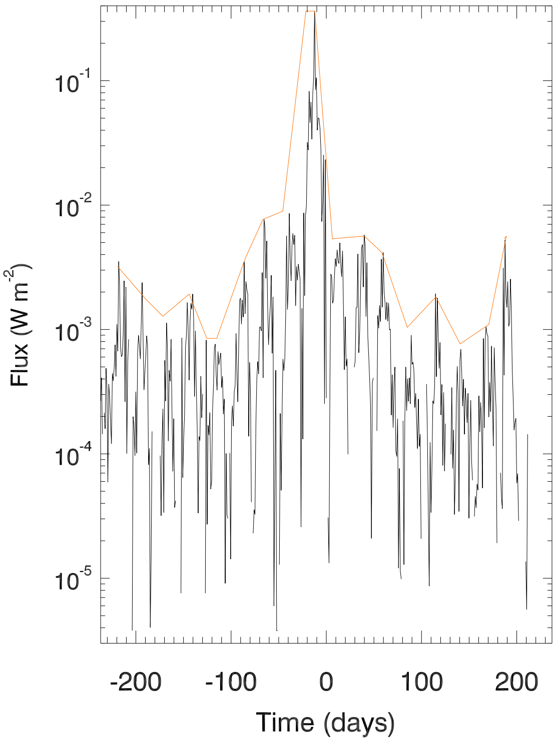

FIGURE 3.7: Mean energy flux released in all regions (± 18 degrees in longitude and of ± 10 degrees in latitude) where an X-class flare occurred and computed considering the integrated flux of each flare from their beginning to their end time. t=0 corresponds to the peak time of X-class flares.

.

We underline the differences in the release of energy during the solar rotation by considering the region within ± 18 degrees in longitude and ± 10 degrees in latitude, when the X-flare occurs. This difference is one order of magnitude greater than the Carrington rotations which precede and follow the peak at t=0 (see Figure 3.8). Restricting our analysis to 3 solar rotations centered on the peaks of the X-class flares (Figure 3.8) we found that there is a difference of an order of magnitude in the energy flux delivered by the ALs in their previous and following solar rotations with respect to the one at t=0.

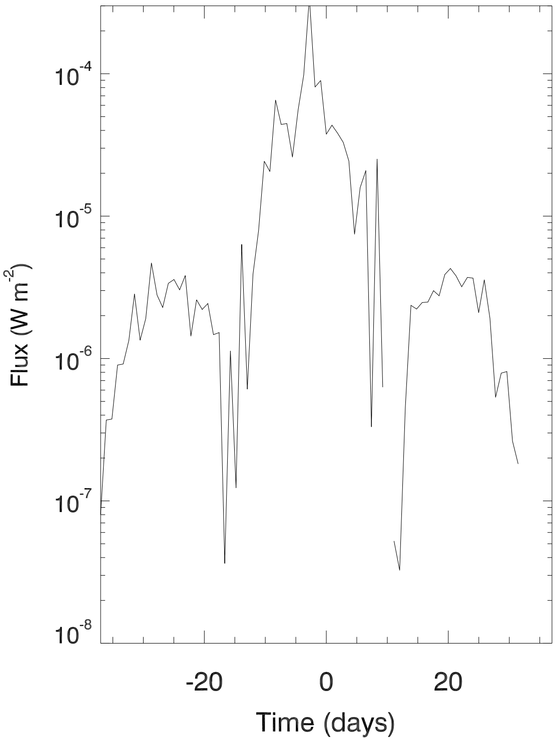

FIGURE 3.8: Zoom of the plot reported in Figure 3.5, limited to a time interval of about 3 solar rotations.

3.4 Summary

In this Chapter we analyzed the flares occurrence in Active Longitudes (ALs), over the solar cycles 23 and 24 in order to investigate the existence of a possible correlation between flares locations and ALs and/or a trend of the energy delivered by these events. We found that the spatial distribution of the flares shows several persistent domain of activity. Moreover, the most energetic events coincide with the peak of the energy released in the AL within a time interval of about 9 Carrington rotations. We also noted a periodicity of about 28 days in the flare activity. We presume that this periodicity may be ascribed to the fact that we observe only the solar disk toward the Earth.

The analysis of the flare activity in the ALs performed by reducing the region of interest not only in longitude but also in latitude showed that the ALs where the X-class flare occur are characterized on average by a phase of increase and a phase of decrease of the energy delivered by the other events before and after the stronger events. These phases of increase and decrease of the released energy in the AL last about 4-5 Carrington rotations.

Chapter 4

Coronal Mass Ejection: observations and models

During the last decades Coronal Mass Ejections have been extensively studied, due to the complexity of phenomena that take place during their occurrence, and also because the plasma ejected from the Sun and impacting spacecrafts and planets along its path, can have an important role in the framework of Space Weather.

In this respect, it is important to analyze the temporal and spatial relationships among flares and CMEs. The relationship among these phenomena is in fact still unclear and presents some difficulties due to the fact that the coronagraphs, occulting the solar disk, do not allow us to observe the source region where the initial eruption takes place.

In this section we give a brief introduction on CMEs (more detailed reviews can be found in Webb and Howard 2012, Chen 2011).

4.1 CME morphology and physical parameters

CMEs can be observed using coronagraphs: instruments that occult the bright photosphere and allow us to investigate the CMEs structure and evolution. Moreover, the possibility offered by the STEREO satellites to obtain a stereoscopic view of these events has greatly improved our knowledge on these phenomena (see, e.g., Dolei *et al.*, 2014).

Usually CMEs present an internal structure that can be divided into three parts. From the outermost to the innermost feature, we find: a bright circular edge, called **leading edge** or bright front, which surrounds a dark region (*the cavity*), that contains a brilliant eruptive prominence, that represents the *bright core* (see Figure 4.1) (Low, 1984; Low, 1990; Hundhausen *et al.*, 1984). CMEs may also exhibit more complex structures (Pick, 2006) or can be without the circular edge, as is the case of the *narrow* CMEs, which are characterized by a jet-like structure along open magnetic field lines.

Sometimes CMEs can occur in close succession, giving rise to the so-called *multiple coronal mass ejections* whose genesis in an asymmetric coronal field configuration has been studied by Bemporad *et al.* (2012).

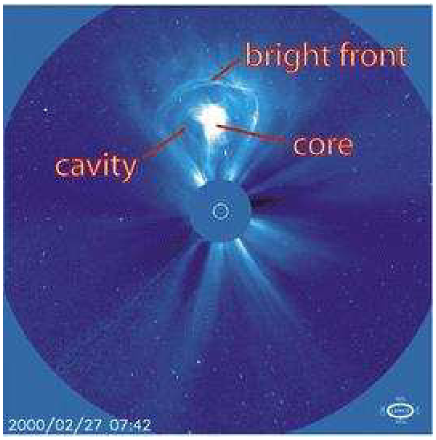

FIGURE 4.1: Example of a CME showing the bright front (or leading edge), the cavity and the core. The CME was observed by LASCO–C3 coronagraph onboard of SOHO spacecraft (Riley *et al.*, 2008)

.

Sheeley *et al.* (1999) classified the CMEs, directed approximately along the line of sight (LOS), in two different classes depending on whether their height/time profiles increase or decrease: the gradually accelerating CMEs and the fast decelerating CMEs.

The core and the leading edges of the gradually accelerating CMEs are characterized by an almost constant acceleration, ranging between 8 and 40 m s^{-2}, and reach speeds of 600 to 1300 km s^{-1} (Sheeley *et al.*, 1999). When gradually accelerating CMEs are observed along the LOS, they are generally seen as regular halos that surround the coronagraph disk. Away from the Sun, gradually accelerating CMEs slowly disappear reaching a constant velocity. Some gradual CMEs that are Earth directed are associated to geomagnetic storms and interplanetary shocks.

Impulsive CMEs, or fast decelerating events, are often associated with flares and Moreton waves (impulsive disturbances observed in the wings of the Hα line, propagating at speeds ranging from 10^2 to 10^3 km/sec) occurring on the visible disk of the Sun. They are characterized by a velocity higher than 750 km s^{-1} and show irregular leading edges with a high ragged fine structure. They show a high deceleration and in 1 hour they reduce their velocities from 1000 to 500 km s^{-1}. Examples of gradual and impulsive CMEs are shown in Figure 4.2.

Figure 4.3 reports a sequence of images showing the evolution of a CMEs characterized by an angular width greater than 120°.The coronal image shown in Figure 4.4, (top panel) exhibits a CME occurring on the backside of the Sun, that does not present a component able to hit the Earth. Figure 4.4, (bottom panel) shows a CME occurring on the visible side of the Sun.

4.2 Models for CMEs initiation

Several models have been proposed to explain the initiation of CMEs. Usually in these models the pre-eruption state of the coronal magnetic field is stressed beyond

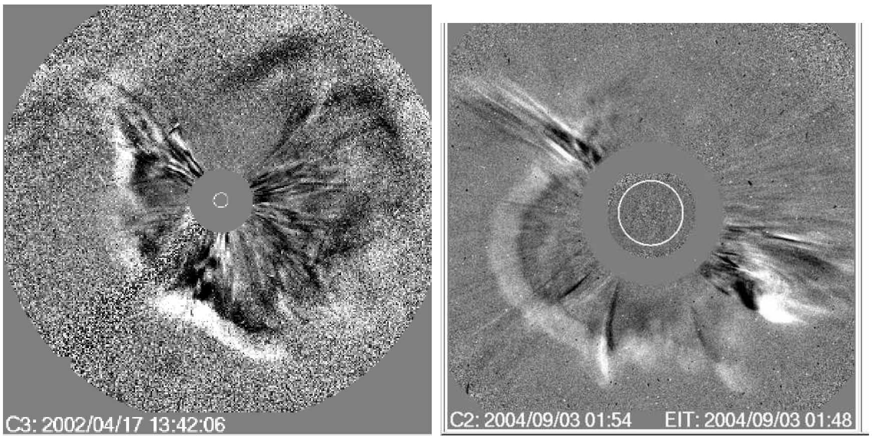

FIGURE 4.2: Left: Gradual CMEs. Right: Impulsive CMEs.

its minimum energy configuration and the magnetic field is in a force-free field configuration.

In the following we present a brief overview of these models.

The thermal blast model: First CME models were based on the hypothesis that the increase of thermal pressure gradient produced by a flare in a stressed magnetic field could be the cause of their occurrence. This phenomenon is similar to the overlying pressure created by a bomb (Dryer, 1982 and Wu, 1982). However, it is now well known from the observations that there are many CMEs not associated with flares and others that are followed by flares (Gosling, 1993). A schematic cartoon of this model is shown in Figure 4.5.

The mass loading model: In this model a mass located in chromosphere or corona, represented by a large filament/prominence, exerts its weight on a magnetic arcade, stressing the magnetic field lines as a compress spring. A CME occurs when the mass slips off, releasing the stressed magnetic field lines, as could occur in a spring without weight on it. A schematic view of this model is shown in Figure 4.6.

The Tether Release, Tether Cutting and flux cancellation models: The Tether Release Model takes into account a possible break of the equilibrium between the magnetic tension (downward) and magnetic pressure (upward) in a magnetic arcade. The magnetic field lines that provide the magnetic tension are called tethers. This model can be sketched with many ropes that compress a spring and a mass over the spring. When these ropes are released or they are cut, the tension of the system above the spring increases. After a certain period of time, the spring becomes unable to keep its position and then, it releases the mass abruptly causing a CME eruption. The main difference between the tether cutting and the tether release model is that in the latter the stress on the tethers gradually increases because of external forces which will cause it to break. van Ballegooijen and Martens (1989) pointed out that the cancellation of magnetic flux near the neutral line of a sheared magnetic arcade would produce helical magnetic field lines, i.e., flux ropes. This configuration can support a filament, but if magnetic flux cancellation takes place, the filament can be erupted, giving rise to a CME. It is worthwhile to stress that the tether cutting and the flux cancellation models are quite similar, being both based on reconnection, but while the latter is related to a more gradual evolution occurring in the photosphere, the former is more impulsive and occurs in the low corona. A schematic view of

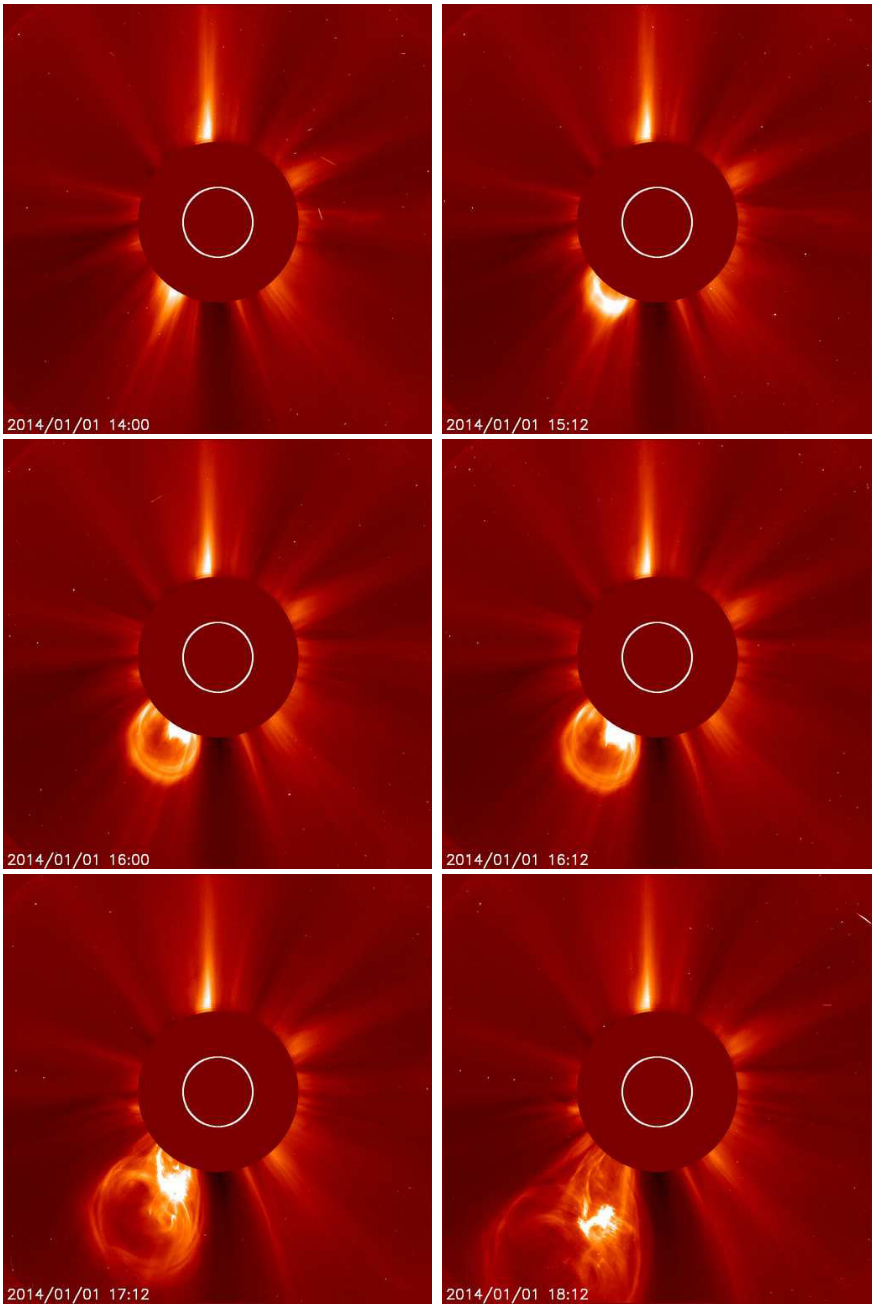

FIGURE 4.3: Example of a partial halo CME evolution observed the 1st Jan 2014 using the LASCO–C3 coronagraph onboard of SOHO spacecraft. The event started at 14:00 UT and ended at 19:15 UT. Note that a partial halo CME during its eruption does not cover the whole coronagraph disk.

these models is shown in Figure 4.7.

The Breakout model: The Magnetic Breakout Model, proposed by (Antiochos, DeVore, and Klimchuk, 1999) is based on a multipolar magnetic field configuration, where a slow and gradual reconnection at a neutral point between a sheared arcade and neighboring flux systems triggers the eruption. A schematic view of this model is shown in figure 4.8.

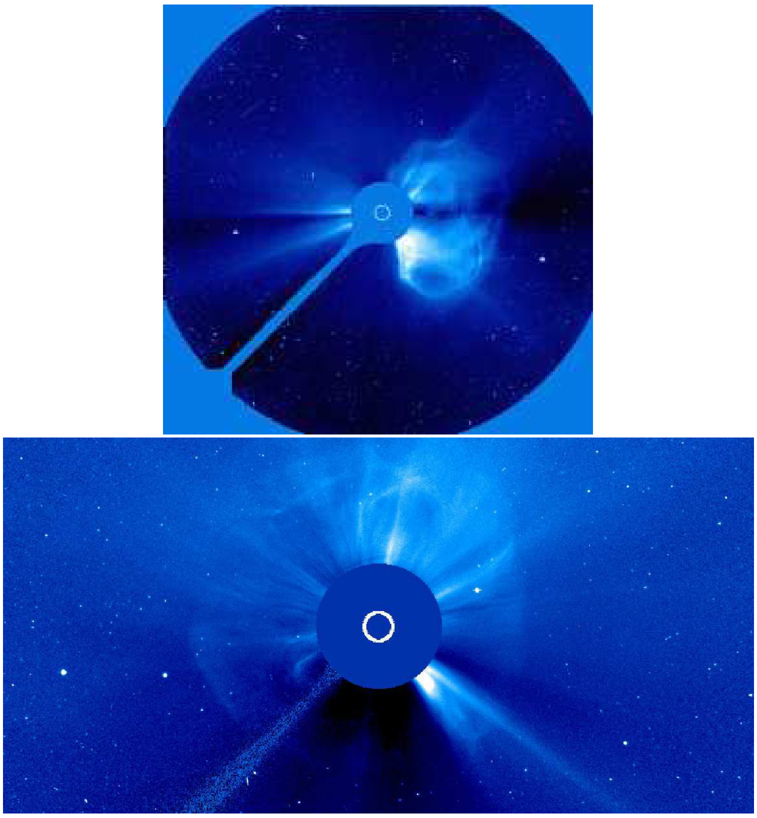

FIGURE 4.4: Top: Example of Backside CME. Bottom: Frontside halo CME observed the 22th June 2015 at 18:24 UT. This event is associated with two flares of class M2.0 and M2.6 respectively.

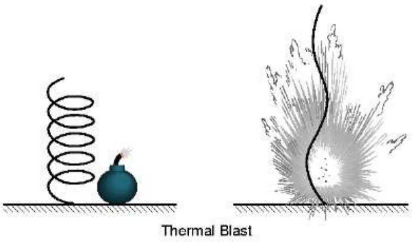

FIGURE 4.5: Thermal blast model evolution (Aschwanden, 2005)

.

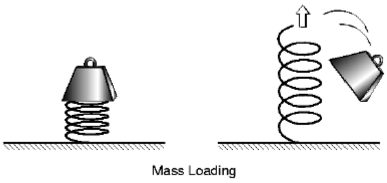

FIGURE 4.6: Mass loading model evolution (Aschwanden, 2005)

.

The flux rope model: In this model the initiation of the CME consists of two phases: photospheric shearing and flux emergence that lead to the formation of a

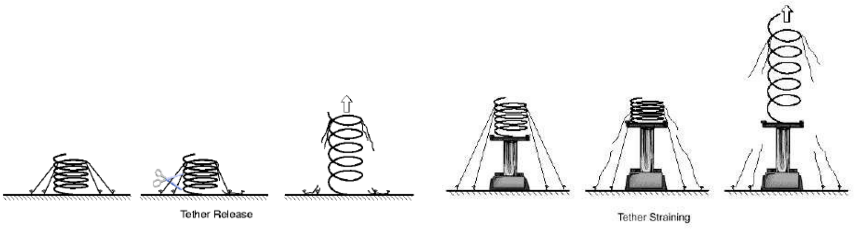

FIGURE 4.7: Tether release (left panel) and tether cutting (right panel) models evolution (Aschwanden, 2005)

.

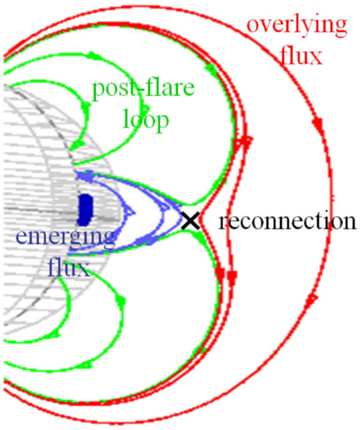

FIGURE 4.8: Breakout model. The magnetic reconnection at a neutral point removes the constraint over the flux rope and allows the eruption (Antiochos, DeVore, and Klimchuk (1999))

.

twisted flux tube. The pre-eruption configuration consists of an infinitely long flux rope and an overlying arcade. When the flux rope starts to rise, the magnetic field lines will reconnect below it, forming some magnetic islands (Forbes, and Isenberg, 1991).

The Flux injection model: In this model the destabilization of the magnetic field is caused by fast footpoint shearing motion, giving rise to an increase of the stored magnetic energy. In particular, the mechanism called flux injection occurs when the magnetic field footpoints remain anchored in photosphere and new magnetic flux emerges (Krall, Chen, and Santoro, 2000).

4.3 The state-of-the-art on statistical studies of CMEs parameters

Ivanov and Obridko (2001) carried out an analysis on the semi-annual mean CMEs velocities in the time window 1979 – 1989 and they found a complex cyclic variation that presents two peaks. The first one is located at the maximum of the solar cycle. The second one, called secondary, is present at the solar cycle minimum. Ivanov and

Obridko (2001) stated that the peak at the minimum of solar cycle in a time window ranging from 1985 – 1986 could be attributed to the conspicuous contribution of fast CMEs that have an angular width around 100° at solar cycle minimum. This significant contribution leads to an increase of the global magnetic field observed at large scale in our Sun. Moreover, they highlighted that on average, an increase of the velocity always provokes the growth of the CMEs width.

More recently, Mittal *et al.* (2009a) reported on the analysis of more than 12900 CMEs observed by the LASCO coronagraph onboard SOHO in the time interval 1996 – 2007. Their results indicate a decrease in the velocity in the descending part of Solar Cycle 23. In the year 2001 was observed an unexpected decrease in the velocities of the CMEs and a peak, that corresponds to the Halloween events in 2003, where many CMEs, flares of X class, shocks and Solar Energetic Particles (SEP) events were observed in October and November 2003.

Using the same dataset, Mittal and Narain (2009b) found that the majority of CMEs (66 %) present negative acceleration, while the CMEs with positive acceleration are the 25 % and the other showed a lower acceleration (9 %) in the external coronal layer.

Cremades and St. Cyr (2007) studied the latitudes of CMEs using a wide sample, since 1980 up to 2005, in order to investigate the possible matches between CMEs and coronal streamers location. They found a good correlation, in agreement with Hundhausen (1993) (see also Gopalswamy *et al.*, 2004).

All these studies have allowed significant steps forward in the comprehension of the CMEs properties, but there are still several open issues, like for instance a clear explanation of why CMEs can have different velocities and acceleration regimes, the reasons of the observed variation of these parameters along the solar cycle, why some CMEs are clearly correlated with flares while others do not seem to show any correlation.

The following Chapters 5 and 6 will describe the research carried out in this Thesis in order to provide a further contribution to the solution of these open problems.

Chapter 5

Statistical analysis on selected CME's parameters

This chapter reports a statistical study of some CMEs parameters and their variation over the Solar Cycles 23 and 24 (Compagnino *et al.*, 2017).

5.1 LASCO and CACTus datasets

The CMEs data analyzed in this thesis were acquired by the LASCO C2 and C3 coronagraphs onboard the SOHO satellite in a time interval extending for 18 years, from 31 July 1996 to 31 March 2014. We used two different datasets: the former obtained from the Coordinated Data Analysis Workshops (CDAW) Data Center online CME catalog, available at the following link: cdaw.gsfc.nasa.gov/CME_list and the latter through the Computer Aided CME Tracking software (CACTus) available at the following link: sidc.oma.be/cactus/. Using two different catalogs we could compare the results obtained through the manual identification method for CMEs detection (CDAW) with the automated identification by CMEs tracking (CACTus).

The CDAW catalog includes information about several CMEs parameters: the polar angle (PA) i.e., the mean angle within the two external edges of the CME width measured in degree on the plane of the sky counterclockwise from the North direction, the linear velocity, the acceleration, the width, the mass and the energy of the CMEs. Some of these parameters are also reported in the CACTus dataset, which however does not contain information about the CMEs mass, energy and acceleration. It is worth noting that the CME start time recorded in these datasets indicates the first CME detection in the LASCO C2 Field of View (FOV), i.e the region ranging from about 2.0 to 6.0 solar radius. The events in the CDAW catalog are 22876 (616 halo CMEs, *i.e.* 2.69 % of all CMEs), while the events in the CACTus catalog are 15515.

5.2 CME Parameters Over the Solar Cycles 23 and 24

The annual CMEs occurrence during the solar cycle 23 and 24 is shown in Figure 5.1 (the black line represents the CACTus data, while the dot–dashed blue lines represents the CDAW data).

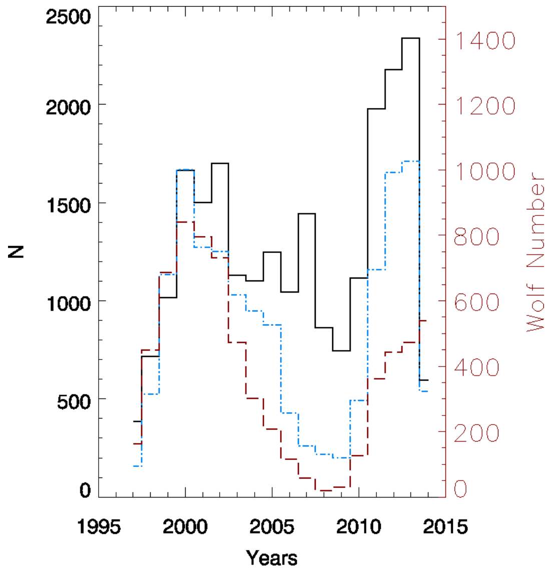

FIGURE 5.1: Number of observed CMEs for each year observed in the considered time widow for CDAW (black line) and CACTus (dot–dashed-blue lines). The yearly Wolf Number is marked by long-dashed-red line

.

We observe two sharp peaks referred to the maxima of the solar cycles 23 and 24. We note that the analysis carried out using the CDAW dataset shows a higher peak related to the occurrence of the CMEs in the cycle 24. This behaviour seems to be in contrast with the weaker magnetic activity observed during the current solar cycle than in solar cycle 23, as already noted by Tripathy, Jain, and Hill (2015), and shown in Figure 5.1 by the yearly Wolf number (long-dashed-red line). As mentioned in the analysis and measurement of the acoustic solar modes frequency shifts in the two cycles carried out by Tripathy, Jain, and Hill (2015) the weakness of the peak in the solar cycle 24 may be attributed to faint polar field strength observed in solar cycle 23. A very low solar magnetic field during the cycle 24 is also documented by the sunspot number (SSN). This activity is the lowest recorded from the space age inception until now and several authors make the hypothesis of a global minimum in solar cycle 24 (Padmanabhan *et al.*, 2015; Zolotova and Ponyavin, 2014).
Moreover, using the CMEs detected by CACTus we note that the number of CMEs occurred each year (N) is of the same order of magnitude during the peaks of the two cycles, and that the peak of CME distribution during the Cycle 24 is more extended in time ($N > 1500$ during 2012 and 2013). Another important conclusion is that the differences between CDAW and CACTus may be due to different CME definition in the CDAW catalog that lead to an observed bias in CMEs detection (Robbrecht, Berghmans, and Van der Linden, 2009; Webb and Howard, 2012; Yashiro, Michalek, and Gopalswamy, 2008).

In Figure 5.2 (from top to bottom) we show the behavior of the average annual velocity, acceleration and angular width for all the observed CMEs during the Solar Cycles 23 and 24. For the velocity and the angular width we plot the results of CDAW dataset (black line) and of CACTus dataset (dot–dashed-blue line), while for the acceleration we show only the CDAW results because this parameter is not available in the CACTus dataset. The blue diamonds indicate the CACTus data.

We calculate the CME annual mean velocity by considering the total number

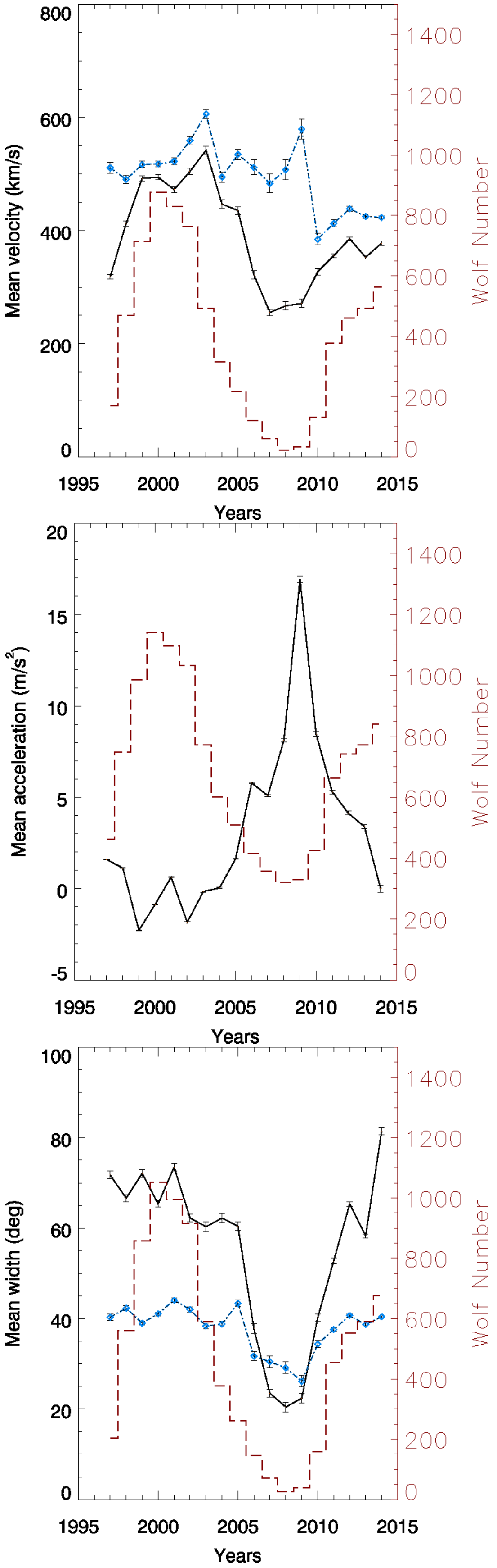

FIGURE 5.2: Mean CME velocity distribution for each year (top panel), acceleration (middle panel,) and angular width (bottom panel) in a period that covers the time window between 1996 and 2014. The results for CDAW are indicated by a black line, while for CACTus dataset dot–dashed-blue lines are used. In each panel the yearly Wolf Number is marked by long-dashed-red line. The CACTus data are indicated by the blue diamonds.

of CMEs for each year and then considering the velocity averaged with respect to this number. The same procedure was applied for the other parameters. We also computed the error bars for the mean distribution of these quantities, as $\sigma/\sqrt{N}$, where σ is the standard deviation of the corresponding quantity and N is the number of CMEs that occurred in each year (see Aarnio *et al.* (2011)). The error bars are smaller than the symbol sizes, although the error for the acceleration is dominated by the uncertainty of the individual measurements. The red line in each panel shows the yearly Wolf number. For the average velocity we can see a first peak around 2003 and a second one between 2012 and 2014 in both of the datasets.

The behaviour of both of the datasets reflects the solar-activity cycles and can be interpreted according to Qiu and Yurchyshyn (2005) as an effect of the magnetic flux involved by the events during the solar maxima. However, one difference between the two datasets is that in the mean-velocity distribution of the CMEs detected by CACTus there is another peak between 2008 and 2010, during the minimum of the solar cycle. A secondary peak was reported by Ivanov and Obridko (2001) from the analysis of CMEs velocities for the time interval 1979 – 1989, and was interpreted by these authors as due to a significant contribution of fast CMEs ($V > 400$ km s^{-1}) with a width of $100°$.

The mean CMEs acceleration for CDAW is $3.2\pm$ 0.3 m s^{-2}. In the distribution of the CME average acceleration (middle panel of Figure 5.2) we see negative values around the maximum of Solar Cycle 23 and a peculiar peak of about $15\pm$ 3 m s^{-2} in 2009. We note that this peak occurs approximately when we observe the minimum in the annual average velocity distribution for CDAW and the second peak of the velocity distribution for CACTus. However, statistically the slower CMEs occurring during solar-activity minimum, are characterized by higher positive values of acceleration.

In Figure 5.2 (bottom panel), showing the mean angular width, the values in the years 2000 – 2003 for CDAW dataset ($\approx 20°$) suggest that on average the narrowest CMEs are the slowest ones (compare with Figure 5.2 (top panel)) (Yashiro, Michalek, and Gopalswamy, 2008). We also note that for the CACTus dataset the fastest CMEs are the narrowest (Yashiro, Michalek, and Gopalswamy, 2008). Both datasets show a minimum in the mean width distribution over the years corresponding to the minimum of the solar cycle, although Yashiro, Michalek, and Gopalswamy (2008) found that the CACTus catalog has a larger number of narrow CMEs than CDAW. This difference in the two samples determines a different amplitude in the range spanned by the mean angular width distribution, *i.e.* in the CACTus catalog the mean width varies from $\approx 30°$ during the minimum of solar-activity to $\approx 40°$ during the maximum of activity, while for CDAW catalog varies between $\approx 20°$ and $\approx 80°$.

In order to further analyze the properties of CMEs during the descending part of the Solar Cycle 23, in Figures 5.3, 5.4, and 5.5 we show the distribution of the velocity, acceleration and width of the CMEs for each year from 2000 to 2006.

Figure 5.3 shows that the tail of the distribution of the CME velocity observed during the descending part of the solar cycle 23 decreases from the maximum (2000) to the minimum (2006) of the cycle. This means that most of the fastest CMEs velocities ($>$ 1000 km s^{-1}) occur during the maximum of the solar cycle, when the amount of magnetic field emerged in the atmosphere reaches higher values. The average

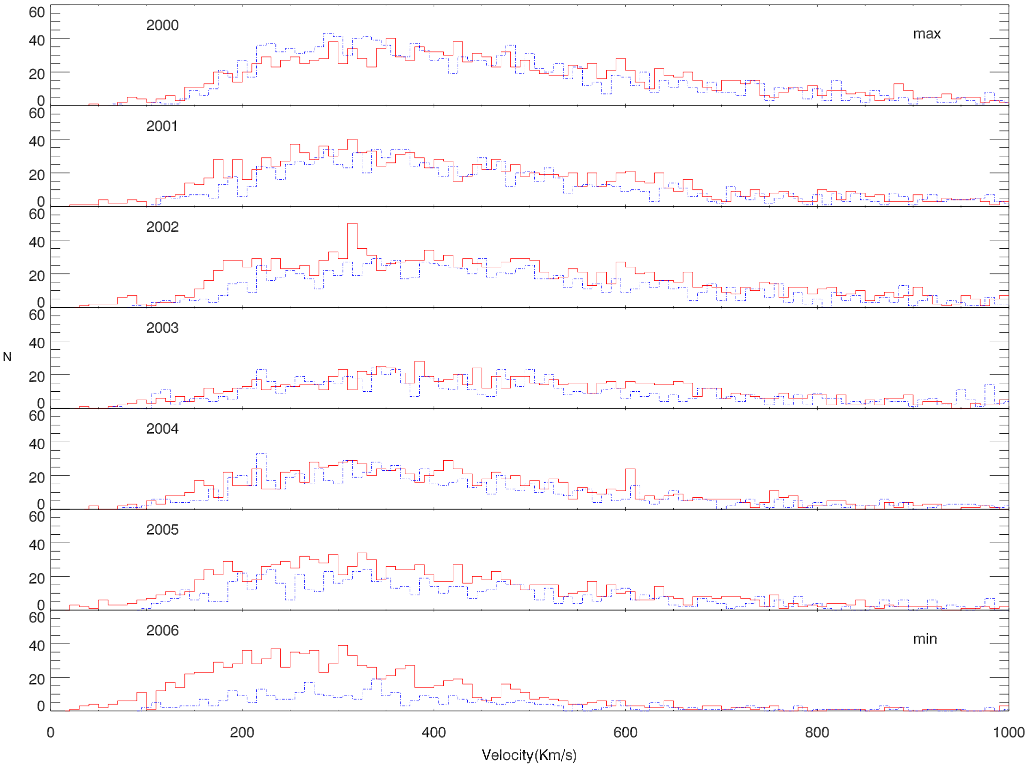

FIGURE 5.3: Distribution of CMEs velocity year by year in a time interval ranging from 2000 to 2006. The red and dot–dashed-blue line indicate CDAW and CACTus data respectively.

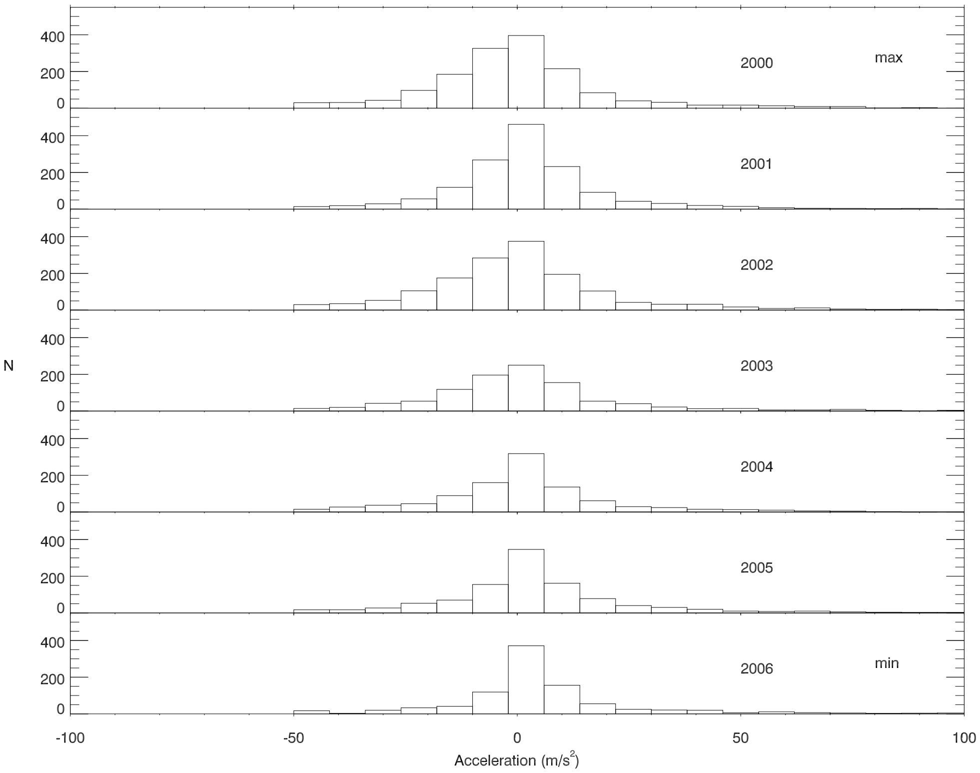

FIGURE 5.4: Distribution of CMEs acceleration year by year in a time interval ranging from 2000 to 2006.

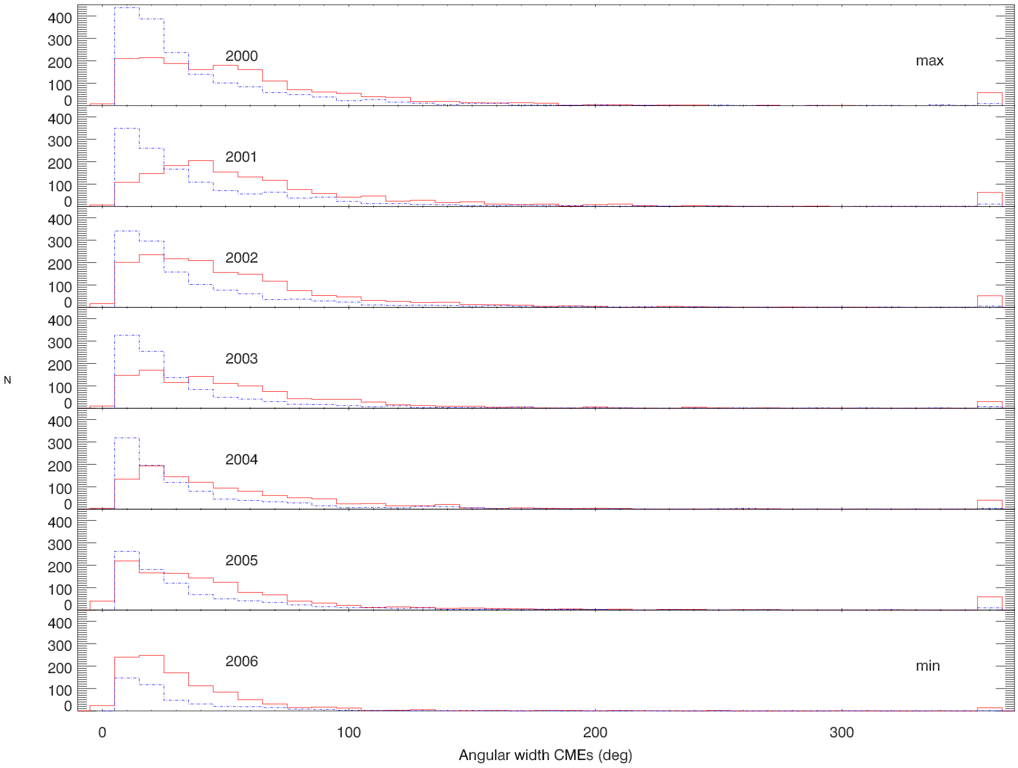

FIGURE 5.5: Distribution of CMEs width year by year in a time interval ranging from 2000 to 2006. The red and dot–dashed-blue line indicate CDAW and CACTus data respectively. Halo CMEs are presented in the latter bin.

velocity of the CMEs for CDAW during these years is 396.3 ±2 $\mathrm{km\,s^{-1}}$, where this uncertainty is the standard deviation of the mean, while the mean velocity for CACTus dataset is 491.8 ±2.7 $\mathrm{km\,s^{-1}}$. We also remark that Fig 5.3 shows only a few CMEs characterized by velocities $\geq$ 600 $\mathrm{km\,s^{-1}}$ (note that in these plots the velocities are not averaged on each year as in the top panel of Figure 5.2).

The CME accelerations in each year (Figure 5.4) are distributed mainly between -50 $\mathrm{m\,s^{-2}}$ and 50 $\mathrm{m\,s^{-2}}$, and few events are characterized by higher values during the solar cycle maximum. We note an increase of the difference between the negative and the positive accelerations while the solar activity decreases. Therefore, the average acceleration per year is mainly negative during the years of higher activity and is positive during the minimum of the solar cycle, as already shown in Figure 5.2 (middle panel).

The angular-width distribution (see Figure 5.5) shows that on average for CDAW the narrower CMEs are slower and the majority of the CMEs are characterized by an angular width lower than $100°$. $\pm$ $0.4°$ We note that the CACTus dataset presents a greater number of CMEs narrower than $40°$ and a smaller number of CMEs wider than $40°$ in comparison with the CDAW dataset (see Yashiro, Michalek, and Gopalswamy, 2008).

The mean angular sizes (latitudinal extents) projected against the plane of the sky of all CMEs of the CDAW dataset is $55.8° \pm 0.4°$, *i.e.* slightly greater than $50°$ as found by Cane (2000). The mean CMEs width for CACTus dataset is $39.5° \pm 0.4°$. Only during the solar cycle maximum (2000 and 2001) we observe a significant

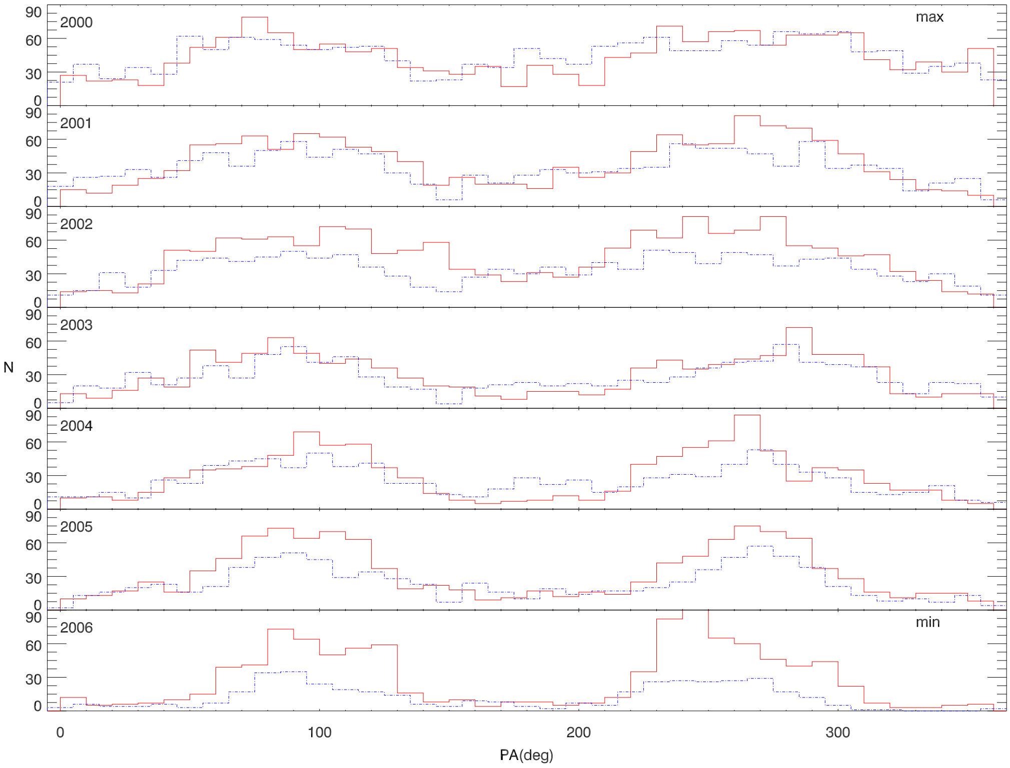

FIGURE 5.6: Distribution of CMEs polar angle (PA) year by year in a time interval ranging from 2000 to 2006. The red and dot–dashed-blue line indicate CDAW and CACTus data respectively. This quantity give information on the CMEs propagation direction and is measured counter-clockwise in degrees from Solar North.

number of CMEs with a width larger than $100°$. The CDAW and CACTus datasets present a different amplitude of the range spanned by the mean angular width, *i.e.* for the CACTus catalog the mean width varies from $\approx 30°$ during solar activity minimum to $\approx 40°$ during the maximum of activity, while for CDAW the mean width varies from $\approx 20°$ to $\approx 80°$.

We used the same sample of years to study the variation in time of the distribution of the polar angle (PA) along which the CME propagated (Figure 5.6). For both datasets we can see two peaks centered around the PA corresponding to low latitudes, *i.e.* where the Active Regions (ARs) form and where the CMEs start. We note that the distribution of PA changes in time from a broader distribution in 2000 (near the maximum of Solar Cycle 23) to a more peaked distribution in 2006 (near the minimum of the solar activity). We deduce that the latitude distribution of CMEs follows the latitude distribution of the closed magnetic field regions in the corona, which is consistent with the fact that the CMEs originate in closed field regions (Hundhausen, 1993).

Chapter 6

Correlation between flares and CMEs: a statistical approach

In this chapter we discuss the main results on the flares and CMEs relationship concerning some physical parameters investigated over the solar cycles 23 and 24. We also report the results on a log-log correlation between the CMEs mass and the flux, emitted by the corresponding flares in the 0.1 – 0.8 nm range.

6.1 Previous results reported in literature

The relationship between flare properties and physical parameters of CMEs has been investigated by many authors. In the following we will provide a brief overview of these studies.

Using the data acquired by the Solar Maximum Mission (SMM) and considering a dataset ranging from 1984 to 1986, St. Cyr and Webb (1991), (see Table 6.1) pointed out that 76 % of the observed CMEs were associated with eruptive prominences, 26 % with flares observed in Hα, and 74 % with X-ray flares (Phillips, 1990).

Gilbert *et al.* (2000), using data acquired by LASCO (Brueckner *et al.*, 1995) and ground based observation from the Mark III K Coronameter (MK3) located in the Mauna Loa Solar Observatory (MLSO: MacQueen and Fisher, 1983; St. Cyr *et al.*, 1999), examined 18 CMEs and 54 Hα flares in a time window extending from 1996 to 1998, and discovered a clear association between Hα flares and CMEs (94 %), while 76 % of CMEs present an association with eruptive prominences. Subramanian and Dere (2001), in the same period using data acquired by LASCO and EIT instruments (Delaboudinière *et al.*, 1995) showed that the majority (44 %) of eruptive prominences associated with CMEs are inside the AR, while 15 % are outside the AR.

Using the LASCO and the Extreme Imaging Telescope (EIT) data taken by the SOHO spacecraft, Zhang *et al.* (2001a) analyzed four events and found that the impulsive acceleration phase of the selected CMEs coincided well with the rise phase of the associated X-ray flares. Later, Qiu and Yurchyshyn (2005) studied 11 events with varying magnetic field configurations in the source regions and concluded that the CMEs velocities were proportional to the total magnetic reconnection flux, while their kinetic energy was probably independent of the magnetic configuration of the source regions.

Moreover, Zhang *et al.* (2001a) found that the impulsive acceleration phase of the CMEs coincide with the rise phase of the associated flare in the X-ray range. Qiu

TABLE 6.1: Previous results on the correlation between CMEs, flares and eruptive prominences.

Authors	Number of CMEs	Period	CMEs associated with eruptive prominences	CMEs associated with Hα flares
St. Cyr and Webb (1991)	73	1984 – 1986	76 %	26 %
Gilbert *et al.* (2000)	18	1996 – 1998	76 %	94 %
Subramanian and Dere (2001)	32	1996 – 1998	59 %	
Zhou, Wang, and Cao (2003)	197	1997 – 2001	94 %	88 %

and Yurchyshyn (2005) found a direct relationship between the CMEs velocities and the total magnetic flux involved in the reconnection.

Zhou, Wang, and Cao (2003) selected 197 frontside halo CMEs from LASCO database, covering a period ranging from 1997 to 2001. They made a distinction between two categories of events: CMEs associated with flares (88 %) and the ones associated with eruptive filaments (94 %). They found that 59 % of the CMEs associated with flares occur before the flare onset observed by GOES, in agreement with Howard (1974) and Ludwig and Johnson (1981)), while the other events occur after the flares.

Chen, Chen, and Fang (2011) reexamined the velocity distributions considering whether and which elements may affect the velocities of the CMEs associated with flare and filament eruptions. They classified the CMEs occurring in the time window 2001 – 2003 into three types. The first one concerned the CMEs associated with flares. The second group contained the filament eruptions associated with CMEs. The third one considered the intermediate type. The main result of this analysis is that the velocities were strongly correlated with the mean magnetic field observed in the filament channel for the second group of events.

More recent studies on the flare - CME relationship were carried out by Gopalswamy *et al.* (2015a) Gopalswamy *et al.* (2015b), and Youssef (2012), but the results obtained were not able to completely clarify this issue.

Finally we recall the analysis on the X-ray flares and CMEs correlation using GOES and LASCO datasets extending from 1996 to 2006 carried out by Aarnio *et al.* (2011). They considered 13682 CMEs and 826 flares associated with CMEs. They found that an increase of the CME mass is related to an increase of the flux of the flares, following an approximately log–log relationship: $log(CME\ mass) = 0.70 \times log(flare\ flux)$. Aarnio *et al.* (2011) have also pointed out higher linear velocities (495 ± 8 km s^{-1}) of the CMEs associated with flares in comparison with those that were not associated with flares (422 ± 3 km s^{-1}).

On the other hand the CMEs width is strongly correlated with the flux of the flares. The CMEs associated with flares of X GOES class are usually the widest ones ($80^\circ \pm 10^\circ$), while the CMEs associated with flares of B GOES class are the narrowest ($42^\circ \pm 1.4^\circ$) (Aarnio *et al.*, 2011).

6.2 GOES dataset

In order to investigate on the flares and CME correlation we used the same datasets considered in Chapter. 5, and collected 19811 C, M, and X-class flares using the dataset acquired by GOES, extending from July, 31,1996 to March, 31, 2014. We found 17712 flares of C class (89.40 %), 1884 flares of M class (9.51 %), and 155 flares of X class (0.78 %). We also took into account the flare location on the solar disk when this information was reported by the National Geophysical Data Center (NGDC; ftp://ftp.ngdc.noaa.gov/).

6.3 Correlation between flares and CMEs

In order to determine the possible association between one CME and one flare, we used a temporal criterion, requiring that both flare and CME occur within a set time window. We initially set time windows to select CME first observation time that occurs within ± two hours of the flare start time, peak time, or end time, using both datasets.

When we consider the CDAW dataset and the flare start time, we find that the highest number of CMEs and flares (59.57 %) is characterized by a difference in time between 10 and 80 minutes (see the black line in the top panel of Figure 6.1), confirming the results obtained by Aarnio *et al.* (2011).

The distribution of the CME-flare associated events for the CACTus dataset (bottom panel of Figure 6.1) is slightly different from the CDAW dataset. In fact, we observe a wider time range (from -30 to 110 minutes) for the occurrence of most of the associated events.

We argue that this difference between the two datasets depends on the different criteria used by the observer for defining a CME in CDAW. A time window of 10–80 minutes is clear evidence that in many cases the flare occurs before the first observation of the CME in the coronagraph and, taking into account that the temporal resolution of LASCO is about 30 minutes, there are a number of cases in which the flare most likely precedes the CME initiation and may be the first manifestation of the initiation process.

Considering the flare start time and a time interval of ± two hours, we found 11441 and 9120 flares associated with CMEs using the CDAW and the CACTus catalogs, respectively. The distributions of these flares according to the GOES class are reported in Table 6.2. In both cases the temporal shift between the flare and the CME decreases if we consider the distributions obtained using the flare-peak time and the flare-end time (see Figure 6.1). In Table 6.2, 6.3, and 6.4 we present the associated CMEs-flares using only temporal criteria. In this way we obtained in first approximation a high number of CMEs associated with flares, which drastically decreases when we apply a spatial correlation between these events to select the true-associated events as described in the following Section 6.4. So that finally we found only 1277 CMEs associated with flares that are spatially and temporally correlated.

The same analysis was performed using the time intervals ± one hour, ±30 minutes, and the flare start time. The results are reported in Tables 2.1 and 2.2. A similar behavior of the correlation between CMEs and flares in different time intervals and in different GOES classes has been found for both datasets. We ascribe the smaller number of CACTus CMEs associated with X-class flares to the limits of the CACTus algorithm in the detection of the fastest CMEs (Yashiro, Michalek, and Gopalswamy, 2008).

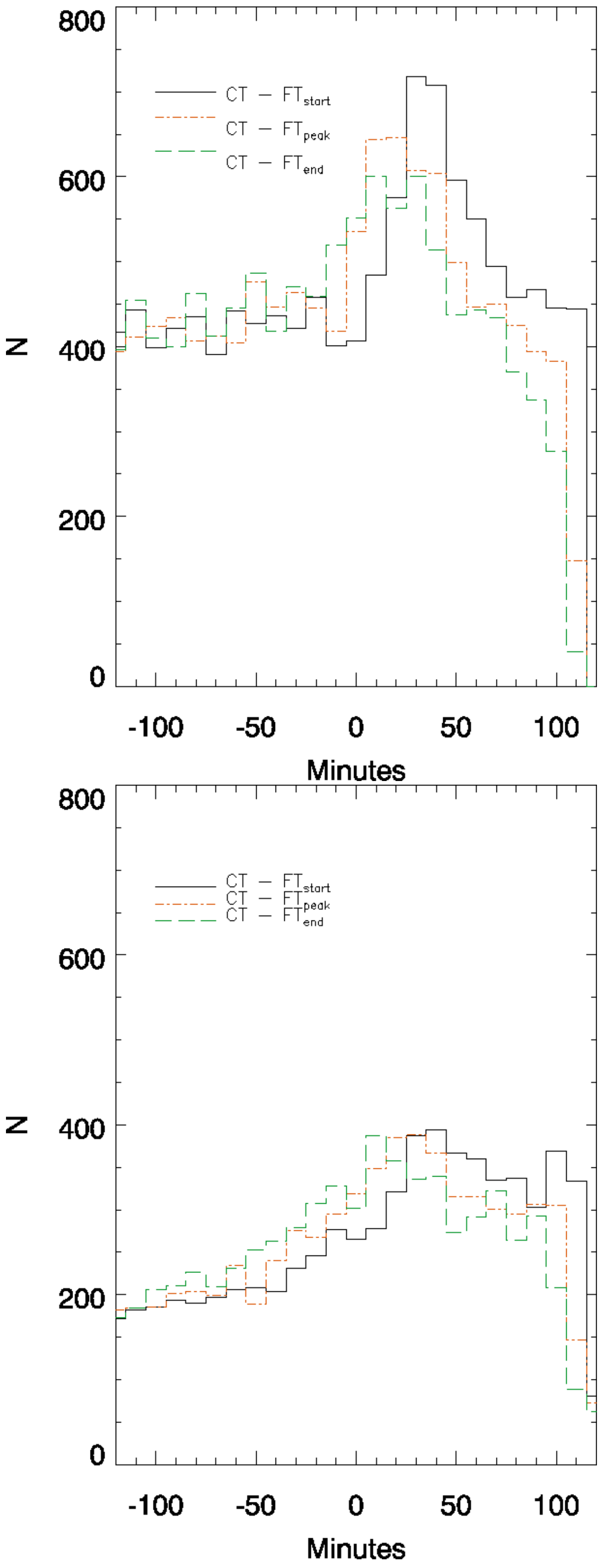

FIGURE 6.1: Distribution of the CME associated with flares considering the difference in time between the CME first observation and the flare start (black line), peak (dot–dashed-red line), and end time (long-dashed-green line). CT and FT refer to CME first observation time and flare time, respectively. The top and bottom panels refer to the CDAW and CACTus datasets, respectively.

TABLE 6.2: Correlation between CMEs and flares for CDAW and CACTus datasets in the ± two hours time interval.

Flares		CDAW		CACTus	
GOES class	Number of events	flare associated with CME ± 2 h [%]	CMEs not associated with flares [%]	flare associated with CME ± 2 h [%]	CMEs not associated with flare [%]
C	17,712	10003 (56.47 %)	11074 (48.40 %)	7755 (43.78 %)	6396 (41.22 %)
M	1884	1308 (69.43 %)		1242 (65.92 %)	
X	155	130 (89.39 %)		121 (78.06 %)	
Halo CMEs	616	315 (51.14 %)	301(48.86 %)		

TABLE 6.3: Correlation between CMEs and flares for CDAW and CACTus datasets in the ± one-hour time interval.

Flares		**CDAW**	**CACTus**
GOES class	Number of events	flare associated with CME ± 1 h [%]	flare associated with CME ± 1 h [%]
C	17,712	5842 (32.98 %)	4228 (23.87 %)
M	1884	951 (50.48 %)	771 (40.92 %)
X	155	118 (76.13 %)	86 (55.48 %)

The distributions of C-, M-, and X-class flares associated with CMEs, as a function of the year in the solar cycle in the time interval of ± two hours, ± one hour, ±30 minutes, are shown in Figures 6.2 and 6.3 for CDAW and CACTUs, respectively. We note that the probability of finding CMEs associated with flares decreases when the time window is narrower. However, we see that the peak and the shape of the distributions remain similar, independently of the considered time window.

In the top panel of Figures 6.2 and 6.3, the peaks correspond to the years 2000 – 2002 and 2011 – 2014, and are in agreement with the solar activity cycles (see Figure 5.1). We can see in the distribution of C-class flares associated with CMEs (top panels of Figures 6.2 and 6.3) that these events are present also during the phases of minimum of solar-activity. In the distribution of M-class flares (middle panels of Figures 6.2 and 6.3) we can see a trend very similar to the one found for C-class flares.

On the other hand, we note that the distribution of X-class flares associated with CMEs is more uniform across the solar cycle than that of C- and M-class flares for

TABLE 6.4: Correlation between CMEs and flares for CDAW and CACTus datasets in the ± 30 min. time interval.

Flares		**CDAW**	**CACTus**
GOES class	Number of events	flare associated with CME ± 30 min. [%]	flare associated with CME ± 30 min. [%]
C	17,712	2992 (16.89 %)	2159 (12.19 %)
M	1884	445 (23.62 %)	341 (18.099 %)
X	155	62 (40.00 %)	37 (23.87 %)

both datasets. For example, for CDAW in 1998 and 2005 we observe 14 and 18 X-class flares associated with CMEs respectively, while for CACTus we observe 6 and 8 X-class flares in those years, although the magnetic activity was not high. However, when we consider only the flares associated with CMEs in a ± 30 minute time window, we find a distribution of the X-class flares more consistent with the solar cycle for both distributions. We then can state that the shape of the distributions of C-, M-, and X-class flares associated with CMEs varies with the intensity of the flares.

In Figure 6.4 we show the distribution of CMEs velocity, distinguishing between events associated with flares in the ± two hours time window and events not associated with flares. The mean CMEs velocities in CDAW datasets for the CMEs associated and not associated with flares are 472.87 ± 2.77 km s^{-1} and 379.41 ± 2.25 km s^{-1}, respectively. The mean CMEs velocities in CACTus dataset for the CMEs associated and not associated with flares are 500.62 ± 3.28 km s^{-1} and 437.75 ± 3.79 km s^{-1} respectively. In Figure 6.4 (right panel) we note that there are a great number of CMEs not associated with flares in the CACTus dataset with velocities between $100-200$ km s^{-1}. In fact,the mean velocities for CMEs associated with flares are higher than the velocities for CMEs not associated with flares in both datasets. Therefore, our results are very similar to those found by Aarnio *et al.* (2011).

The distribution of the CME acceleration (left panel of Figure 6.5) shows that the CMEs associated with flares have an average acceleration of $-0.32\pm$ 0.34 m s^{-2} , while the CMEs not associated with flares have an average positive acceleration of 3.44 ± 0.39 m s^{-2} . We notice that these values are slightly different from those found by Aarnio *et al.* (2011) due to the diverse sample of events considered in our analysis.

In the right panel of Figure 6.5 we report the distribution of the CME mass. The logarithms of mean CME mass for CMEs associated with flares and not are 14.7 and 14.5, respectively.

Furthermore we found different linear velocity distributions when we distinguish among the three flare classes (Figure 6.6). The CDAW velocity distribution of the CMEs associated with the C-class flares shows a significant peak at 250 km s^{-1} that is not present in the CACTus velocity distribution. For CDAW the mean linear velocities of CMEs associated with flares of C-, M-, and X-classes are 535.9 ± 1.1 km s^{-1} , $585.7\pm$ 8.2 km s^{-1}, and $627.0\pm$ 56.6 km s^{-1}, respectively. For CACTus the mean velocities of CMEs associated with flares of C-, M-, and X-classes are $487.9\pm$ 3.5 km s^{-1}, $562.2\pm$ 9.8 km s^{-1}, and $688.1\pm$ 34.3 km s^{-1} , respectively.

Both distributions are similar except that CACTus finds fewer events than CDAW, as we note in the distribution of CMEs associated with C-class flares (see the blue line in Figure 6.6). It is worth noting the difference between the velocity of CMEs associated with X-class flares in the CDAW dataset and in the CACTus dataset. In fact most of the CMEs associated with flares in the CACTus dataset are faster than the ones of the CDAW dataset (see-*e.g.* - Gosling *et al.*, 1976; Moon *et al.*, 2003).

In Figure 6.7 we show the relationship between CME speed and acceleration in the whole period covered by our dataset and not year by year as in Figures 5.2 and 5.4, taking into account the different class of the associated flares. We found that the majority of CMEs characterized by higher velocities are associated with acceleration between -200 and 200 m s^{-2} . On the other hand, there are many CMEs with a much larger acceleration (between -400 and 400 m s^{-2}), but with velocity below 700 km s^{-1}. These CMEs are mainly associated with C- and M-class flares. We note in Figure 6.7 that there is not a clear correlation between acceleration and

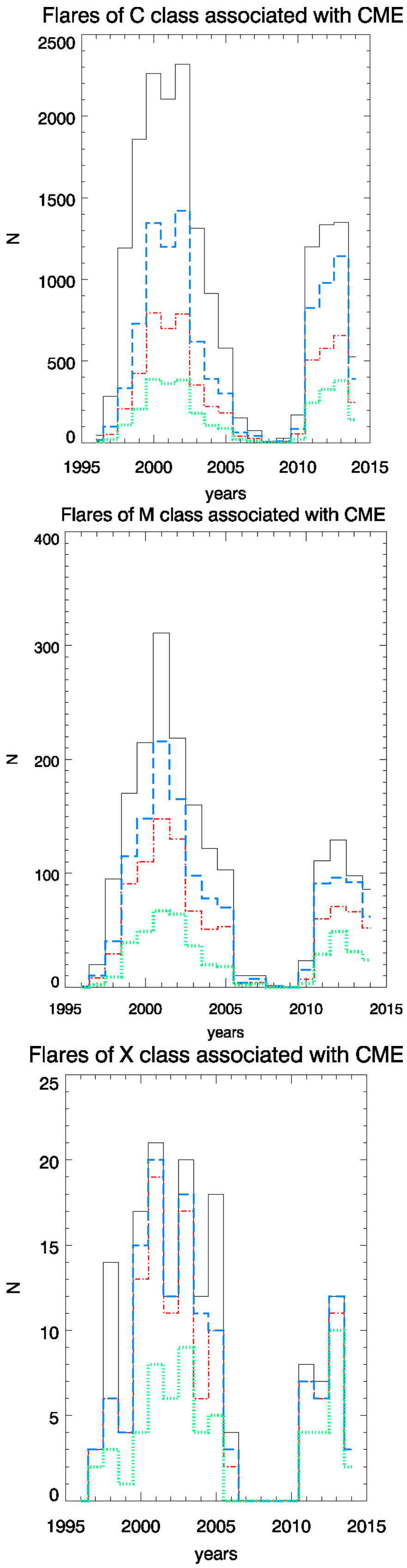

FIGURE 6.2: In the top, middle, and bottom panels we report the distribution of C-,M, and X, class flares associated with CMEs vs years for CDAW dataset, respectively. The long–dashed-blue line, dot–dashed-red line and the dotted-green line represent the CMEs associated with flares in ± two hours time interval, ± 1 hour time interval and ± 30 minutes time interval, respectively. The total flares distribution for a given class is indicated in black in each panel.

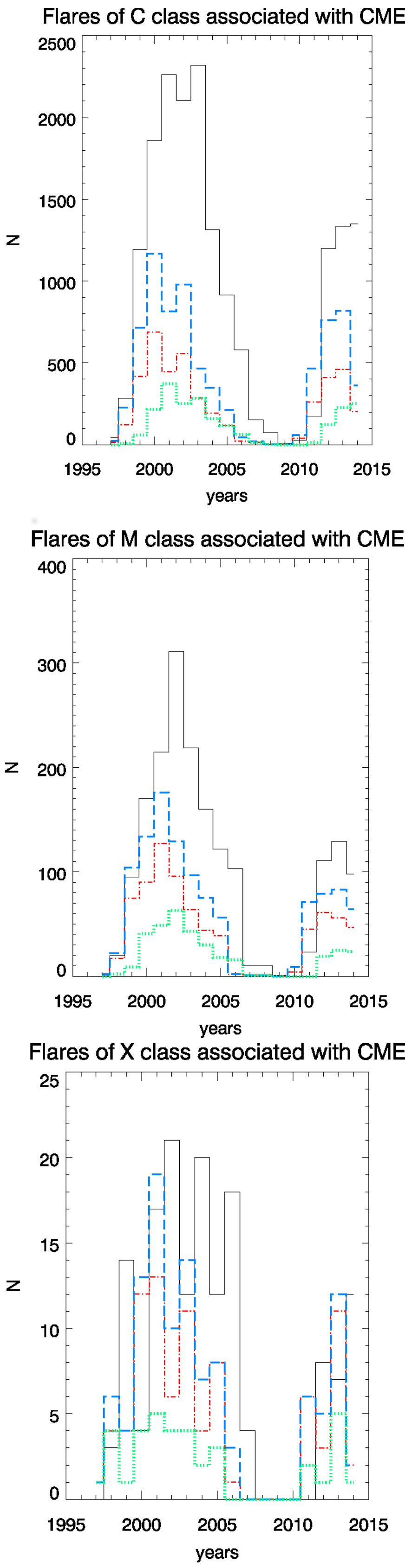

FIGURE 6.3: In the top, middle, and bottom panels we report the distribution of C-,M, and X, class flares associated with CMEs vs years for CACTus dataset,respectively. The long–dashed-blue line, dot–dashed-red line and the dotted-green line represent the CMEs associated with flares in ± two hours time interval, ± 1 hour time interval and ± 30 minutes time interval, respectively. The total flares distribution for a given class is indicated in black in each panel.

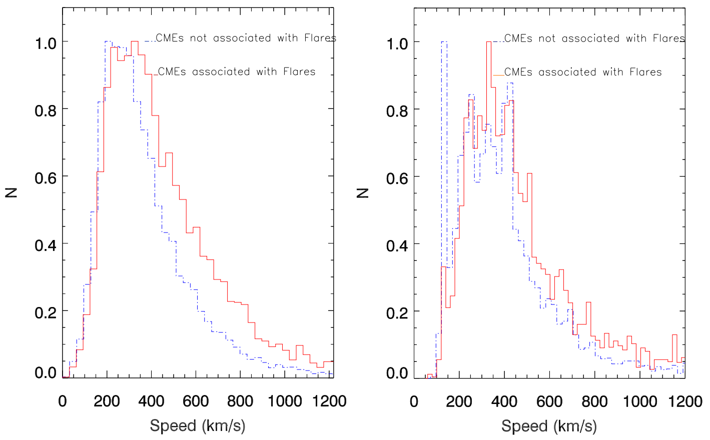

FIGURE 6.4: The left and right panels represent the CMEs velocities for CDAW and CACTus datasets, respectively. The CMEs associated with flares are indicated by solid -red line,while the CMEs not associated with flares are indicated by the dot–dashed blue line.

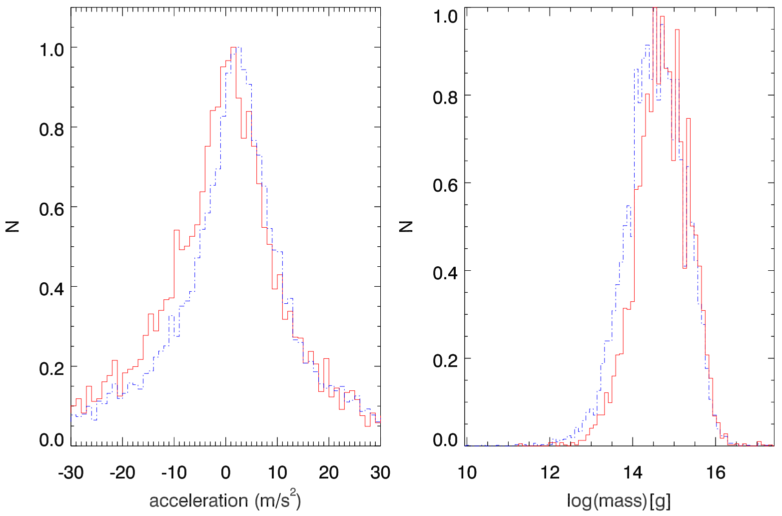

FIGURE 6.5: The left and right panels represent the CMEs acceleration and mass for CDAW dataset, respectively. The CMEs associated with flares are indicated by solid-red line,while the CMEs not associated with flares are indicated by the dot–dashed blue line.

speed of CMEs associated with flares: this is probably due to the fact that the bulk acceleration of CMEs occurs below the coronagraph occulter.

We finally remark that the CMEs width is strongly correlated with the flux of the flares. The mean angular width of the CMEs associated with flares of C, M, and X, classes are $68.61°$, $116.82°$, $258.49°$, respectively.

6.4 CME Parameters and Flare Energy

We used our dataset to investigate the relationship between the logarithm of the flare flux [ϕ_f] and the logarithm of the CME mass [m_{CME}]. In this case we considered not only the temporal correlation between flares and CMEs, but also their spatial correlation. We limited this analysis to flares which occurred in the time window of ± two hours and characterized by a known location of the source region on the solar disc. We associated flares which occurred in the top-right quadrant of the solar disk with CMEs characterized by a polar angle between 0° and 89°, flares occurred in the top-left quadrant with CMEs characterized by a polar angle between 90° and 179°, *etc.* This criterion of association between flares and CMEs is based on the assumption that most CMEs propagate nearly radially, according to the standard CME–flare model (see Lin and Forbes, 2000). In this way we obtained 1277 CMEs that are spatially and temporally correlated with flares.

We considered the flux of these flares integrated from their start to end in the $0.1-0.8$ nm range. Subsequently the 1277 CME–flare pairs were binned into 13 equal sets of 100 pairs each, with the exception of the last one containing 77 pairs. We computed the mean value of the logarithm of the CME mass and the logarithm of flare flux in each group. The relationship between the logarithm of the CME mass and the logarithm of the flare -flux is shown in Figure 6.8, where we also show the error bars of the logarithm of the CMEs mass computed as $\sigma/\sqrt{N}$. The flux error bars correspond to the minimum/maximum flare flux values spanned by that bin.

The results shown in Figure 6.8 are similar to the result reported by Aarnio *et al.* (2011). In fact we found the following log–log relationship between integrated flare flux [ϕ_f] and CME mass [m_{CME}]:

$$\log(m_{CME}) = (12.33 \pm 0.10) + (0.23 \pm 0.04)\ \log(\phi_f). \tag{6.1}$$

However, it is worth noting that this relationship disappears when we limit the same analysis on the sample of flare associated with CMES to each year of our dataset, corresponding to the different phases of the solar cycle. This means that the log–log relationship between integrated flare flux and CME mass is only consistent for a large sample of events, but it is not valid during the different phases of the solar cycle.

The unreduced χ^2-test of the linear fit that we have performed is 0.07. Further tests to verify the goodness of the fit have also been performed. The Spearman's coefficient , indicating how well the relationship between two variables can be described using a monotonic function, is 0.82, which indicates a good correlation between these quantities. We also found a p-value of 0.85 and a linear Pearson correlation coefficient of 0.87.

If we consider the result on the correlation between the mass of the CME and the energy flux of the associated flare in the general scenario of the CME models described in Chapter 4, we could argue that the most plausible models are those based on the key role played by a filament that undergoes an eruption, like for instance the mass loading model, the tether release and tether cutting model, the flux rope model and the breakout model. In fact, all these models have in common the presence of a filament / flux rope that, due to some instability, starts to rise and later erupts. We also know that the most energetic flares occur in the most complex magnetic field configurations. Therefore, one preliminary conclusion, that however needs to be further explored, is that the relationship between the mass of the expelled cloud of plasma and the energy of the associated flare indicates situations characterized by flux ropes embedded in highly complicated magnetic field configurations.

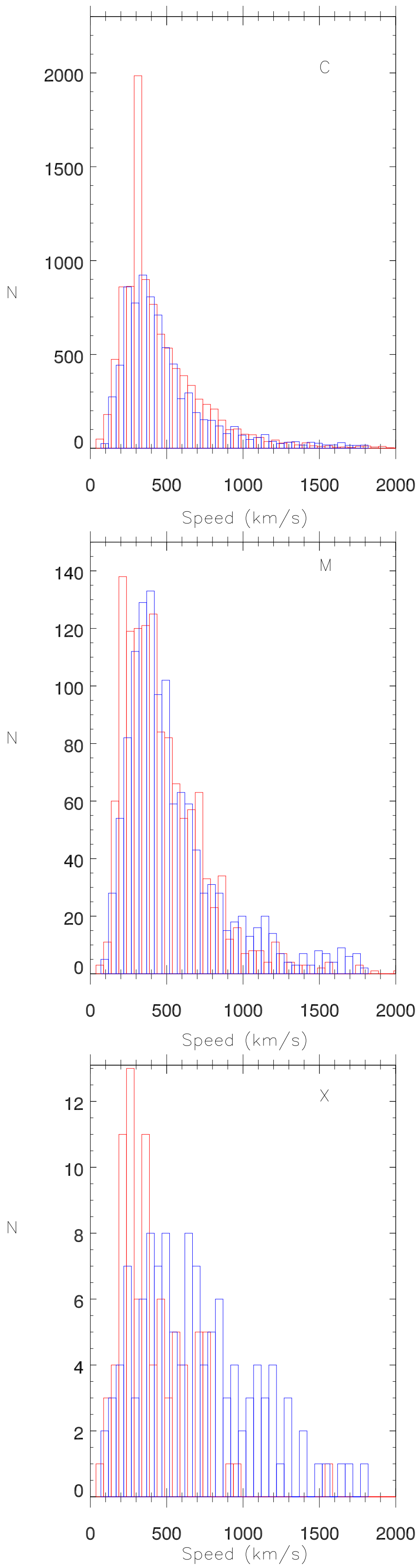

FIGURE 6.6: The top, middle and bottom panels show the velocity for CMEs associated with C, M, and X class flares, respectively for CDAW (red line) and CACTus (blue line)

.

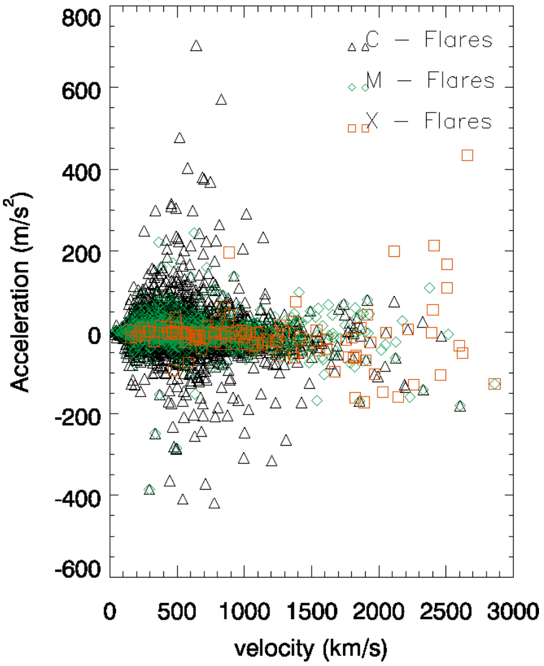

FIGURE 6.7: The black triangle, green diamond, and red square, indicate CME velocity vs acceleration for the C, M, and X associated flares, respectively.

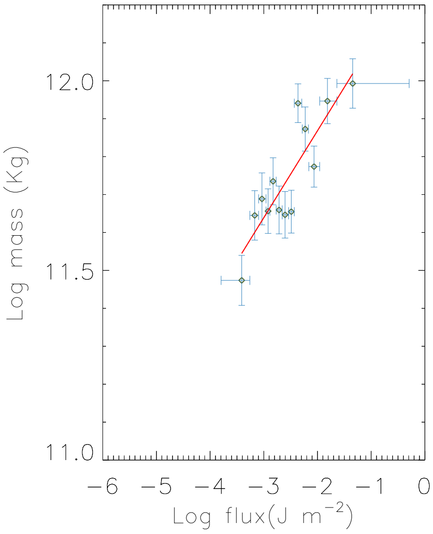

FIGURE 6.8: Relationship between integrated flare flux and CME mass for the CMEs associated with flares in the ± two hour time window.

Chapter 7

Possible correlation between CME occurrence and variations of the night-sky brightness

This Chapter describes a novel study on the possible correlation between the effects of CMEs on the Earth atmosphere and the variations of the night-sky brightness, using data acquired by the fluorescence detectors of the Pierre Auger Observatory (PAO).

Previous studies, described in (Gulyaev, 1996) investigated the possibility to detect signatures of CMEs in the night-sky from ground-based optical observations. Using the zodiacal light photometers on-board the Helios space probes, they concluded that a faint luminous extended object observed in the night sky at the distance of 50° from the Sun was a possible signature of a CME.

The Pierre Auger Observatory was born for a huge statistics study of cosmic rays at the highest energies. The main scientific goals are to measure the properties of the Extensive Air Showers (EAS) to determine the energy and arrival direction of each cosmic ray and to provide a statistical determination of the distribution of primary masses (cosmic ray composition). The Pierre Auger Observatory located in Malargüe (Province of Mendoza), Argentina, has been taking data since 2004, adding detectors as they became active until completion in 2008. The Observatory is an hybrid detector, a combination of a large Surface Detector (SD) and a Fluorescence Detector (FD). The SD is composed of a baseline array, consisting of 1660 water Cherenkov stations placed in a triangular grid separated by 1500 m and a smaller array inside (stations separated by 750 m). The Surface Detector is spread over an area of ~ 3000 km^2. The FD operates in combination with the SD. Its primary purpose is to measure the longitudinal profile of showers recorded by the SD whenever the sky is dark and clear enough to make reliable measurements of fluorescence produced by the Extensive Air Showers in their development in the atmosphere. In the next section a brief overview of the Fluorescence Detector will be presented (Aab *et al.*, 2015).

7.1 The Fluorescence Detector

The FD is composed of 24 fluorescence telescopes that overlook the SD array from four sites: (named Eyes) Los Leones, Los Morados, Loma Amarilla and Coihueco (Abraham *et al.*, 2010)

Six independent telescopes are located at each FD site in a clean climate controlled building (see Figure 7.1).

FIGURE 7.1: FD building at Los Leones; behind the building is a communication tower.

A single telescope has a field of view of 30 × 30 degrees in azimuth and elevation with a minimum elevation of 1.5 degrees above the horizon. The combination of the six telescopes provides 180 degrees coverage in azimuth. The photomultipliers of the telescope are arranged in a matrix of 22 rows and 20 columns (Figure 7.2). Each photomultiplier looks at a small fraction of the sky that represents a pixel, with $1.5°$ field of view. The XP3062 photomultiplier tube is an 8-stage unit with a bialkaline photocathode with quantum efficiency (Figure 7.3) of about 25% in the (350-400) nm wavelength range. The filter transmission is above 50% in the (310-390) nm UV range and 80% in the (330-380) nm. The filter reduces the background light flux and thus improves the Signal-to-Noise (S/N) ratio of the measured air shower signal. Abraham *et al.* (2010)

The detection of ultra-high energy cosmic rays (particles and nuclei with energy $\geq 10^{18} eV$) using nitrogen fluorescence emission induced by Extensive Air Showers is a well established technique, used previously by the Fly's Eye (Baltrusaitus *et al.*, 1985) and HiRes (Abu-Zayyad *et al.*, 2000) experiments. Charged particles generated during the development of Extensive Air Showers excite atmospheric nitrogen molecules and these molecules then emit fluorescence light in the 300-430 nm range. On the fluorescence telescope, cosmic ray showers are detected as a sequence of triggered pixels. An example of an event propagating through two adjacent FD telescopes is presented in Figure 7.4.

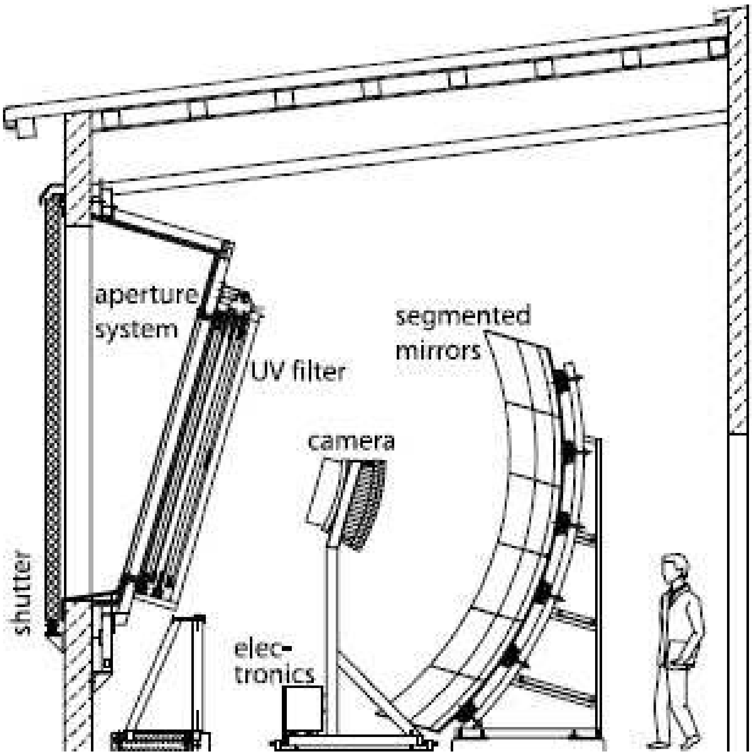

FIGURE 7.2: Schematic view of a fluorescence telescope with a description of its main components.

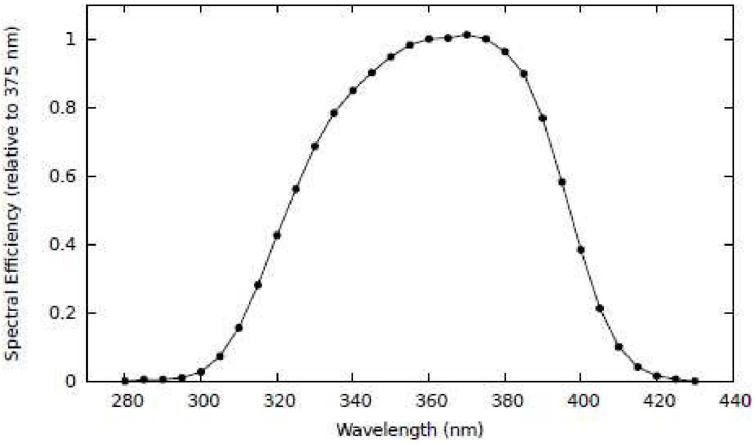

FIGURE 7.3: The relative efficiency between 280 nm and 430 nm wavelength measured for the telescope 3 at Coihueco. The curve is taken relative to the efficiency of the telescope at 375 nm.

The presence of the moon above the horizon increases the background light level, which has to be monitored. The direct current induced by the background signal is eliminated by the AC coupling of the phototube base, nevertheless it is possible to determine background levels using the direct relation between the fluctuations of the sky background and the photon flux. The analysis of the fluctuations in the ADC signal (variance analysis) performed for each night of data taking is used to monitor the FD background signal and data taking conditions. Thus the amount of light is derived from ADC variance value and it is given in units of *ADC counts* (Kleifges *et*

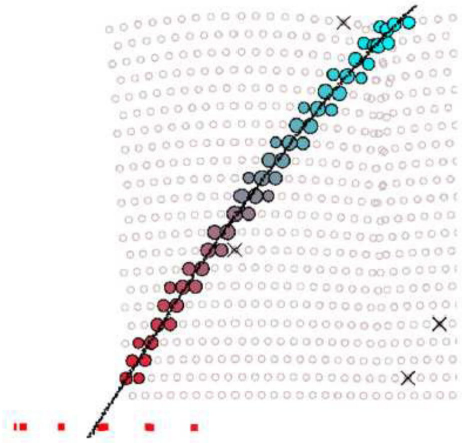

FIGURE 7.4: Light track of a stereo event as seen by the fluorescence telescopes. The different colors indicate the timing sequence of the triggered pixels. The full line is the fitted shower-detector plane.

al., 2003). The total background signal is the sum of the electronics background (photomultiplier and electronics noise) and the sky brightness (airglow, moonlight, stars and planet light, zodiacal light, [1] twilight and artificial light). The typical values of background signals are: 3-5 *ADC counts* for electronics background, around 20 *ADC counts* for cloudy nights and within 25 and 60 *ADC counts* for clear moonless nights Caruso *et al.* (2005a). During the nights when the moon is above the horizon, the light background level can reach several hundred *ADC counts*. The optimal background conditions for the measurements range from 25 to 60 *ADC counts* which corresponds to photon background flux from approximately 100 to 250 $photons\ m^{-2}\ deg^{-2}\ \mu s^{-1}$ (Abraham *et al.*, 2010).

7.2 The Night Sky Brightness

The diffuse Night Sky Brightness (NSB) is defined as the luminosity of the sky when the solar elevation angle (the position of the Sun with respect of the horizon) of the Sun is well beyond the horizon[2] in clear and moonless nights, excluding the brightest stars. The ground-based detectors present a small field of view to observe an area of the sky far away from stars; they are active only in total absence of the Moon. Moreover many space-borne experiments on balloons and satellites collect data to estimate the night sky photon flux from the Earth's surface and atmosphere seen from high altitude or near space.

As a matter of fact, the monitoring of this light in the UV wavelength range is fundamental in experiments based on the fluorescence detection technique as it represents a background signal to be subtracted in the reconstruction of the Ultra High Energy Cosmic Rays (UHECR).

---

[1] faint, diffuse, white glow visible in the night sky that appears to extend from the vicinity of the Sun along the ecliptic

[2] usually below -18°, definition of the astronomical twilight, where the scattered light is negligible

The sources of the night sky radiation, which presents a spectrum from the far Infra-Red (IR) to the Ultra-Violet (UV) electromagnetic spectrum, are the faint stars of the Milky Way and the galaxies too far to be seen or resolved; moreover the diffusion of the light from this sources on the galactic dusts has to be considered together with the solar radiation diffused inside the Solar System. In addition, the atmosphere has to be taken into account as a source of diffusion and the so-called *airglow*. Moreover it can not be ignored the effect of the artificial lights, which can pollute entire regions through diffusion and reflection in the atmosphere and in presence of clouds.

The contributions to the diffuse night sky background between 100 nm (far UV) and 200 μm (far IR) in a clear moonless night are (Leinert *et al.*, 1998):

- **airglow** (I_A), produced in the atmosphere;
- **zodiacal light** (I_{ZL}), due to the interplanetary dust, is composed both by diffused solar radiation and thermal emission;
- **integrated starlight** (I_{ISL}) of faint stars;
- **diffuse galactic light** (I_{DGL}) due to interstellar gas inside the Milky Way;
- **extragalactic background light** (I_{EBL}) produced by far galaxies that can not be observed or resolved.

In the Earth's atmosphere the radiation of the above mentioned components is attenuated according to an exponential extinction coefficient $e^{-\tau}$. Moreover, diffusion processes add the contribution of the tropospheric scattering (I_{sca}) which is never attenuated.
Eventually the intensity of the diffuse night sky brightness can be written as:

$$I_{NightSky} = (I_A + I_{ZL} + I_{ISL} + I_{DGL} + I_{EBL}) \cdot e^{-\tau} + I_{sca} \tag{7.1}$$

There are two important components that are missing as they are usually negligible in astronomical experiments: the moonlight (direct and diffused) and the artificial light.

7.2.1 Dependence of NSB on the solar cycle

Recently an analysis of the diffuse night sky brightness measured at the **ESO-Paranal Observatory** has been carried out, searching for an effect of the solar cycle on the background luminosity (see Patat (2003, 2008)).

The ESO-Paranal Observatory is located in the north of Chile, in the Atacama desert, on the Cerro Paranal mountain (about 2635 m a.s.l.) where the climatic conditions (weather stability, negligible light pollution, etc.) allow to reach a great accuracy in NSB measurements.

The study of interest used data collected in the period 2000-2007, a period of transition from a maximum of the solar activity (2000/01) to a minimum (2007/08), in order to have a precise indication of the dependence of the diffuse NSB on the solar cycle.

A first result was to point out the presence of a not negligible *yearly half-oscillation* of the diffuse NSB (up to $\approx 0.5\ mag\ arcsec^{-2}$) in the V, R and I bands (Figure 7.5), that was demonstrated to be independent from zodiacal light and solar activity. The most important conclusion is related to the solar cycle: thanks to the time interval

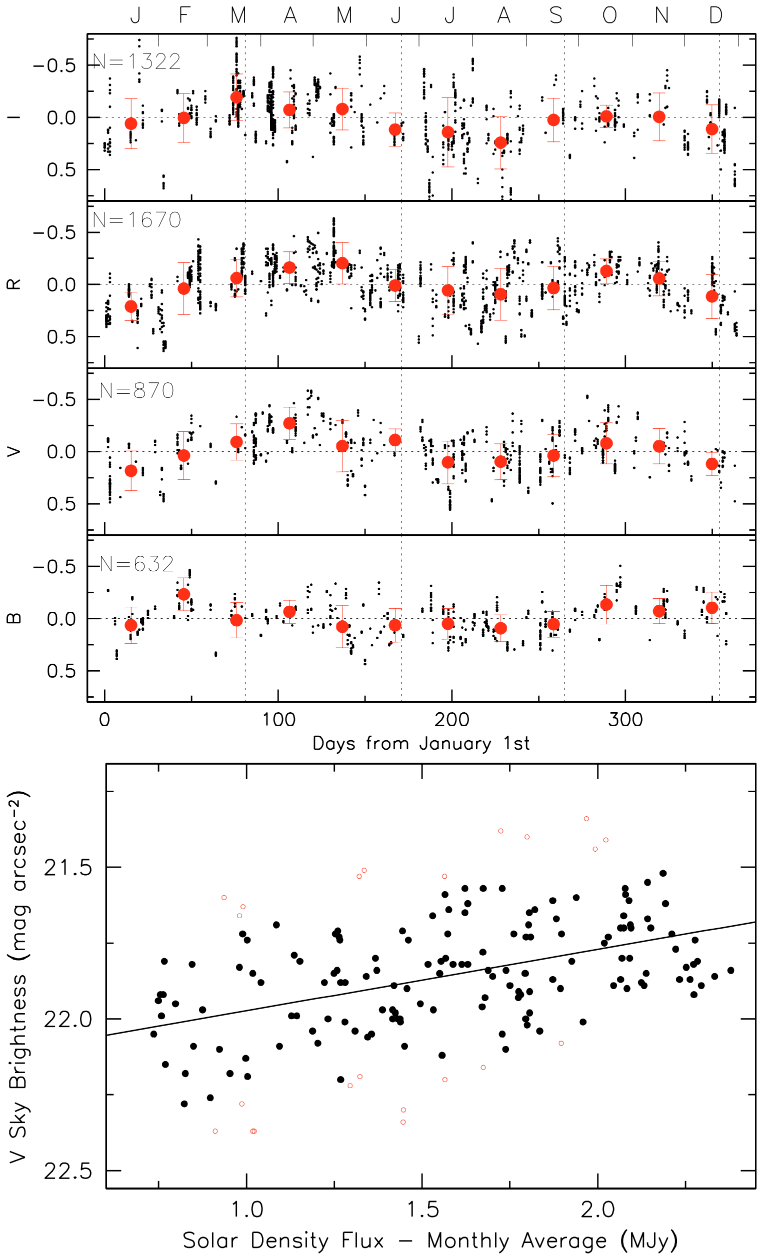

FIGURE 7.5: Results from data of the ESO-Paranal Observatory. (*Top*) Seasonal variation of the diffuse NSB with respect of the average value for the I, R, V; and B bands. Black points, the single measurements; red dots, monthly averages; vertical lines, equinoxes and solstices. The contribution of the zodiacal light and of the solar activities are already subtracted. Image from Patat (2008). (*Bottom*) Correlation between the temporal averages of the monthly averaged Penticton-Ottawa solar flux at 2800 MHz (Covington, 1969) in the radio range and of the NSB in the V-band; the line is the linear fit that proves the correlation itself. Image from Patat (2008).

available, they found a correlation between the diffuse night sky brightness and the *solar flux density*[3], once the zodiacal light is subtracted (Figure 7.5).

In particular it was established a correlation between the diffuse night sky brightness and the solar flux density averaged on the 30 days before the NSB measurement, which means that the solar activity has an effect on the Earth's atmosphere (and then on the NSB) with a delay of about one month.

7.2.2 The results of ground-based NSB measurements

It is reasonable to assert (Sanchez, 2007) that the diffuse night sky brightness in the U band is about $22\ mag\ arcsec^{-2}$, taking for granted in all the astronomical observatories in the conditions of : (1) clear moonless night; (2) measurements at the zenith; (3) field of view of observation where the zodiacal light is faint; (4) artificial light pollution negligible.

At this point it is necessary to convert this value, expressed in units common in the astronomical field, to units of the International System: from a brightness expressed as a magnitude distributed in a region of sky of one square arcsecond ($mag\ arcsec^{-2}$) to a flux of photons per unit of area, solid angle and time (*photons* $m^{-2}\ sr^{-1}\ ns^{-1}$).

For the U-band, in particular around $350\ nm$, the flux is:

$$F_\gamma \simeq 500\ photons\ m^{-2}\ sr^{-1}\ ns^{-1} \tag{7.2}$$

This equation indicates the reference value for the photon flux measured from ground and it will be used to compare the results obtained from the PAO, in Figures 7.9 and following.

7.3 The measurement of the night sky background in the Pierre Auger Observatory

The proper measurement of the photon flux due to the night sky brightness is not simple to accomplish with the data from the Pierre Auger Observatory as the background luminosity is monitored only to be subtracted from the fluorescence signals from EAS. Furthermore, it is important to take into account the differences with the observations performed by astronomical experiments.

The fluorescence observations are performed also in presence of the Moon (even when the diffuse moonlight becomes the dominant component of the night sky brightness) and in cloudy conditions while the astronomical results are obtained only in clean and moonless nights. Moreover astronomical instruments present a very small field of view and usually point areas of the sky near to the zenith while the PAO telescopes observe a huge portion of the sky from $\approx 2^\circ$ to $\approx 30^\circ$ in elevation and 30° in azimuth.

The differences in the NSB measurements are caused also by the acquisition process of the photomultipliers of the PAO: as the coupling of a phototube with the

---

[3] Flux of solar energy, measured in $[W\ m^{-2}\ Hz^{-1}]$.

electronics is made in alternate current, the instrument can measure only variations of a signal, in this case the sky luminosity; therefore the "physical observable" is no more the night sky brightness, but its variance (σ^2_{sky}).

The quantity actually measured by each photomultiplier is the variance of the background signal (σ^2_{ADC}), expressed in $(ADC\ counts)^2$; this value is given by the sum of the variance of the night sky brightness (σ^2_{sky}) and the variance of the electronic noise [4] (σ^2_{elec}):

$$\sigma^2_{ADC} = \sigma^2_{sky} + \sigma^2_{elec}$$

The measurement of σ^2_{ADC} is performed together with the usual data taking of the fluorescence telescopes: each 30 seconds is recorded a background event, from the beginning of the nightly data taking to the closing of the shutters of each telescope.

In order to obtain σ^2_{elec} about 50 events of electronic noise are recorded every 5 second, before and after the nightly data taking; then it must be subtracted to the total variance to extract the σ^2_{ADC}.

The determination of the NSB photon flux requires a perfect knowledge of the acquisition chain, in the sky from outside the diaphragm of each telescope to the digitalised signal in $(ADC\ counts)^2$ (Figure 7.6): the reconstruction is made pointing out what the signal is at each step and studying the processes in the inverse direction with respect to the propagation of the signal itself. This approach was initially presented in Caruso and Petrera (2003) and then developed in Caruso and Petrera (2004, 2006).

It is important to stress that all the quantities of interest are integrated over a $100\ ns$ time interval, typical for both the photomultiplier and electronics used in the PAO fluorescence telescopes.

The flux of photons from the night sky brightness as a function of the measured variance of the background signal from the PMTs of the PAO is obtained as:

$$\Phi^{NSB}_{\gamma} = \frac{10 \cdot Q \cdot f \cdot C^2_{FD}}{\mathcal{A}_{pix} \cdot \Delta t \cdot (1 + V_G) \cdot 2B}\, \sigma^2_{sky} \tag{7.3}$$

In tab. 7.1 the values of the used factors and the related uncertainties are reported.

7.3.1 Result on the night sky photon flux from the Pierre Auger Observatory

A first analysis performed by the Pierre Auger Collaboration concerned only the first months of data taking (before 2006). The measurements can be divided into classes according to the different environmental conditions:

- clean moonless nights;
- nights with the sunrise/sunset or moonrise/moonset, characterised by an increasing or decreasing luminosity due to light diffusion;

---

[4] The electronic noise is caused by the so-called dark current of the phototube and by stochastic processes among the various components of the electronics.

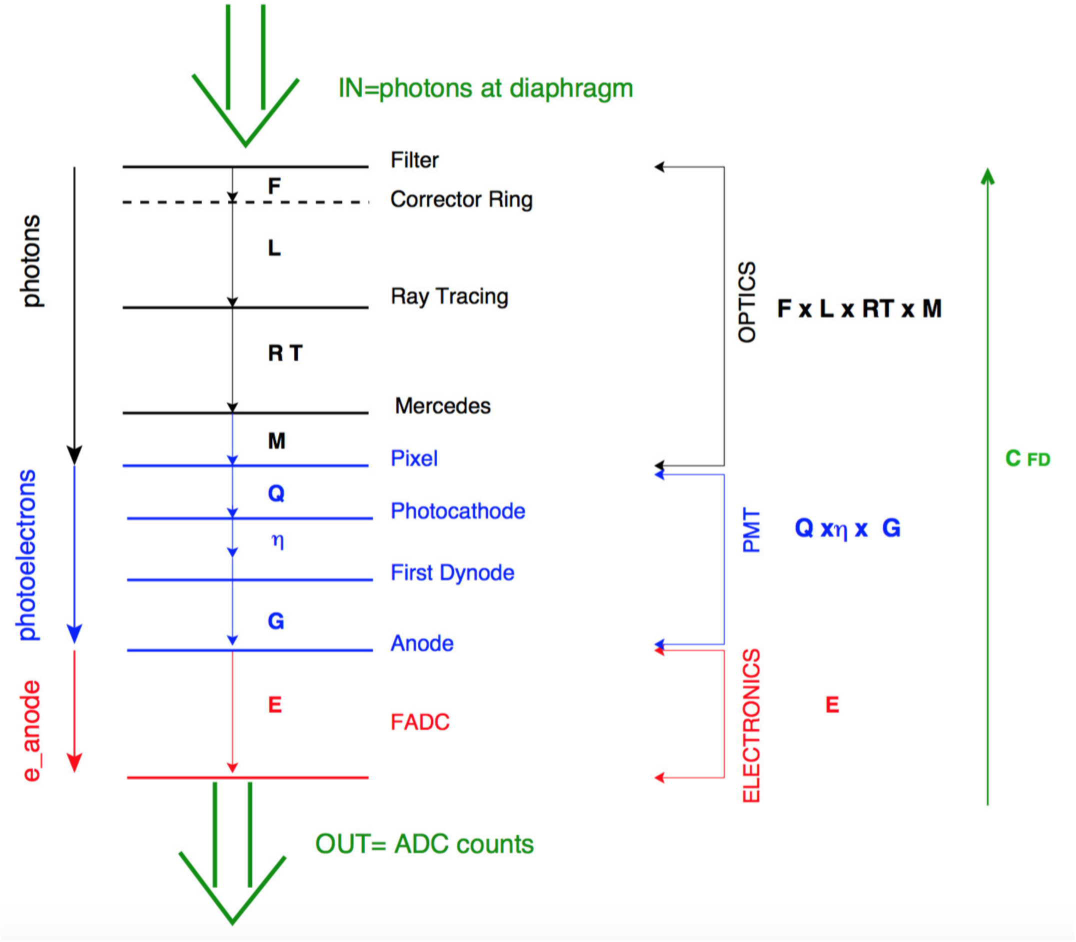

FIGURE 7.6: Scheme of the acquisition chain of the background signal, where the processes from the propagation of the NSB photons through the diaphragm of each telescope to the digitalisation in counts measured by each pixel are presented. In this scheme the empty spaces between the photomultiplier are fill by a reflective wedge device, known as Mercedes corrector that collect and redirect the light make the sky exposure more uniform in order to avoid the PMTs blind spots . The fast analog to digital converter (FADC) are devices that convert the input analogical signals entering in the detector to digital signal in a short time. Image from Caruso and Petrera (2003).

Constant	Symbol	Value	Uncertainty
Filter transmission @ 370 nm	F	0.83	0.05 (hyp.)
Corrector ring transmission @ 370 nm	L	0.9	0.05 (hyp.)
Mirror reflectivity @ 370 nm	R	0.875	0.05 (hyp.)
Camera shadow factor	T	0.79	0.05 (hyp.)
Mercedes collection efficiency @ 337 nm	M	0.93	0.05 (hyp.)
Optical factor	f	0.48 (calc.)	13.0 % (calc.)
Quantum efficiency @ 337 nm	Q	0.295	0.01 (hyp.)
Absolute calibration constant	C_{FD}	*PMT dependent*	9.9 %
Gain variance	V_G	0.41	10 %
Noise equivalent bandwidth	B	3.3	2.7 %
Pixel aperture	$\mathcal{A}_{pix}$	$2.34 \times 10^{-3}\ m^2\ sr$	/
Integration time	Δt	100 ns	/

TABLE 7.1: Table of the known or estimated conversion factors (constants in the table) of interest for the reconstruction of the night sky brightness from PMT variances. The values are taken from Caruso and Petrera (2003, 2004, 2006) while the uncertainties are hypothesized (*hyp.*), calculated (*calc.*) or can be found in the indicated references for the absolute calibration constant (Aab *et al.*, 2015), for the gain variance (Kleifges *et al.*, 2003) and for the noise equivalent bandwidth (Menshikov, Kleifges, and Gemmeke, 2003) .

- cloudy nights, that present a lower background in respect to the previous cases.

In Figure. 7.7 it is possible to appreciate the quantitative differences among data.

In order to obtain a photon flux which can be compared with the results from astronomical observatories, the following steps are accomplished Caruso and Petrera (2006); Caruso *et al.* (2005b):

1. event selection: clean and moonless nights with duration longer than 3 hours;
2. calculation of the electronic noise mean variance σ^2_{elec} and subtraction from the total variance σ^2_{ADC};
3. conversion into a NSB photon flux (eq. 7.3).

The final results can be found in Caruso *et al.* (2005a). The analysis of the diffuse night sky brightness at the Pierre Auger Observatory were not further updated after 2006, when the Fluorescence Detector was still incomplete.

7.4 Most recent results on the Night Sky Background

The variances (and other relevant information) measured from the fluorescence telescopes of the PAO are gathered in text file in ASCII format, that are identified by a string at the beginning of each file name:

- "*bg*" for the electronic noise: each night 2 files are generated for each Eye a first one containing 50 measurements before the start of usual data taking and a second one with 50 measurements at the end of the usual data taking;

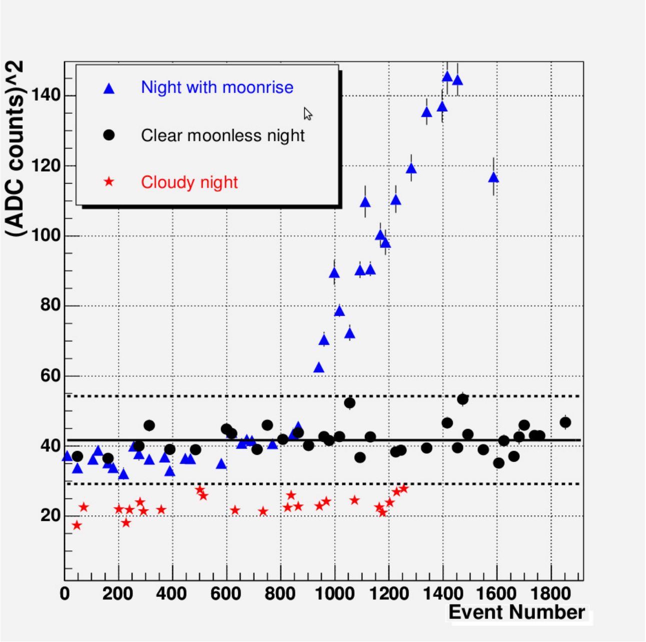

FIGURE 7.7: The variance σ^2_{ADC} of the night sky background (in $(ADC\ counts)^2$) plotted in correspondence of the event number during the night of data taking for three typical data taking nights: i) (*triangles*) night with moonrise; ii) (*circles*) clear moonless night; iii) (*stars*) cloudy night. Each point is the average value of the variance taken over all active pixels in telescope 4 at Los Leones. The continuous line is the mean value over the whole night for clear moonless conditions, the dashed lines indicate ± 1 σ. Image from Caruso *et al.* (2005a).

- *"bg_run"* for the environmental background: 1 file is created for each acquisition run for each Eye; as the data taking is often interrupted during a shift, there are as many *bg_run* files

The data are archived at the CDAS (Central Data Acquisition System) of Malargüe in a compress format (*tar.gz*) and periodically copied into other computing centres around the world.

In order to study the diffuse night sky photon flux and its temporal variability, a code was developed to accomplish a complete analysis of the electronics and environmental background variances.

The first part of the code reduces the data into a handy format (ROOT TTrees collected into TFiles).

7.4.1 Results

In this section, an overview of the most recent results is presented; in particular the plots of the different temporal behaviours are shown, allowing a complete monitoring of the background measurements performed since the beginning of the PAO until December 2015.

The first step is the study of the background variances from which the electronic noise have been already subtracted. In particular it is possible the monitoring on a short (nightly) timescale, on a longer (yearly) timescale and on the whole period of operation, different for each eye. All the three timescales are important to define the features of the NSB as observed by the PAO. The behaviour of the background luminosity during one night allows to understand the necessity of cuts and selection over the single measurements. Extending the time interval to one year, it is instead possible to observe a semi oscillation in the magnitude of the NSB. Finally, when the NSB values on the whole period considered in this analysis are plotted, one can appreciate the optimal stability of the overall measurements.

The starting point is to analyse the graphs for the nightly behaviours: the average over the 440 pixels for each recorded event (every 30 s) is plotted as a function of time for each night and each telescope. In Figure. 7.8 are shown some representative plots for the measurements of NSB variance for the same night, where 6 telescopes are drawn together.

The graphs in Figure. 7.8 have been performed from rough data, i.e. before applying the selection criteria for the exclusion of sunrise/sunset (moonrise/moonset) diffuse light. Actually the quality cuts discard the intervals with significant increasing/decreasing trends, as in the beginning and above all end parts of the shown plots.

Indeed, the nightly behaviours after the data selection allow to infer more clearly the environmental and weather conditions mainly from the presence and magnitude of fluctuations.

The starting point (Figure 7.9) is to analyse the yearly temporal behaviour of the average number of photons at diaphragm per 100 ns for the Los Leones telescopes.

In the yearly plots the different shift periods are evident as groups of points separated by intervals when the fluorescence telescopes are turned off. It can be noticed

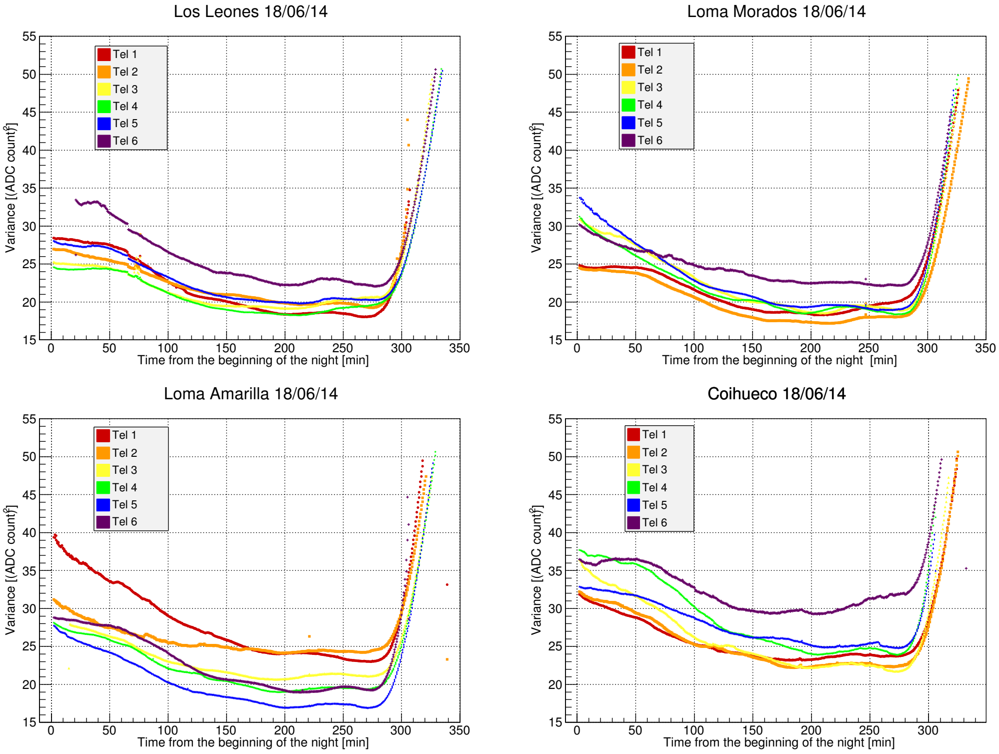

FIGURE 7.8: Temporal behaviours on the shortest timescale (single night). The night shown (July, 18 2014) was chosen because data acquisition was good and continuous for all the 24 telescopes. It can be observed: a decreasing trend at the beginning of the night, due to diffuse light after the twilight; an intermediate region of stability, where the fluctuations are effectively due to the night sky brightness or to bright stars; a final sudden increasing of the measured variances, due to the moonrise.

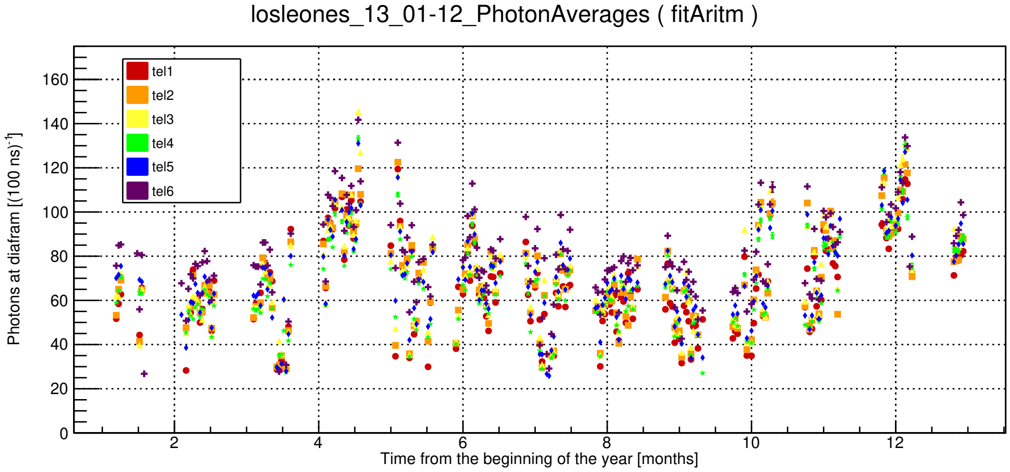

FIGURE 7.9: Temporal behaviour for 1 year (January - December 2013). Each point represents a mean number of photons at diaphragm per 100 ns, averaged over the measurements in the related night and over the pixels: in particular the values are obtained as arithmetic mean over the pixels and as time average over the whole night of data taking. The different FD shift periods are clearly distinguishable as grouping of points. Moreover one can observe a semi-annual oscillation of the values

.

that the variance values, even if averaged over the 440 pixels, can change noticeably from one night to another one also inside the same shift period: as a matter of fact the environmental condition can vary on a daily timescale, while strong fluctuations are rarer in the nightly behaviours as usually caused by sudden weather instabilities.

However the most interesting information that can be deduced is the existence of a semi-annual oscillation of the variances measured by the PAO instruments. For every year two changes of the averaged variances are observed: from a minimum in the first months (austral summer) to a maximum in the austral autumn, then from a second minimum in the winter months to a second maximum in the last months (austral spring). The temporal positions of the maxima and minima are not exactly constant, but this semi-annual oscillation of the variances is present in every year and for each Eye, even if with different magnitudes from one telescope to another one and from one period to another one. A first possible explanation concerns the seasonal changes: despite the desired isolation of the telescopes, the different temperatures and weather conditions typical of each period of the year could influence the acquisition. Anyway one can not exclude, without further analysis, that this semi-annual oscillation is generated by a true yearly variation of the night sky brightness or other phenomena.

Finally in Figure 7.10 the complete behaviour of the NSB photon flux measured by the Los Leones telescopes over the whole dataset (November 2004 - December 2015) is shown. In the corresponding plot each point represents the variance value resulting from an average over the events in the related night and over the 440 pixels, for each telescope.

The most evident characteristic of each graphs is the semi-annual oscillation, confirmed to be present since the beginning of the fluorescence data taking. The

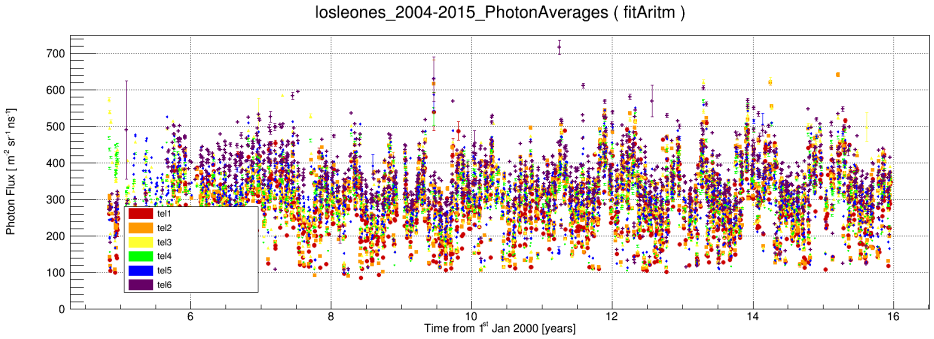

FIGURE 7.10: Temporal behaviour over the whole period analysed (November 2004 - December 2015) for the Los Leones telescopes. Each point represents a mean photon flux in $[m^{-2}sr^{-1}ns^{-1}]$, averaged over the events in the night and over all the PMT. It is observed an overall stability in data acquisition over the whole period and the presence of semi-annual oscillations.

causes of this periodical fluctuation are supposed to be intrinsic of the environmental conditions of the PAO and/or of the apparatus itself.

Further studies are required in order to go beyond the simple NSB monitoring: the semi-annual oscillations should be quantitatively interpreted to obtain a reliable result, for instance analysing the amplitudes and the related variations with time.

7.5 Correlation between CMEs and Night Sky Background

From the point of view of geophysics and atmospheric studies, the amount of data collected by the fluorescence telescopes likely contains great information about the diffuse night sky brightness, its characteristics and temporal behaviour. A specific analysis is possibly foreseen: searching for effects of highly energetic solar events on the overall night sky brightness collected by the Fluorescence Detector.

A preliminary analysis has been accomplished on possible correlation between Coronal Mass Ejection with Night Sky Background in collaboration with members of the Pierre Auger. The results of this analysis are reported in this Section.

The idea is to search for atmospheric emission timely related to strong magnetic storms associated with CMEs that can be detected by the Pierre Auger fluorescence telescopes, considering their duty cycle, bandwidth and elevation range. The reference type of event is the *aurora* (see Chapter 1), spectacular phenomenon of light and ionosphere emission due to the interaction of particles from the Sun with the Earth magnetosphere. However, the accomplished analysis is related in particular to the search for correlation between intense magnetic storms and increments of the night sky brightness photon flux.

For the correlation between CMEs and storm we used the dataset described in Chapter 6 and the list of Richardson and Cane (2010) where among other CMEs parameter, the date of storm or disturbance and the date of ICME (indicating the CME is into interplanetary medium) is reported. This list is available at the following link: www.srl.caltech.edu/ACE/ASC/DATA/level3/icmetable2.htm (Richardson and Cane, 2010). From this list we selected all events associated with CMEs in the LASCO dataset and, if possible, associated with flares, that respect the following conditions:

- arrival time of the CME between 1 and 4 days;
- $K_p > 6$
- no threshold on IMF and B_z

We created a list of selected night and then compared our information on the night about the storm with the data reported in the SolarHam archive (http://www.solarham.net/older33.htm/), where months by months the events occurring on the solar surface are reported, to the one found in the Space Weather database (https://www.spaceweatherlive.com/ and in the Space Weather Prediction Center National Oceanic and Atmospheric Administration(NOAA) (http://www.swpc.noaa.gov/, where information about geomagnetic activity are reported. A night that is not reported in our list and in all the archives mentioned above is considered without geomagnetic storms and vice versa.

The first difficulty in the search for correlation between magnetic storms and the night sky background is due to the latitude of the Pierre Auger Observatory if compared with the usual latitudes of auroras: the majority of them are observed at high latitudes, below (for the South Hemisphere) the Antarctic Polar Cicle. Another difficulty is to determine whether these atmospheric effects can be actually detected by the fluorescence telescopes from the altitudes where the auroras occur (usually in the ionosphere). The lower limit for the auroras in the atmosphere ranges from 85 – 100 km (sometimes they are observed also at 65 km in the atmosphere (Kamade and Chain, 2007)), while the upper limit is about 100 – 200 km. Lastly, an increment of the diffuse luminosity of the sky can be detected with the fluorescence telescopes only if the light emission due to the geomagnetic event is in the near ultraviolet range (while auroras produce mainly visible photons).

In spite of these problematics, the effects of intense magnetic storms have been searched in the 10 years period of data taking of the Pierre Auger Observatory between the end of 2004 and the end of 2015. In a first phase, the geomagnetic events with index $K_p > 6$ in the period 2004-2015 were gathered, keeping the temporal information about each event.

In the second phase, the geomagnetic storms were selected according to the data taking of the fluorescence telescopes in order to maintain only events happened during nights of actual measurements; moreover clean weather and low Moon percentage are required to achieve a good data quality. Only 16 events for the whole period survived these selection criteria.

In the third phase, the diffuse night sky brightness of these 16 selected nights was studied, analysing the behaviour for each one of the 24 fluorescence telescopes, with a temporal resolution of 30 seconds (the sample time of measurements). In Figure 7.11 is shown the time behaviour at different elevations (11 intervals between $0°$ and $30°$) for a given telescope. More precisely, Figure 7.11 (left) shows the night between April 22, and April 23, 2012 that was interested by an intense geomagnetic storm, started around 02:00 UTC and with a peak value of $K_p = 7$ at 03:25 UTC; as the fluorescence telescopes started taking data around 23:30 UTC, a possible effect is expected at least after 2:30 hours since the beginning of the measurements. Actually an increase of the diffuse luminosity is evident after 3-4 hours since the beginning, showing a possible correlation with the storm. In Figures 7.11 (right) is shown the night between May, 25 and May, 26 2014. However, this night presents a temporal behaviour of the night sky background quite similar to the previous one (even if only one telescope is shown, the same can be applied to the other ones) but in this case there is not correlation with magnetic events.

Finally, 3 out of 16 selected nights present a peaked increment of the photon flux in a temporal interval corresponding with the geomagnetic storm (see the green rectangles in Table 7.5); 7 nights are negative to the correlation (see the red rectangles in Table 7.5) as no appreciable fluctuations of the luminosity are observed during the related storm. The remaining 6 nights show not-negligible increments of the diffuse brightness but these variations are not temporally correlated with the magnetic storm peak or they are present only in a subset of the 24 telescopes (see the yellow rectangles in Table 7.5).

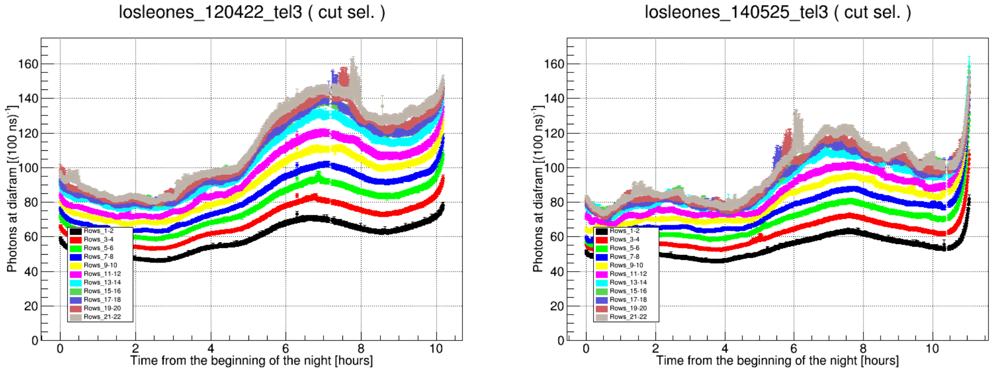

FIGURE 7.11: Temporal behaviours of the night sky background at different elevations (11 intervals between 0° and 30°) for the third telescope of the Los Leones building. Two different nights are shown, both with a temporal resolution of 30 seconds. On the left, the night between April, 22 and April, 23 2012. On the right is shown the night between May, 25 and May, 26 2014, in which it was not measured any strong geomagnetic storm.

However, this study is not sufficient to assert that phenomena related to strong geomagnetic storms induce an increment of the diffuse night sky brightness as observed by the fluorescence telescopes of the Pierre Auger Observatory. In fact the analysis accomplished until this point can be biased since the effect of a storm was searched already knowing where it should be found. This fact implies the possibility of a false positive, i.e. claiming that a storm has induced a luminous effect during a certain night when the increment was due to a different phenomenon, like a variation of the cloud coverage or not understood atmospheric effects.

In order to avoid such error, the strategy was to study the night sky brightness during nights temporally far from geomagnetic storms of high intensity ($K_p > 6$). In this manner it is possible to determine if the behaviours observed in the candidate nights can be due to different phenomena or can only be related to geomagnetic storms.

Therefore it was performed a search for nights showing a behaviour corresponding qualitatively to the luminous increase expected for a geomagnetic event in the candidate nights, but temporally far from any strong storm. This search was limited to the period from January to December 2014, in which very few strong geomagnetic storms have been measured.

For each one of the 3 candidate nights were found two other measurements which present a temporal behaviour of the night sky background quite similar to the candidate one but that can not be correlated with a magnetic storm (see Figure 7.11 on the right). Also for the 6 nights with weaker correlation was found at least another night showing the same behaviour. At this point one can suspect that the correlations found inside the selected nights are misleading, even if the accomplished analysis is not quantitative: in fact only the shape of the behaviour and not the intensity of variations was studied.

A preliminary hypothesis to explain these "spurious" luminous increases is related to the variation of the cloud coverage in the selected nights: in fact, the clouds can absorb the background photons but also, in some conditions, diffuse the light from particular sources. So in the future it would be necessary to correlate the accurate cloud monitoring performed in the PAO with the NSB measurements. Moreover, we can not exclude the incidence of other atmospheric processes or the correlation with unknown atmospheric phenomena.

In conclusion, it is not possible, at this stage, to claim the existence of a correlation between strong geomagnetic storms (induced by CMEs) and noticeable increases of the diffuse night sky background photon flux measured by the fluorescence telescopes of the Pierre Auger Observatory. However, an effect of these events on the luminous background can not be in principle excluded since the accomplished analysis is qualitative and based on a night-by-night evaluation of the fluctuations.

A possible future improvement of this study could concern the determination of a reference value for the night sky background photon flux, in order to study quantitatively the temporal variations. Moreover it would be of great interest to use maps of the cloud coverage and its temporal behaviour, when available, for the selected nights.

TABLE 7.2: Table with the main informations about the nights selected for a possible correlation between NSB behaviour and geomagnetic storms. In green, the actual candidates that present an increment of the NSB in a temporal interval corresponding with the geomagnetic storm. In yellow, nights that present NSB variations not temporally correlated with the magnetic storm peak or which are present only in a subset of the 24 telescopes. In red, nights without appreciable fluctuations of the background luminosity during the related storm.

Storm Date	Interval (UTC)	FD data Taking Interval (UTC)	Night Quality	NSB comments (UTC)
2005/05/16	03:00 05/16 06:00 05/16	23:10 05/16 09:58 05/16	foggy night with not-negligible Moon (38%) until 04:00 UTC	Peaked increment since ∼ 06:00 with maximum around ∼ 07:00, shifted of ∼ 3 hours with respect to the storm
2005/07/12	00:00 07/12 18:00 07/12 (peak 04:00)	23:30 07/11 10:15 07/12	cloudy (mainly in the last part of) (measurements with moonlight) pollution until 02:30 UTC	increment since 01:00 with maximum at ∼ 03:00 but the NSB variation is suspected to be due to cloud coverage
2010/04/12	00:00 04/12 03:00 04/12 (peak 01:42)	23:43 04/11 09:35 04/12	Clean moonless night	Peaked increment between ∼ 01:00 and ∼ 02:00
2011/02/04	03:00 02/05 06:00 02/05 (peak 02:38)	01:19 02/05 08:24 02/05	Cloudy (mainly at the beginning) But moonless night (Moon 2%)	Not evident variation of the NSB photon flux
2011/05/28	05:30 05/28 09:00 05/28	23:05 05/27 09:11 05/28	Partially cloudy Night, with moonlight pollution since ∼ 07:00 UTC	Variation due to the cloud coverage, but without peaked increments common among the telescopes
2011/09/29	00:30 09/29 06:00 09/29 (peak 03:00)	23:05 05/27 08:52 09/29	Clean moonless night after 02:00 UTC (cloudy only around) Coihueco building	Not evident variation of the NSB photon flux
2012/04/23	02:00 04/23 09:00 04/23 (peak 03:25)	23:30 04/23 09:42 04/23	Clean moonless night	Peaked increment since ∼ 02:30 with maximum around 06:00
2012/06/17	22:00 06/17 (peak 23:00)	23:02 06/17 10:13 06/16	Partially cloudy (mainly around Los Leones building) but moonless night	Increment since ∼ 03:00 with maximum around 06:30, probably due to cloud coverage as not common among the telescopes and > shifted of 3 hours with respect to the major storm
2012/07/16	03:00 07/16 18:00 07/16	23:12 07/15 10:12 07/16	Partially cloudy But moonless night	Not evident variation of the NSB photon flux
2013/06/07	03:00 06/07 06:00 06/07	23:23 06/06 10:09 06/07	Clean moonless night	Increment since ∼ 03:00 but without a proper peak (reaching stable (value around 08:30)

2013/06/29	00:00 06/29 09:00 06/29 (peak 03:00) -06:00)	23:04 06/28 04:0929 06/29	Quite clean night, but high moonlight pollution since ∼ 03:00 UTC (Moon 58%)	Peaked Increment before the storm (betwwen 00:00 and 02:00) probably related to cloud coverage
2013/10/08	21:00 10/08 (peak 02:00 10/09)	00:12 07/15 08:34 10/09	Partially cloudy night, moonless only after 02:00 UTC (Moon 14%)	Not evident variation of the NSB photon flux
2015/03/17	peak 04:35 03/17	00:19 03/17 09:11 03/17	Clean moonless night until ∼ 07:00 UTC, then moonlight pollution (Moon 21%)	Variations and peaks not common among the telescopes, probably due to cloud coverage or other phenomena
2015/05/13	03:00 05/13 09:00 05/13	23:11 05/12 09:55 05/13	Clean moonless night until ∼ 06:00 UTC, then moonlight pollution (Moon 38%)	Slow increment since ∼ 02:30 but not common among the telescopes
2015/06/22	23:00 06/22 09:00 06/23 (peak 04:30)	00:45 06/23 10:14 06/23	Clean moonless night since 03:00 UTC, before moonlight pollution (Moon 32%)	Small peaked increment between 06:00-09:00, shifted of > 2 hours with respect to the storm (probably due to cloud in combination with Moon)
2015/06/25	06:25-08:30	04:30 06/25 10:14 06/25	Quite clean and moonless night since 05:30 UTC, before moonlight pollution (Moon 50%)	After moon-set the photon flux stabilize until ∼ 08:30 when it decrease to a lower value

Chapter 8

Discussion and Conclusions

The study carried out in this Thesis on solar phenomena and their effects on the Earth provides some interesting results on aspects of the magnetic activity during different phases of the solar cycle.

The first analysis carried out in the Thesis concerns the location of the C-, M- and X-class flares registered by GOES during the Solar Cycles 23 and 24. The occurrence of events of each class seems to reproduce very well the different phases of the two cycles. The spatio-temporal distribution of the flares also shows several persistent domains of activity, similar to the distribution of the ALs. The events of X-class, whose impacts on Earth environment can be significant, seem to occur at the peak of the energy released in ALs of 10 degrees of latitude and among a time interval of 9 Carrington rotations. A phase of about 4 Carrington rotations where the ALs seem to increase their budget of released energy has been singled out. We argue that this behaviour may be ascribed to a corresponding trend of the emergence of magnetic flux in ALs.

The part of the Thesis dedicated to the statistical study of the CME occurrence during the Solar Cycles 23 and 24 by means of the LASCO/SOHO mission data provides a further contribution to the comprehension of the trend of these phenomena in the solar atmosphere. The results indicate that the number of events registered during the peak of activity of the solar cycle 24 was higher than the number of events occurred during the previous cycle, although the solar cycle 24 was weaker in terms of the Wolf number. Some interesting behaviours of the CME physical properties like velocity, acceleration and angular width were highlighted. In particular, it has been found that the higher is the energy involved in the flares (based on C, M, X, classes), the higher the CMEs velocity is. The occurrence of slower CMEs during minima of the solar cycle is correlated with a higher positive acceleration of the plasma. Moreover, it seems that the slowest CMEs are the narrowest ones.

Looking at the correlation between flares and CMEs it has been found that the highest number of CMEs and flares detected in the CDAW dataset (59.57 %) is characterized by a difference in time between 10 and 80 minutes. A wider temporal window has been found using the CACTus dataset due to the different criteria adopted to define a CME by the two catalogues. In any case, for both data-sets, most of the CMEs that are characterized by higher linear velocities are associated with flares. However, the main result of this study is the log-log relationship between the flare flux and the CME mass:

$$Log(m_{CME}) \propto 0.23 Log(\Phi_f). \tag{8.1}$$

This relationship is slightly different from a previous analysis performed by Aarnio *et al.* (2011), because of a refinement of the statistics performed using a wider data-set and a more precise estimation of the flux delivered by the flares.

It is also remarkable that this relationship is no longer valid when we limit the sample of flare/CME pairs to the different phases of the solar cycle. This means that the log-log relationship is only valid from a statistical point of view, i.e. when we consider a sample of events large enough.

We believe that the result obtained as far as the log-log relationship between the flare flux and the CME mass can provide useful indications on the mechanisms at the base of the flare - CME connection, and in particular on the models that can better explain these phenomena. Based on our results in fact the most promising models are those based on mass loading, tether release and tether cutting, breaking and flux rope.

Further study and analysis must be carried out in order to disentangle from this list the most realistic model.

The last part of the Thesis was devoted to an investigation of possible effects of CMEs associated to the most energetic flares on the night sky brightness determined using the data collected by the Fluorescence Detectors of the Pierre Auger Observatory. The preliminary analysis carried out on a period of 10 years (2004 - 2015), on a sample of CMEs causing geomagnetic storms with a K_p index greater than 6, does not allow us to claim the existence of a clear correlation between geomagnetic storms and variations in the night sky background.

It is however worthwhile to stress that this result might be affected by the method used in this analysis, which at this stage was based on a night-by-night evaluation of the fluctuations. Therefore an improvement in this investigation might be obtained by determining a reference value for the night sky background photon flux.

Finally, we would like to highlight the importance of our results in the framework of Space Weather. This Thesis may in fact provide an improvement of our understanding of the relationship between flares, CMEs, geomagnetic storms and effects that they can produce on the Earth's environment. A full comprehension and eventually forecasting of the occurrence of flares and CMEs is necessary in order to avoid or mitigate effects related to the propagation of these events into the interplanetary space.

Taking into account the result concerning the presence of preferential domains for flare occurrence, we believe that our results can provide a useful contribution to the forecast of X-class flares, which are usually associated with the most massive CMEs (Compagnino *et al.*, 2017) and to the strongest geomagnetic storms. Therefore a patrol of the ALs and a continuous monitoring of the energy released by flares could provide a good tool for solar eruptions forecasting.

The correlation found between CMEs mass and flare energy flux is a first step to shed light on some open questions related to these phenomena, like for instance how is the energy stored and what fraction of energy is released during the eruption, what is the source of the CME mass and how they are accelerated.

The research carried out using the Pierre Auger fluorescence telescopes on possible night-sky brightness variation related to strong magnetic storms associated with CMEs and flares, even if at this stage has not provided a clear correlation between these events, is a first step in a direction that has never been investigated until now and it surely deserves further investigation.

List of Figures

1.1 Atmosphere 2
1.2 Filament structure 3
1.3 TRACE flare 4
1.4 Ribbon flare 4
1.5 CME observed by LASCO 5
1.6 Interplanetary Magnetic Field (IMF) 7
1.7 CIR formation 8
1.8 Map of k_p index 8
1.9 Map of DST index 9
1.10 Effect of a geomagnetic storm 10
1.11 Aurora polar cup 11
1.12 Aurora 12

2.1 Profile of solar flare 14
2.2 Different phases of the flares 15
2.3 Flare evolution 17
2.4 Standard flare model 18
2.5 Chromospheric evaporation 19

3.1 Total flares distributions compared with Wolf Number 22
3.2 Different class flares distribution 23
3.3 Flare longitude in the Southern hemisphere 24
3.4 Flare longitude in the Northern hemisphere 25
3.5 Mean energy flares Flux without latitude condition 26
3.6 Mean energy flares flux with latitude condition 27
3.7 Mean energy integrated flares flux with latitude condition 28
3.8 Zoom of the flux of the flares about 30 days before and after the X flares start 29

4.1 CMEs Structures . . . 31
4.2 Gradual and impulsive CMEs . . . 32
4.3 Partial halo CME evolution . . . 33
4.4 Backside and Frontside CMEs . . . 34
4.5 Thermal blast model . . . 34
4.6 Mass loading model . . . 34
4.7 Tether release and tether cutting model . . . 35
4.8 Breakout model . . . 35

5.1 Solar cycle 23 and 24 . . . 38
5.2 Total mean velocity, acceleration, and width of the CMEs . . . 39
5.3 Annual CMEs velocity . . . 41
5.4 Annual CMEs acceleration . . . 41
5.5 Annual CMEs width . . . 42
5.6 Annual CMEs mean polar angle . . . 43

6.1 CMEs-flares time correlations . . . 48
6.2 C, M, and X class flares for the CDAW dataset . . . 51
6.3 C, M, and X class flares for the CACTus dataset . . . 52
6.4 Velocity of the CMEs associated with flares . . . 53
6.5 Acceleration of the CMEs associated with flares . . . 53
6.6 Velocity of the CMEs associated with flares for different class . . . 55
6.7 Scatter plot of CMEs associated with flares . . . 56
6.8 CMEs-mass-flux relationship . . . 56

7.1 External Auger . . . 58
7.2 Internal Auger . . . 59
7.3 Quantum Efficiency . . . 59
7.4 Light FD track . . . 60
7.5 Season variation of NSB and solar flux . . . 62
7.6 Acquisition chain . . . 65
7.7 Previous result of the NSB variance . . . 67
7.8 Nightly Behaviour of NSB . . . 69
7.9 Yearly photon flux . . . 70
7.10 Total photon flux . . . 71

7.11 Candidate Event 73

List of Tables

1.1 Geomagnetic storm classification 9

2.1 Hα Flare classification. 15
2.2 GOES Flare classification 15

6.1 Previous results on the correlation between CMEs, flares and eruptive prominences. 46
6.2 Correlation between CMEs and flares for CDAW and CACTus datasets in the ± two hours time interval. 49
6.3 Correlation between CMEs and flares for CDAW and CACTus datasets in the ± one-hour time interval. 49
6.4 Correlation between CMEs and flares for CDAW and CACTus datasets in the ± 30 min. time interval. 49

7.1 NSB constants 66
7.2 Storm Selected Night 75

Acknowledgements

In questa sezione ho il piacere di ringraziare tutti quelli che mi hanno supportato è *sopportato* in questo percorso di Dottorato e nella stesura del lavoro tesi.
In paricolare ringrazio la mia Supervisor **Prof.ssa Francesca Zuccarello**, che si è mostrata sempre molto gentile e disponible nei miei confronti e con la sua chiarezza e professionalità mi ha aiutato e chiarito i dubbi nel mio percorso formativo, arrichendomi culturalmente, ed al contempo stesso con la sua autorevolezza (quando necessaria) mi ha fatto capire i miei errori, ed in collaborazione con il mio tutor il **Dr Paolo Romano**, *che ha impostato la mia voce come souneria del cellulare* mi hanno aiutato a crescere professionalmente, anche cambiando il mio modo di pensare.
Ringrazio anche i membri della collaborazione Pierre Auger, in Particolare la **Prof.ssa Caruso** ed il dottorando **Gioacchino Alex Anastasi** che hanno collaborato attivamente alla stesura di una parte della tesi di dottorato e sono stati sempre disponibili. Ringrazio anche i referee esterni **Dott.ssa Rita Ventura & Dott. Alessandro Bemporad** che hanno valutato e corretto la mia tesi, dandomi suggerimenti utili e preziosi per renderla ancora migliore. Ringrazio inoltre **L'INAF** dell' **Osservatorio Astrofisico di Catania** ed in particolare i miei colleghi di lavoro del **Gruppo Di Ricerca di Fisica Solare** che sono stati sempre pronti a darmi qualsiasi suggerimento. Un ringraziamento particolare va infine alla **mia famiglia** che mi ha sempre sostenuto e mi sosterrà sempre (spero!) nella mie scelte, ed a mio **padre** che mi ha sempre aiutato, accompagnato, e sostenuto durante le mie lunghe giornate nel mio percorso di studi. **Spero di non aver dimenticato nessuno e ringrazio comunque tutti.**

Bibliography

Aab,A.Abreu, P., Aglietta,M. *et al.*2015, The Pierre Auger Cosmic Ray Observatory Nuclear Instruments and Methods in Physics Research A, **798**,172 The Pierre Auger Collaboration

Aarnio, A.N., Stassun, K.G., Hughes, W.J., McGregor, S.L.: 2011, *Solar Phys.* **268**, 195.

Abu-Zayyad, et al., Nucl. Instr. and Meth. A 450 (2000) 253.

Abraham J., Abreu P. , Aglietta M. *et al.*2010, The fluorescence detector of the Pierre Auger Observatory Nuclear Instruments and Methods in Physics Research A 620, 227

Acuña, M. H., Ogilvie, K. W., Baker, D. N., et al. 1995, *Space Sci. Rev.*, 71, 5

Allekotte I. , et al.Pierre Auger Collaboration, Nucl. Instr. and Meth. A 586 (2008) 409.

Antiochos, S. K., DeVore, C. R., & Klimchuk, J. A. 1999, ApJ, 510, 485

Aschwanden, M.J. (2005). Physics of the Solar Corona. An Introduction., Pour la science Praxis Publishing Ltd.

Baltrusaitus,R.M. et al., Nucl. Instr. and Meth. A 240 (1985) 410.

Balthasar, H. 2007, *Astron. Astrophys.*, 471, 281

Bellido J.A.,etal.,Pierre Auger Collaboration,in:Proceedings of the 29th ICRC, arXiv:astro-ph/0507103, 2005.

Bemporad, A., Zuccarello, F. P., Jacobs, C., Mierla, M., & Poedts, S. 2012, *Solar Phys.*, 281, 223

Berdyugina, S.V., Moss, D., Sokoloff, D. and Usoskin, I.G.: 2006, Astron. Astrophys. 445, 703.

Brandenburg, A., and Subramanian, K. 2005, Physics Reports, 417, 1

Bothmer, V., & Schwenn, R. 1996, Advances in Space Research, 17

Brueckner, G.E., Howard, R.A., Koomen, M.J., Korendyke, C.M., Michels, D.J., Moses, J.D., Socker, D.G., Dere, K.P., Lamy, P.L., Llebaria, A., Bout, M.V., Schwenn, R., Simnett, G.M., Bedford, D.K., Eyles, C.J.: 1995, *Solar Phys.* **162**, 357. ADS, DOI.

Cane, H.V.: 2000, *Space Sci. Rev.* **93**, 55. ADS, DOI.

Carmichael, H. (1964). A Process for Flares. NASA Special Publication, 50, 451

Carrington, R. C. 1863, in Observations of the Spots on the Sun (London: Redhill, Williams and Norgate), 246

Carrington, R. C. 1859, MNRAS, 20, 13.

Caruso R., and Petrera S., A photon background model for the FD trigger simulation. GAP-2003-083. Nov. 2003.

R. Caruso and Petrera, S. Measurement of the sky photon background flux at Los Leones. GAP-2004-072. Dec. 2004.

Caruso R. and Petrera S., Status of the sky photon background flux measurement. GAP-2006-014. Feb. 2006.

Caruso R. et al. "Measurement of the Sky Photon Background Flux at the Auger Observatory". In: ICRC-2005. 29th International Cosmic Ray Conference Pune. 2005.

Caruso R. et al. "Quality studies of the data taking conditions for the Auger Fluorescence Detector". In: ICRC-2005. 29th International Cosmic Ray Conference Pune. 2005.

Chen, A.Q., Chen, P.F., Fang, C.: 2006, *Astron. Astrophys.* **456**, 1153. ADS, DOI.

Chen, P.F.: 2011, Coronal Mass Ejections: Models and Their Observational Basis. Living Rev. Solar Phys. 8, 1

Cliver, E. W., and A. G. Ling (2009), Low-frequency type III bursts and solar energetic particle events, Astrophys. J., **690**, 598.

Compagnino, A., Romano, P., & Zuccarello, F. 2017, SoPh, 292, 5

Covington, A. E. 1969, JRASC, 63, 125

Cremades, M. H. Three-dimensional configuration and evolution of coronal mass ejections.Ph.D. Dissertation. Fakultät für Physik und Geowissenschaften der Technischen Universität Carolo-Wilhelmina, Braunschweig, Germany, 2005.

Cremades, H., St. Cyr, O.C.: 2007, *Adv. Space Res.* **40**, 1042. ADS, DOI.

de Toma, G., White, O.R., & Harvey, K.L., 2000, *Astrophys. J.*, 529, 1101

Delaboudinière, J.-P., Artzner, G.E., Brunaud, J., Gabriel, A.H., Hochedez, J.F., Millier, F., Song, X.Y., Au, B., Dere, K.P., Howard, R.A., Kreplin, R., Michels, D.J., Moses, J.D., Defise, J.M., Jamar, C., Rochus, P., Chauvineau, J.P., Marioge, J.P., Catura, R.C., Lemen, J.R., Shing, L., Stern, R.A., Gurman, J.B., Neupert, W.M., Maucherat, A., Clette, F., Cugnon, P., van Dessel, E.L.: 1995, *Solar Phys.***162**, 291. ADS, DOI.

Dolei, S., Romano, P., Spadaro, D., & Ventura, R. 2014, *Astron. Astrophys.*, 567, A9

Dryer, M., Space Sci. Rev., 33, 233, 1982.

Dryer, M., Detman, T., Watari, Shinichi, Smith, Z., Garcia, H.A., 1996. Coronal change at the South-West limb observed by YOHKOH on 9 November 1991, and the subsequent interplanetary shock at Pioneer Venus Orbiter,. Solar Physics 167 (1–2), 357 369

Eastwood, J.P., Hietala, H., Toth, G. et al. Space Sci Rev (2015) 188: 251.

Emslie, A.G., Dennis, B.R., Shih, A.Y., Chamberlin, P.C., Mewaldt, R.A., Moore, C.S., Share, G.H., Vourlidas, A. & Welsch, B.T. (2012). Global Energetics of Thirtyeight Large Solar Eruptive Events. Astrophysical Journal, 759, 71.

Forbes, T. G. & Acton, L. W. 1996, ApJ, 459, 330

Forbes, T. G. and Isenberg P. A., 1991. ApJ, 373, 294.

Forbes, T.G., 2000, Geophys. J., Res. 105, 23153.

Gilbert, H.R., Holzer, T.E., Burkepile, J.T., Hundhausen, A.J.: 2000, *Astrophys. J.* **537**, 503. ADS, DOI.

Golub, L., & Pasachoff, J. M. 2009, The Solar Corona by Leon Golub, Jay M. Pasachoff. Cambridge University Press, 2009. ISBN: 9780521882019,

Gopalswamy, N., Makela, P., Akiyama, S., Yashiro, S., Thakur, N.: 2015a, *Sun Geosphere* **10**, 111. ADS, arXiv.

Gopalswamy, N., Xie, H., Akiyama, S., Mäkelä, P., Yashiro, S., Michalek, G.: 2015b, *Astrophys. J. Lett.***804**, L23. ADS, DOI.

Gopalswamy, N., Yashiro, S., Michalek, G., et al. 2010, Sun and Geosphere, 5, 7

Gopaswamy, N., Solar connections of geoeffective magnetic structures, J. of Atmospheric and Solar-Terrestrial Physics, **70** (17), 2078, (2008)

Gopalswamy, N., Yashiro, S., Akiyama, S.: 2007, Geoeffectiveness of halo coronal mass ejections. J. Geophys. Res. **112**, 6112.

Gopalswamy, N., Shimojo, M., Lu, W., et al. 2004, Advances in Space Research, 33, 676

Gopalswamy, N., S. Yashiro, A. Lara, M. L. Kaiser, B. J. Thompson, P. T. Gallagher, and R. A. Howard (2003), Large solar energetic particle events of cycle 23: A global view, Geophys. Res. Lett., **30** (12), 8015, doi:10.1029/2002GL016435

Gosling, J.T., Hildner, E., MacQueen, R.M., Munro, R.H., Poland, A.I., Ross, C.L.: 1976, *Solar Phys.* **48**, 389. ADS, DOI.

Gosling, J. T., J. Geophys. Res., 98, 18, 937, 1993

Gyenge, N., Baranyi, T., & Ludmány, A. 2014, *Solar Phys.*, 289, 579

Gyenge, N., Ludmány, A., & Baranyi, T. 2016, *Astrophys. J.*, 818, 127

Gyenge, N., Singh, T., Kiss, T. S., Srivastava, A. K., & Erdélyi, R. 2017, *Astrophys. J.*, 838, 18

Gulyaev, R. A., & Gulyaeva, T. L. 1995, Advances in Space Research, 16

Gulyaev, R. A. 1996, Advances in Space Research, 17,

Harrison, R. A. 1986, Astron. Astrophys., 162, 283

Hirayama, T. (1974). Theoretical Model of Flares and Prominences. I: Evaporating Flare Model. Solar Physics, 34, 323

Howard, R. A. et al. Coronal mass ejections 1979-1981. Journal of Geophysical Research, v. 90, p. 8173, 1985.

Howard, R.A., Michels, D.J., Sheeley, N.R., Jr. and Koomen, M.J., The observation of a coronal transient directed at earth, ApJ, **263**, L101, (1982)

Howard, M.: 1974, *Spaceflight* **16**, 383. ADS.

Huang, X., Zhang, L., Wang, H., & Li, L. 2013, *Astron. Astrophys.*, 549, 6

Hundhausen, A., 1999. Coronal mass ejections. In: Strong, Keith T., Saba, Julia L.R., Haisch, Bernhard M., Schmelz, Joan T. (Eds.), The Many Faces of the Sun: A Summary of the Results from NASA's Solar Maximum Mission. Springer, New York, p. p. 143.

Hundhausen, A.J., Coronal Expansion and Solar Wind, In: Coronal Expansion and Solar Wind, XII, **238** Springer-Verlag, New York, p. 101, (1972).

Hundhausen, A.J., Sawyer, C.B., House, L., Illing, R.M.E. and Wagner, W.J., 1984, Geophys. J. Res. 89, 2639

Hundhausen, A.J.: 1993, *J. Geophys. Res.* **98**, 13177 ADS, DOI.

Ivanov, E.V, Obridko, V.N.: 2001, *Solar Phys.* **198**, 179. ADS, DOI.

Ivanov, E. V. 2003, in A.Wilson (ed),ISCS Symposium,ESASP 535, 105

Ivanov, E. V. 2007, Advances in Space Research, 40, 959

Janvier, M., Aulanier, G., & Démoulin, P. 2015, *Solar Phys.*, 290, 3425

Jenkins J.L. (2009) Observing the White Light Sun. In: The Sun and How to Observe It. Astronomers' Observing Guides. Springer, New York, NY

Juckett, D. A., 2006, Solar Phys., 245, 37

Juckett, D. A., 2007, Solar Phys., 245, 37

Kahler, S. W., et al. 1989, Astrophys. J., 344, 1026

Kamide, Y., Chian, A. (Eds.) 2007, Springer Berlin Heidelberg New York : ISBN: 978-3-540-46514-6 Handbook of the Solar-Terrestrial Environment

Kitchatinov, L. L., & Olemskoi, S. V. 2005, Astronomy Letters, 31, 280

Kleifges, M. , et al., IEEE Trans. Nucl. Sci. NS-50 (4) (2003) 1204.

Kleifges, M., et al. "Statistical current monitor for the cosmic ray experiment Pierre Auger". In: IEEE Transactions on Nuclear Science 50.4 (2003), 1204

Kopp, R.A. & Pneuman, G.W. (1976). Magnetic reconnection in the corona and the loop prominence phenomenon. Solar Physics, 50

Kostuchenko, I.G. & Benevolenskaya, E.E. Geomagn. Aeron. (2014) 54: 1019.

Krall, J., Chen, J., Santoro, R.: 2000, "Drive Mechanisms of Erupting Solar Magnetic Flux Ropes", Astrophys. J., 539, 964

Labrosse, N., Heinzel, P., Vial, J. C., Kucera, T., Parenti, S., Gunàr, S., Schmieder, B. and Kilper, G. (2010), Physics of Solar Prominences: I–Spectral Diagnostics and Non-LTE Modelling, βr 151, 243332.

Lakhina, G.S.; Alex, S.; Tsurutani, B.T.; Gonzalez, W. D., Research on Historical Records of Geomagnetic Storms, In Coronal and Stellar Mass Ejections, Eds. Dere, K.P., Wang, J. and Yan, Y., Proce. IAU Symposium No. **226**, Cambridge: Cambridge University Press, p. 3, (2005)

Leinert, C., Bowyer, S., Haikala, L. K., et al. 1998, *Astron. Astrophys. Suppl.*, 127, 1

Li, J. 2011, ApJ, 735, 130

Lin, J., Forbes, T.G.: 2000, *J. Geophys. Res.* **105**, 2375. ADS, DOI.

Loewe, C.A., Prölss, G.W.: 1997, Classification and mean behavior of magnetic storms. J. Geophys. Res. **102**, 14209.

Low, B.C., 1984, Ap J., 281, 392

Low, B.C., 1990, Annual. Review. A & A, 28, 491

Low, B. C. 2001, *J. Geophys. Res.*, 106, 25141

Ludwig, G., Johnson, D.: 1981, *Adv. Space Res.* **1**, 23. ADS, DOI.

Mackay, D. H., Karpen, J. T., Ballester, J. L., Schmieder, B. and Aulanier, G. (2010), Physics of Solar Prominences: II– Magnetic Structure and Dynamics, Space Science Reviews 151, 333399

MacQueen, R.M., Fisher, R.R.: 1983, *Solar Phys.* **89**, 89. ADS, DOI.

S. F. Martin. Conditions for the formation and maintenance of filaments. Solar Phys., 182:107, 1998.

Menshikov, A. ,Kleifges M., and Gemmeke, H. "Fast gain calibration of photomultiplier and electronics". In: IEEE Transactions on Nuclear Science 50.4 (2003), pp. 1208

Michalek, G., Gopalswamy, N., Lara, A., Yashiro, S.: 2006, Properties and geoeffectiveness of halo coronal mass ejections. Space Weather **4**, 10003.

Mittal, N., Narain, U.: 2009, *New Astron.* **14**, 341. ADS, DOI.

Mittal, N., Sharma, J., Tomar, V., Narain, U.: 2009, *Planet. Space Sci.* **57**, 53. ADS, DOI.

Moon, Y.J., Choe, G.S.,Wang, H., Park, Y.D., Cheng, C.Z.: 2003, *J. Korean Astron. Soc.* **36**, 61. ADS, DOI.

Naitamor, S., Coronal Mass Ejection: their sources and geomagnetic disturbances, Mem. S.A.It., 76, 1011, (2005)

Padmanabhan, J., Bisoi, S.K., Ananthakrishnan, S., Tokumaru, M., Fujiki, K., Jose, L., Sridharan, R.: 2015, *J. Geophys. Res.* **120**, 5306. ADS, DOI.

Parenti, S. (2014), Solar Prominences: Observations, Living Reviews in Solar Physics 11.

Patat F., "The dancing sky: 6 years of night-sky observations at Cerro Paranal". In: Astronomy & Astrophysics 481.2 (2008), pp. 575–591.

Patat F. "UBVRI night sky brightness during sunspot maximum at ESO-Paranal". In: Astronomy & Astrophysics 400.3 (2003), pp. 1183.

Phillips, K.: 1990, *Astronomy Now* **4**, 28. ADS. DOI.

Pick, M., Forbes, T. G., Mann, G., Cane, H. V., Chen, J., Ciaravella, A., Cremades, H., Howard, R. A., Hudson, H. S., Klassen, A., Klein, K. L., Lee, M. A., Linker, J. A., Maia, D., Mikic, Z., Raymond, J. C., Reiner, M. J., Simnett, G. M., Srivastava, N., Tripathi, D., Vainio, R., Vourlidas, A., Zhang, J., Zurbuchen, T. H., Sheeley, N. R., MarquÃľ, C.: 2006, "Multi- Wavelength Observations of CMEs and Associated Phenomena. Report of Working Group F", Space Sci Rev, 123, 341

Priest, E. R. Solar flare magnetohydrodynamics (Gordon and Breach science publisher, 1981)

Qiu, J., Yurchyshyn, V.B.: 2005, *Astrophys. J.* **634**, L121. ADS, DOI.

Raftery, C.L., Gallagher, P.T., Milligan, R.O., Klimchuk, J.A.: 2009, Multi-wavelength ob- servations and modelling of a canonical solar flare. Astron. Astrophys. 494, 1127.

Richardson, I. G., & Cane, H. V. 2010, *Solar Phys.*, 264, 189

Riley, P., Lionello, R., MikiÄĞ, Z., Linker, J.: 2008, "Using Global Simulations to Relate the Three Part Structure of Coronal Mass Ejections to In Situ Signatures", Astrophys. J., 672, 1221

Robbrecht, E., Berghmans, D., Van der Linden, R.A.M.: 2009, *Astrophys. J.***691**, 1222. ADS, DOI.

Sánchez S. F., et al. "The night sky at the Calar Alto observatory". In: Publications of the Astronomical Society of the Pacific 119.860 (2007), 1186.

Segarra, A. & Curto, J. (2015). Recovering of local magnetic K-indices from global magnetic Kp-indices using neural networks: An application to Antarctica. Annals of Geophysics. 58 ,4

Sheeley Jr, N.R., Walters, J.H., Wang, Y.-M. & Howard, R.A.: 1999, "Con- tinuous tracking of coronal outflows: Two kinds of coronal mass ejections", J. Geophys. Res., 104, 24739

Smith, S. M., Mendillo, M., Wilson, J. K., & Baumgardner, J. 2001, Advances in Space Research, 27, 1181

Srivastava, N. and Venkatkrishnan, P., Solar and interplanetary sources of major geomagnetic storms during 1996-2002, J. Geophys. Res., **109**, A10103, (2004)

St. Cyr, O.C., Webb, D.F.: 1991, *Solar Phys.* **136**, 379. ADS, DOI.

St. Cyr, O.C., Burkepile, J.T., Hundhausen, A.J., Lecinski, A.R.: 1999, *J. Geophys. Res.* **104**, 12493. ADS, DOI.

Sturrock, P.A. (1966). Model of the High-Energy Phase of Solar Flares. Nature, 211, 695 697.

Subramanian, P., Dere, K.P.: 2001, *Astrophys. J.* **561**, 372. ADS, DOI.

Sun, X., Hoeksema, J.T., Liu, Y., Aulanier, G., Su, Y., Hannah, I.G., Hock, R.A.: 2013, Hot Spine Loops and the Nature of a Late-phase Solar Flare. Astrophys. J. 778, 139.

Tandberg-Hanssen, Einar; Emslie, A. Gordon (1988). Cambridge University Press, ed. "The physics of solar flares".

Tripathy,S.C., Jain, K., Hill, F.: 2015, *Astrophys. J.* **812**, 20. ADS, DOI.

Usoskin, I. G., Berdyugina, S. V., & Poutanen, J. 2005, *Astron. Astrophys.*, 441, 347

Usoskin, I. G., Berdyugina, S. V., Poutanen, J., 2005. A&A, 441, 347

van Ballegooijen, A.A., Martens, P.C.H.: 1989, Formation and eruption of solar prominences. Astrophys. J. 343, 971.

Vršnak, B., Sudar, D., Ruždjak, D., & Žic, T. 2007, *Astron. Astrophys.*, 469, 339.

Vourlidas, A., Howard, R. A., Esfandiari, E., et al. 2010, *Astrophys. J.*, 722, 1522-1538

Vourlidas, A., Lynch, B. J., Howard, R. A., Li, Y.: 2013, "How Many CMEs Have Flux Ropes? Deciphering the Signatures of Shocks, Flux Ropes, and Prominences in Coronagraph Observations of CMEs", Solar Phys., 284, 179

Vršnak, B., Sudar, D., & Ruždjak, D. 2005, *Astron. Astrophys.*, 435, 1149

Wang, Y. M.; Ye, P. Z.; Wang, S.; A statistical study on the geoeffectiveness of Earth-directed coronal mass ejections from March 1997 to December 2000. J. Geophys. Res. 107, 1340 (2002)

Watari, S., Smith, Z., Garcia, H. A., Detman, T., & Dryer, M. 1996, *Solar Phys.*, 167, 357

Webb, D.F.: 2002, CMEs and the solar cycle variation in their geoeffectiveness. In: Wilson, A. (ed.) From Solar Min to Max: Half a Solar Cycle with SOHO, ESA SP 508, 409.

Webb, D.F., Howard, T.A: 2012, *Liv. Rev. Solar Phys.* **9**, 3,

Weber, M. A., Fan, Y., & Miesch, M. S. 2013, *Astrophys. J.*, 770, 149

Wu, S. T., Space Sci. Rev., 32, 115. 1982.

Yang, S. H., Zhang, J., Jin, C. L., Li, L. P., & Duan, H. Y. 2009, *Astron. Astrophys.*, 501, 745

Yashiro, S., Gopalswamy, N., Michalek, G., St. Cyr, O. C., Plunkett, S. P., Rich, N. B., Howard, R. A.: 2004, "A catalog of white light coronal mass ejections observed by the SOHO spacecraft", J. Geophys. Res.A, 109, 7105

Yashiro, S., Michalek, G., Gopalswamy, N.: 2008, Annales Geophysicae **26**, 3103. ADS, DOI.

Yashiro, S., Michalek, G., Akiyama, S., Gopalswamy, N., & Howard, R. A. 2008, *Astrophys. J.*, 673, 1174-1180

Yashiro, S., & Gopalswamy, N. 2009, Universal Heliophysical Processes, 257, 233

Youssef, M.: 2012, *NRIAG J. Astron. Geophys.* **1**, 172. ADS, DOI.

Zhang, L. 2012, Ph.D. Thesis, 78,

Zhang, J., Dere, K.P., Howard, R.A., Kundu, M.R., White, S.M.: 2001a, *Astrophys. J.* **559**, 452. ADS, DOI.

Zhang, J ., Richardson, I.G., Webb, D.F., Gopalswamy, N., Huttunen, E., Kasper, J ., Nitta, N.V., PoomVises, W., Thompson, B.J., Wu, C.-C., Yashiro, S. and Zhukov, A.N., Solar and interplanetary sources of major geomagnetic storms (Dst $\leq$ -100 nT) during 1996-2005, J. Geophys. Res., **112(A12)**, A12103, (2007).

Zhang, L. Y., Wang, H. N., & Du, Z. L. 2008, *Astron. Astrophys.*, 484, 523

Zhang, L., Mursula, K., Usoskin, I., & Wang, H. 2011, *Astron. Astrophys.*, 529, 23

Zhao, X., and M. Dryer (2014), Current status of CME/shock arrival time prediction, Space Weather, **12**, 448.

Zhou, G., Wang,J., Cao, Z.: 2003, *Astron. Astrophys.* **397**, 1057. ADS, DOI.

Zhukov, A.N., Solar Sources of Geoeffective CMEs: a SOHO/EIT View, In: coronal and stellar mass ejections, Eds. Dere, K.P., Wang, J. and Yan, Y., Proce. IAU Symposium No. **226**, (Cambridge: Cambridge University Press), p. 437, (2005).

Zirin, H. 1988, Astrophysics of the Sun, Cambridge University Press, 1988, 440

Zolotova, N.V., Ponyavin, D.I.: 2014, *J. Geophys. Res.* **119**, 3281. ADS, DOI.